MASS MEASUREMENT OF ^{27}P TO IMPROVE TYPE-I X-RAY BURST MODELS AND IMPLEMENTATION OF PHASE IMAGING ION CYCLOTRON RESONANCE MASS MEASUREMENT TECHNIQUE

By

Isaac T. Yandow

A DISSERTATION

Submitted to
Michigan State University
in partial fulfillment of the requirements
for the degree of

Physics — Doctor of Philosophy

2023

ABSTRACT

Atomic mass measurements provide fundamental information about the nature of the nucleus due to the mass lost to binding energy in nucleosynthesis. At the Low Energy Beam and Ion Trapping (LEBIT) facility at the Facility for Rare Isotopes Beams, mass measurements of nuclei across the nuclear chart are performed to improve our understanding of the formation of the elements, explosive astrophysical events, the structure of the nucleus, and even fundamental symmetries of the universe.

Type-I x-ray bursts are particularly complex and exciting sites of nucleosynthesis. A neutron star in a binary system slowly consumes its companion, building up a proton rich crust so hot and dense that it spontaneously undergoes rapid nuclear fusion across its entire surface, generating massive amounts of energy over the course of a few minutes, and emitting powerful bursts of x-rays detectable on earth. Then they do it again every few hours. These events are the site of the rapid proton capture (rp) process. In this work, a high-precision mass measurement of phosphorus-27, an isotope with a 260 ms lifetime—less than the blink of an eye—is discussed. Its impact on the path of the rp process and therefore the energy produced in x-ray burst is investigated using a complex supercomputer simulation. Based on the results, the importance in astrophysics of having precision measurements over theoretical predictions and high performance simulations over simple approximations is discussed.

With the transition from the National Superconducting Cyclotron Laboratory (NSCL) to the Facility for Rare Isotope Beams (FRIB), a plethora of rare isotopes previously beyond the reach of nuclear physicists due to low production rates and short half-lives have become available. To measure the masses of these exotic isotopes, new tools have been implemented at LEBIT. The Phase Imaging Ion Cyclotron Resonance (PI-ICR) Technique is one of these tools, and it has vastly improving experimental sensitivity. As with any technique requiring

parts-per-billions level precision, it is full of complications in hardware, software, and understanding of systematic uncertainties. These challenges and how they have been overcome will be discussed. Finally, preliminary results of PI-ICR proof of effectiveness will be shown: successful PI-ICR mass measurements of two rare isotopes produced by FRIB, the previously known ^{105}Sn and the world's first mass measurement of ^{22}Al.

TABLE OF CONTENTS

LIST OF ABBREVIATIONS ..... **v**

Chapter 1 Introduction **1**

Chapter 2 Mass Spectrometry with Penning Traps **8**

Chapter 3 The LEBIT Mass Spectrometer Facility at the NSCL/FRIB **29**

Chapter 4 ^{27}P Mass Measurement and X-Ray Burst Simulations **37**

Chapter 5 Implementation of PI-ICR at LEBIT **53**

Chapter 6 Conclusion **69**

BIBLIOGRAPHY **70**

APPENDIX A Hardware **79**

APPENDIX B MM8 For PI-ICR **89**

APPENDIX C Software **99**

LIST OF ABBREVIATIONS

NSCL National Superconducting Cyclotron Laboratory

FRIB Facility for Rare Isotope Beams

LEBIT Low Energy Beam and Ion Trap

PTMS Penning Trap Mass Spectrometry

TOF-ICR Time Of Flight Ion Cyclotron Resonance

MCP Microchannel Plate

PI-ICR Phase Imaging Ion Cyclotron Resonance

PS-MCP Position Sensitive Microchannel Plate

FT-ICR Fourier Transform Ion Cyclotron Resonance

FFT Fast Fourier Transform

MR-TOF Multi Reflection Time Of Flight

RF Radio-Frequency

RFQ Radio-Frequency Quadrupole

HV High Voltage

IoI Ion of Interest

TIS Thermal Ion Source

LAS Laser Ablation Source

Nd:YAG Neodymium-doped Yttrium Aluminum Garnet

IMME Isobaric Multiplet Mass Equation

rp **process** Rapid Proton capture process

MESA Modules for Experiments in Stellar Astrophysics

MM8 Mass Measurement 8

SOMA Simple Online Mass Analysis

SWIFT Stored Waveform Inverse Fourier Transform

AFG Arbitray Function Generator

CFD Constant Fraction Discriminator

TDC Time to Digital Converter

NIM Nuclear Instrument Modules

ANL Argonne National Lab gas stopper

ACGS Advanced Cryogenic Gas Stopper

CCF Coupled Cyclotron Facility

AME Atomic Mass Evaluation

ESR Experimental Storage Ring

GSI Helmholtz Centre for Heavy Ion Research

HIRFL-CSR Heavy Ion Cooler-Storage-Ring

Chapter 1

Introduction

When determining the mass of an atomic nucleus, one would—reasonably—assume that it is easy to do; just count the number of protons and neutrons, and sum the masses of these protons and neutrons. If one does this and compares the result to an experimentally measured mass, they will find that a nucleus *always* weighs less than the sum of its parts.

Where did this mass go? Einstein told us with his famous equation $E = mc^2$ that energy and mass are can be converted into one another. In the case of the missing mass in nuclei, mass was converted to binding energy in the process of nuclear fusion. The energy produced by nuclear fusion is used to power stars, like our sun, and hopefully will someday power our homes and cities using fusion reactors.

By measuring the mass of an atom, one can determine exactly how much mass was converted into binding energy during its formation. Knowing this binding energy is important for a wide variety of applications; in advanced studies of nuclear structure, astrophysics, and fundamental interactions masses often must be known to a precision of $\frac{\delta M}{M} \leq 10^{-6}$, 10^{-7}, and 10^{-8}, respectively. When measured to these levels of precision, the mass becomes a valuable tool for quantifying the nucleus and its interactions.

1.1 Introduction to X-ray Bursts

Type-I x-ray bursts are an astrophysical events which occur in binary star systems in which one star has died, leaving a neutron star orbiting an actively burning star. If the gravitational pull from the extremely dense neutron star is great enough, and the radius of the main sequence star large enough, then hydrogen and helium will flow from the companion star to the neutron star. This proton-rich matter accretes on the surface of the neutron star, forming a hot, dense crust.[46]

The neutron star itself is largely inert, but the crust it forms is an excellent site for nuclear fusion. Once enough matter has accreted onto the crust, it becomes dense and hot enough to trigger thermonuclear runaway, during which nuclear fusion reactions generate enough energy to cause more nuclear fusions, leading to the entire surface of the neutron star explosively beginning to fuse. Because the neutron star's gravitational pull is so immense, instead of the crust being blown away by this explosion, it is held in place, the force of the nuclear blast not enough to substantially displace it from the neutron star's surface. Instead, the energy generated from the thermonuclear runaway leads to two important results.

First, the now slightly heavier nuclei in the crust continue to fuse, mostly with hydrogen and helium nuclei, generating still more energy and creating the most proton-rich nuclei naturally found in the universe via the rapid proton capture (rp) process. Second, light in the form of x-rays escapes the neutron star, cooling it. These x-rays are nearly the only thing that can escape the gravitational well of the neutron star; they are the one and only observable astronomers on earth have to probe these extreme astrophysical events. Because they are characterized by a sudden, intense burst of x-rays, as can be seen in data from the first of these events ever measured (Figure 1.1), they have been aptly named x-ray bursts. An "artist's rendition" of an x-ray burst can be seen in Figure 1.2.

X-ray bursts recur periodically because the accretion process in the binary system is not disrupted by the burst. Some x-ray burster systems recur as often as once every 4-6 hours, allowing astronomers to gather enough data to precisely determine the x-ray intensity generated by the burster over time during the events, which last anywhere from 10-1000 seconds, but typically on the order of 100 s [34]. These observations allow physicists to compare computational models of the complex network of nuclear reactions which occur in the burst to real data.

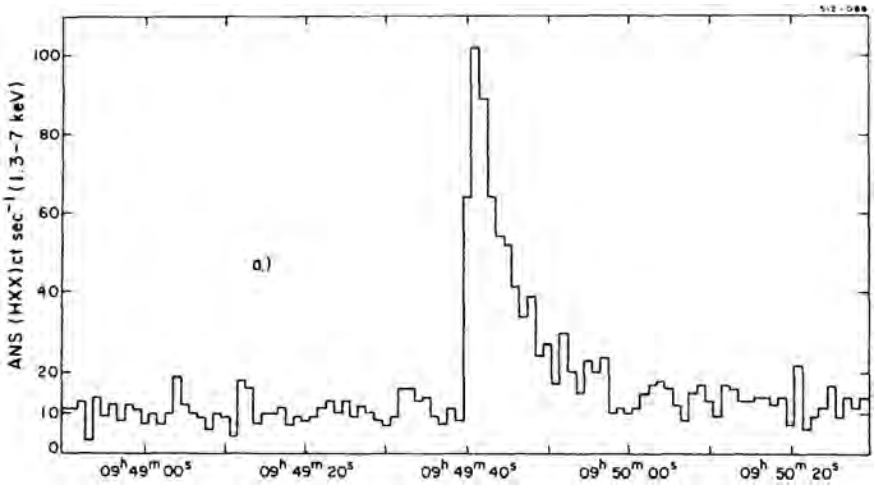

Figure 1.1: The x-ray luminosity over time of the first x-ray burst (XRB) ever detected by humans in 1975 by Grindlay et al. using the Astronomical Netherlands Satellite [23]. The light curve is characterized by a sharp increase in x-ray luminosity followed by a decay back to background levels over the course of about a minute.

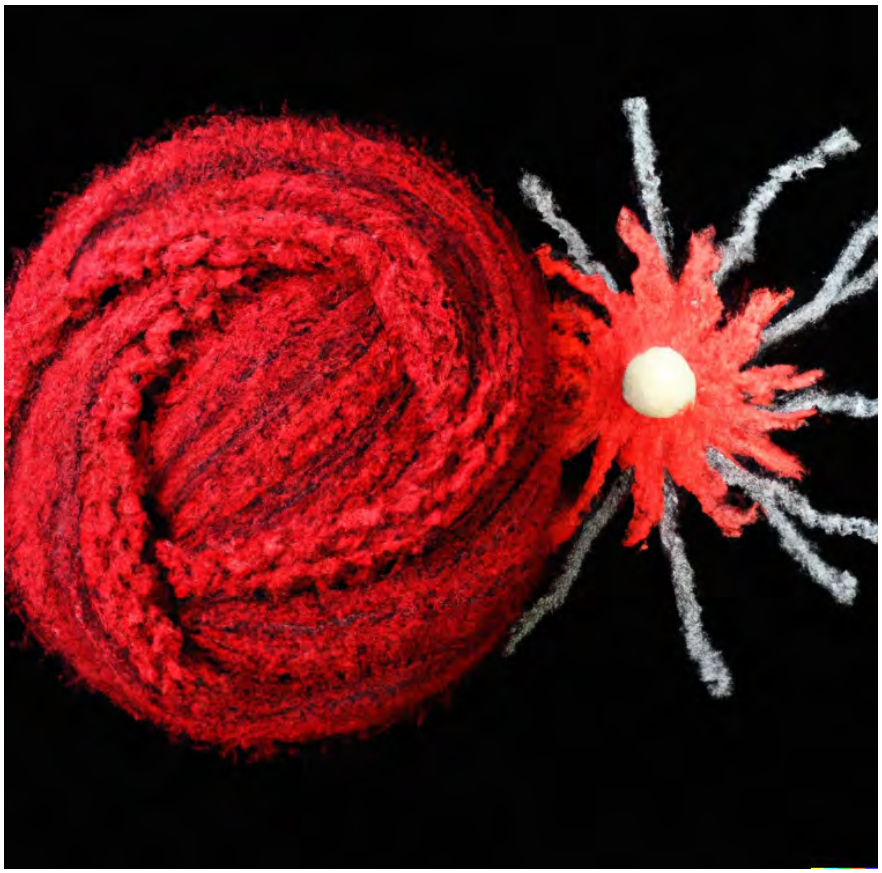

Figure 1.2: The AI DALL-E 2's rendition of an x-ray burst using the prompt "A small neutron star with an accretion disc. The neutron star is consuming a red giant star and generating an x-ray burst. Everything is knitted out of yarn." The Neutron star lies at the center of the center of the XRB on the right, while the star providing proton-rich material for this explosive event is on the left.

These computational models of x-ray bursts use astrophysical and nuclear physics parameters in order to calculate the energy generated by the nuclear reactions which occur during the x-ray burst. The energy generated can be used to determine the surface temperature and x-ray intensity from the bursts, which can be compared to observations. If the results agree, then models of x-ray burst are validated.

With precise enough models, observations of x-ray bursts could be used to determine otherwise unmeasurable characteristics of the x-ray binary system. For instance, a light curve that deviates from expectation could tell observers that mass radius relation of this neutron star differs from the usual [63]. However, such analysis cannot be reliably performed until all of the uncertainties in our computational models of x-ray bursts are reduced to the same level as natural variation in observed bursts, and simulations agree with well understood binary systems. Most of the remaining uncertainties in x-ray burst models are from nuclear physics parameters, such as the masses of certain important nuclei [12].

1.2 Precision Mass Measurements of Rare Isotopes

Atomic mass measurements provide integral data for studying nuclei. High-precision mass measurements, especially of rare isotopes, are key to making meaningful physical predictions about the properties of nuclei, their interactions, and even macroscopic consequences of their interactions. The atomic mass is such a valuable quantity that many techniques have been developed to measure it at a variety of labs. These different techniques are usually divided into two categories: direct and indirect. Indirect mass measurement techniques measure properties of a reaction or decay. They allow one to determine a mass via mass differences, or Q-values. Measuring the energy emitted during a reaction or decay allows one to extract these Q-values and thereby determine the mass of the parent or daughter nucleus. By this process, chains of Q-values have been used to measure masses of exotic isotopes far from the

valley of stability. While this method is still useful for extremely short lived isotopes, the uncertainties are compounded for each Q-value that must be used between the well known reference isotope and exotic isotope of interest, often leading to substantial uncertainty in the mass value.

Direct mass measurement techniques utilize time-of-flight magnetic rigidity (ToF-$\beta\rho$), time-of-flight (ToF), and frequency measurements. The least precise, but most suitable of these methods for very low rate, very short half-life isotopes is the ToF-$\beta\rho$ method. This method determines the nuclear mass by equating the centripetal and Lorentz forces on a nucleus moving through a magnetic system [40]. The ToF-$\beta\rho$ technique has been utilized at the National Superconducting Cyclotron Laboratory (NSCL)'s S800 spectograph [3] as well as several other facilities including SPEG at GANIL [56]. The mass resolution achieved in these experiments are rather low because of their short time of flight, and the relative mass uncertainty $\delta m/m$ is usually limited to about 10^{-6} [40].

Higher resolutions can be achieved by increasing the flight path using cyclotrons or storage rings, like the Heavy Ion Cooler-Storage-Ring (HIRFL-CSR) at Lanzhou [73] and the Experimental Storage Ring (ESR) at GSI [19]. These devices can drastically increase the time-of-flight path by sending ions around the ring many times and measuring the frequency of their revolution, reaching $\frac{\delta m}{m} \sim 10^{-7}$

A recent development in precision mass spectrometry is the multi-reflection time-of-flight (MR-TOF) method. This method traps ions between two electrostatic deflectors in order to extend their flight paths. This method has an exceptionally high mass resolving power of 600,000, so it is frequently used as a beam purifier [15, 72, 71, 49]. It has also been used for mass spectrometry, producing respectable results typically with a mass measurement accuracy around 10^{-7} [49, 33, 42, 37, 4, 59].

The greatest accuracy and precision in direct mass measurement methods are achieved in Penning trap mass spectrometry (PTMS) [14, 64]. Penning traps use strong magnetic fields to probe the cyclotron frequency of an ion, which is inversely proportional to its mass. Penning traps and the measurement techniques which utilize them will be discussed in much greater detail in Chapter 2. Penning traps have achieved relative mass uncertainties of $\delta m/m < 10^{-10}$ for stable ions [47], $\delta m/m < 10^{-8}$ for unstable ions [68], and $\delta m/m$ 10^{-7} for very short lived isotopes with half-lives below 10 ms [62]. There are a plethora of Penning trap mass spectrometry programs at rare isotope beam facilities across the globe, including ISOLTRAP at CERN [7], JYFLTRAP at Jyväskylä [29], SHIPTRAP at GSI [61], CPT at Argonne National Lab [57], TITAN at TRIUMF [31], and LEBIT at FRIB [53].

The Low Energy Beam and Ion Trap (LEBIT) facility at the Facility for Rare Isotope Beams (FRIB) is the only Penning trap coupled to a projectile fragmentation facility. This gives LEBIT access to the widest array of rare isotopes among PTMS facilities. LEBIT has been pushing the limits of rare isotope mass measurements for 16 years, measuring isotopes with half lives less than a third of an eye-blink (¡100 ms) [69] achieving precisions as low as two parts per billion [68]. LEBIT continues to push the limits of precision, introducing new techniques like the single ion Penning trap (SIPT) [26] and phase-imaging ion cyclotron resonance (PI-ICR). These advancements will allow LEBIT to take full advantage of the wide array of exotic isotopes that will be accessible as FRIB comes online.

1.3 Enabling Measurements of Short-Lived Isotopes with Phase-Imaging

FRIB will increase the rate of rare-isotope production by greater than an order of magnitude, but many of the isotopes it will deliver are so far from the valley of stability that they decay within a few tens of milliseconds of their creation. Traditional time-of-flight mass measurements techniques can be used to attempt to measure these isotopes, but the statistics

required to measure the mass of an isotope if parts-per-billion uncertainty levels are required for the relevant nuclear physics application could require gathering data for months at a time. The phase imaging technique reduces the number of measurements required to reach this precision by about 25 times [18], potentially reducing experiment times from months to mere days. PI-ICR achieves this increased precision per measurement by detecting not just the rate at which an ion is oscillating in a Penning trap, but the phase of its rotation as it exits the trap. The technique and its implementation at LEBIT will be discussed in greater detail in Section 2.6 and Chapter 5.

Chapter 2

Mass Spectrometry with Penning Traps

2.1 Penning Trap Basics

Penning traps are able to trap charged particles by combining a homogeneous magnetic field for radial confinement and a quadrupolar electrostatic field for axial confinement. The magnetic field causes ions with any nonzero initial velocity perpendicular to the magnetic field lines to precess about these lines. The rate of this precession is known as the cyclotron frequency, which is related to the mass of the particle as follows:

$$\omega_c = \frac{qB}{m} \tag{2.1}$$

where ω_c is the cyclotron frequency, q is the ion's charge, m is its mass, and B is the magnetic field strength. This relation is how Penning traps are used to precisely determine the masses of ions and other charged particles. As we're ultimately interested in measuring the masses of rare isotopes, for the remainder of this dissertation I will restrict the discussion to ions.

The ion is confined axially using a set of three electrodes arranged to create a static quadrupolar field: two hyperbolic endcaps and one hyperbolic ring electrode. The potential created by these electrodes is

$$V(\rho, z) = \frac{V_0}{4d^2}(2z^2 - \rho^2) \tag{2.2}$$

where V_0 is the potential difference between the ring and endcaps—each of which is kept at the same potential—and d is a geometric trap parameter defined as $d = \sqrt{\frac{\rho_0^2}{4} + \frac{z_0^2}{2}}$. Here, ρ_0 is the minimum radius of the ring electrode and z_0 is half the minimum distance between the two endcaps. The Penning trap and the potential described by equation 2.2 are illustrated in Figure 2.1. It is clear to see from the electrostatic potential which resembles a saddle that positively charged ions are confined axially (z) but not confined radially (ρ), necessitating

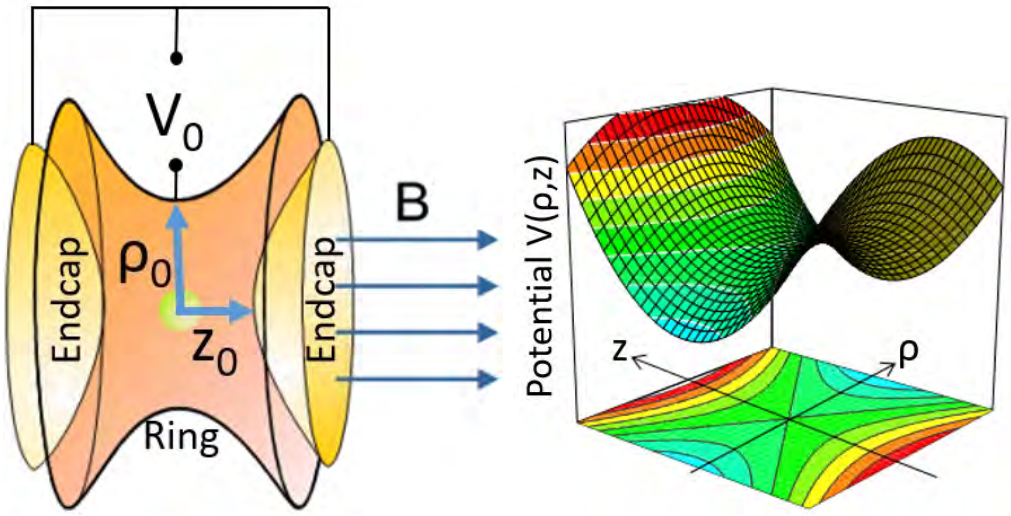

Figure 2.1: Model of a Penning trap composed of a hyperbolic ring and two hyperbolic endcaps (Left) and the quadrupolar electrostatic potential created by them (Right)

the radial confinement provided by a magnetic field aligned with the axial direction. In a real Penning trap the potential is distorted due to holes which must be included in one or both endcaps in order for ions to enter and exit the trap. Additional field imperfections arise from the fact that the hyperbolic ring and endcaps are finite. In order to minimize frequency shifts caused by these field imperfections, correction electrodes are added which generate a field very similar to that created by an ideal Penning trap [21].

2.2 Ion Motion in the Penning Trap

As the mass of the ion is uniquely determined by its motion in the Penning trap, it is critical to understand it. A full derivation of the motion described in this section can be found here [11].

As can be seen in Figure 2.2, motion in a Penning trap consists of one axial oscillation, and two radial oscillations—magnetron and reduced cyclotron motion. The axial motion is generated by the electrostatic field and simply described as a harmonic oscillator with the

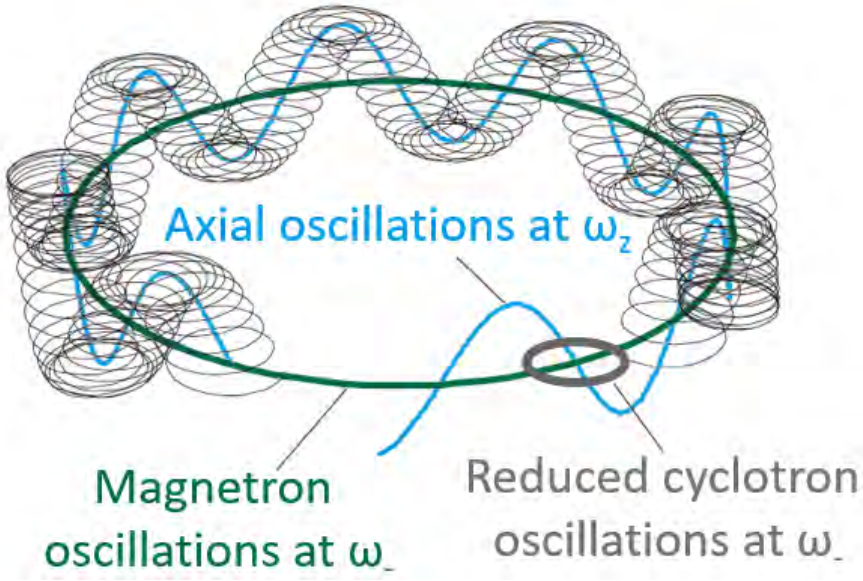

Figure 2.2: Ion motion in a Penning trap split into its three component motions: magnetron, reduced cyclotron, and axial motion

frequency

$$\omega_z = \sqrt{\frac{qV_0}{md^2}}. \tag{2.3}$$

The radial motions are generated by a combination of the magnetic and electrostatic fields. The two radial oscillations have the frequencies ω_+ (reduced cyclotron) and ω_- (magnetron) which are given by the equation:

$$\omega_\pm = \frac{\omega_c}{2} \pm \sqrt{\frac{\omega_c^2 - 2\omega_z^2}{4}} \tag{2.4}$$

In an ideal Penning trap potential, the two radial motions sum to the cyclotron frequency.

$$\omega_c = \omega_+ + \omega_- \tag{2.5}$$

Even in a real Penning trap, equation 2.5 is close enough to correct that it can be used for high-precision measurements and introduces much less error than other systematics [20]. Therefore, it is generally treated as true in all but ultra-high-precision measurements of

stable ions, which must use the invariance theorem [10]

$$\omega_c = \sqrt{\omega_+^2 + \omega_-^2 + \omega_z^2} \tag{2.6}$$

which remains true even in Penning traps with misalignments or distortions. Typical Penning traps have strong magnetic fields and weak electric fields, leading to the frequencies of the three component ions motions having the hierarchy

$$\omega_+ >> \omega_z >> \omega_- \tag{2.7}$$

While in the ideal case of a purely quadrupolar electrostatic and linear magnetic field, these frequencies are immutable, the amplitudes of the radial motions can be manipulated by applying radio frequency (rf)-excitations to the Penning trap's ring electrode [1]. Ring electrodes are usually segmented so that these rf-excitations can be applied at various multipolarities. At LEBIT, for instance, the hyperbolic ring electrode is split into 8 segments, each of which can have a unique sinusoidal signal applied to it. Two common excitation schemes are quadrupolar and dipolar excitations, a diagram of which can be seen in Figure 2.3. A dipolar excitation at either of the trapped ion's radial frequencies ($f_\pm = \omega_\pm/2\pi$) drives the radius of the corresponding motion. This can be used to excite contaminant ions until they collide with the ring electrode, effectively removing them from the system, or just to move an on-center ion to an off center orbit. A quadrupolar excitation at the sum or difference of the two radial frequencies ($f_c = \omega_c/2\pi$ or $f_+ - f_-$) couples the magnetron and reduced cyclotron motion, causing the motion of the ions to convert back and forth between the two as long as the excitation is applied [1].

2.3 Basics of Penning Trap Mass Spectrometry

Penning Trap Mass Spectrometry (PTMS) is the most precise mass measurement method available today. An ion's mass is determined by measuring its cyclotron frequency, ω_c, and

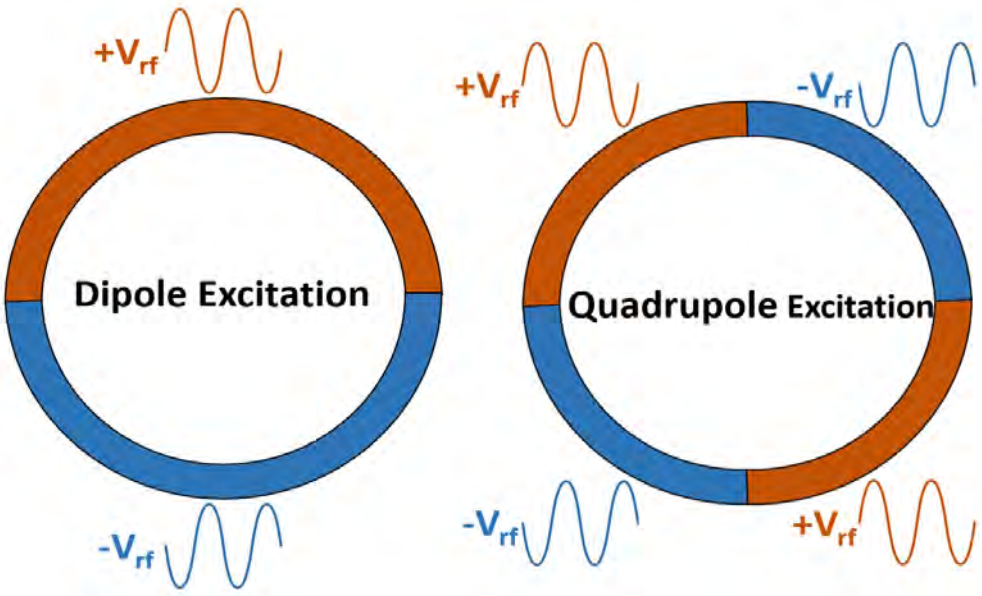

Figure 2.3: The two common types of rf-excitations applied to segmented ring electrodes in a Penning trap to manipulate the motion of trapped ions. The excitations in blue are exactly 180° out of phase from those in orange.

rearranging equation 2.1 to solve for mass.

$$m = \frac{qB}{\omega_c} = \frac{qB}{2\pi f_c} \tag{2.8}$$

This also requires precise knowledge of the ion's charge, q, and the magnetic field, B. Ions arrive from the beam stopping facility with a charge of $q = +1e$ or $+2e$. The magnetic field is determined by measuring the cyclotron frequency of a calibrant ion of well-known mass. Thus with q, m, and ω_c well determined, equation 2.1 can be rearranged and solved for B. Mass measurements of the ion of interest (IoI) are interleaved with these calibrant measurements, and the magnetic field at the time of the IoI measurement is determined via linear interpolation.

All mass measurements are based on the cyclotron frequency ratio between the IoI and the calibrant:

$$R = \frac{f_{c,ref}^{int}}{f_c} \tag{2.9}$$

Here, $f_{c,ref}^{int}$ is the cyclotron frequency of the calibrant (also commonly called the reference ion, hence the "ref" subscript) which has been linearly interpolated to the time of the IoI measurement. f_c is the cyclotron frequency of the Ion of Interest. With R, we can determine the IoI mass using the following equation:

$$m = \frac{q}{q_{ref}}\bar{R}(m_{ref} - q_{ref}m_e) + qm_e \tag{2.10}$$

in which q_{ref} is the calibrant charge state, $\bar{R}$ is the mean of several frequency ratio measurements, m_ref is the calibrant mass, and m_e is the electron mass. Electron binding energies, usually about 10 eV, are typically less than statistical uncertainty, and can therefore be neglected in all but ultra-high-precision measurements. The statistical uncertainty in a measurement is

$$\frac{\delta m}{m} = \frac{\delta f_c}{f_c} = \frac{\gamma}{f_c T\sqrt{N}} \tag{2.11}$$

where T is the observation time, N is the number of detected ions, and γ is a system-dependent constant.

Penning trap mass spectrometers can use three different, well-established measurement techniques, each of which is available at LEBIT. They are, in order from most to least common, Time-of-Flight Ion Cyclotron Resonance (TOF-ICR), Phase-Imaging Ion Cyclotron Resonance (PI-ICR), and Fourier Transform Ion Cyclotron Resonance (FT-ICR). As it is not the subject of any components of this document, FT-ICR will be briefly summarized below.

In FT-ICR, the ions in a Penning trap produce a small but detectable image current on the trap electrodes [38]. The oscillatory signal is a superposition of noise and ion image currents. A Fast Fourier Transform (FFT) is performed on the time-domain signal to produce a frequency-domain spectrum [17]. The image currents produced will appear as distinct peaks

in the frequency domain at oscillatory frequency of the trapped ions. This can be used to measure both the reduced cyclotron frequency (ω_+) and magnetron frequency (ω_-), thus the mass can be determined using equations 2.5 and 2.1.

2.4 The TOF-ICR Technique

The TOF-ICR (Time of Flight Ion Cyclotron Resonance) technique [8] measures the time of flight from the Penning trap to a microchannel plate (MCP) detector, of an ion which a certain quadrupolar RF excitation has been applied to while it was in the Penning trap. If the applied quadrupolar excitation was at or near the ion's cyclotron frequency, f_c, then the initial slow magnetron motion at ω_- will be converted into fast, reduced cyclotron motion at ω_+. The amount of radial energy gained from a perfect conversion of pure magnetron to pure reduced cyclotron motion is easily found by taking the difference in the ion's radial kinetic energy at each frequency:

$$\Delta E_r = \frac{1}{2} m(\omega_+^2 - \omega_-^2)\rho^2 \tag{2.12}$$

When the ion is ejected from the trap, it experiences a force in the axial direction due to the weakening magnetic field as it gets further from the center of the magnet, the peak magnetic field being positioned at the center of the Penning Trap.

$$F_z = -\mu \frac{\delta B}{\delta z} = \frac{E_r}{B_0} \frac{\delta B}{\delta z} \tag{2.13}$$

where F_z is the force in the axial direction pointing from the Penning trap towards the MCP, $\frac{\delta B}{\delta z}$ is the magnetic field gradient the ion is passing through, and μ is the magnetic moment which is equal to $\frac{E_r}{B_0}$, E_r being the radial kinetic energy of the ion and B_0 the central magnetic field strength [6].

Knowing this, it is clear which ions which have had their radial motion converted from magnetron to much much faster reduced cyclotron motion will experience a greater force

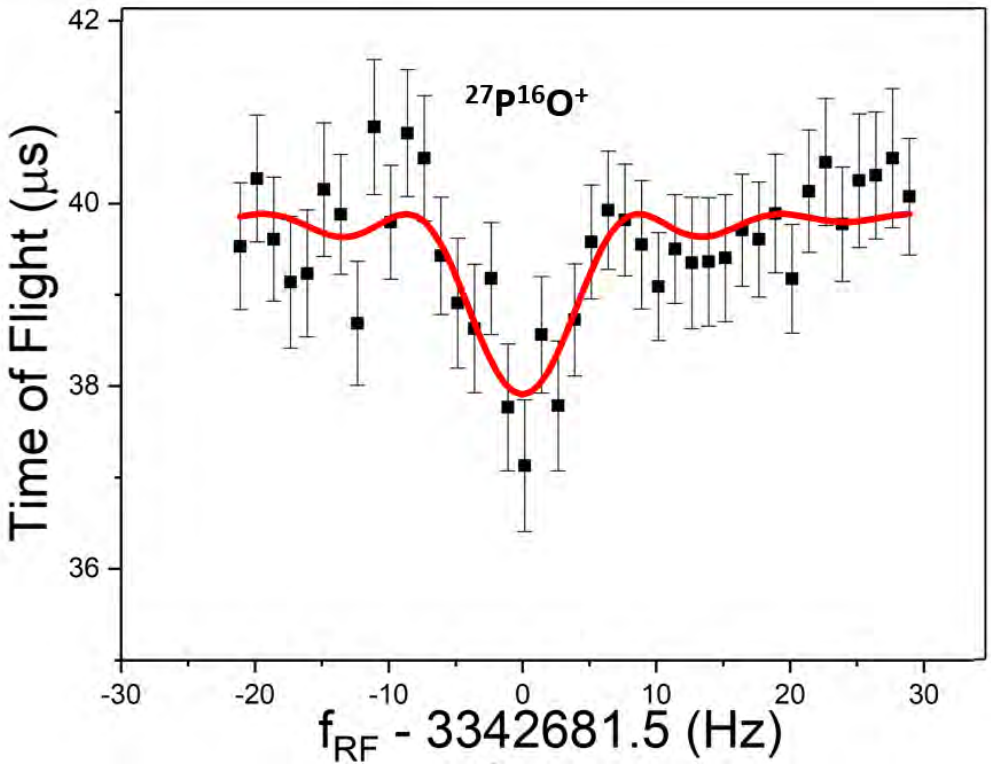

Figure 2.4: Sample 100 ms continuous quadrupolar excitation TOF-ICR resonance of $^{27}PO^{+}$ obtained by scanning f_{rf} applied to $^{27}PO^{+}$ ions prepared with pure initial magnetron motion and measuring time of flight between the Penning trap and an MCP detector. The theoretical fit (red) is calculated in [1]. The minimum corresponds to the cyclotron frequency f_c.

as they travel to the MCP, accelerate faster, and strike earlier than ions with their motion unconverted, or partially converted.

In order to determine an ion's f_c (and therefore mass via equation 2.1), one scans the quadrupolar rf-excitation frequency, f_{rf}, while making measurements of ToF. When ToF is minimized, the conversion was optimal and $f_{rf} \approx f_c$. The exact shape of the ToF distribution is determined by calculating the ToF at each excitation frequency f_{rf} using [1]. An example of the theoretical fit to a ToF distribution is shown in red in Figure 2.4.

In order to achieve full conversion from f_- to f_+, the product of the RF amplitude and excitation time is optimized. This product is species independent and found by varying RF amplitude for a given conversion time until ToF is minimized, indicating full conversion.

The TOF-ICR technique requires >100 ions in order to produce a meaningful response

curve, and, in its traditional form, has the downside that while off-resonance ions are necessary to establish a baseline ToF and generate a full ToF resonance, they do not contribute greatly to knowledge of f_c, and therefore the ion mass. In short, TOF-ICR is a scanning technique where not all points maximally contribute to the determination of f_c. One technique which can be used to increase the knowledge gained from off-resonance rf-excitation values is the Ramsey resonance technique. Instead of applying the full conversion $V_{rf} \times T_{rf}$ in one burst, half of the conversion is applied, then the ions are allowed to freely evolve in the trap for a time $T_{free} = 1.5 * T_{rf}$, after which the second half of the conversion is applied. If $f_{rf} = f_c$ this results in fully converted ions with pure reduced cyclotron motion, just like in the continuously applied rf method. However, when a frequency near but not at f_c is applied, an interference pattern of deep sidebands appears when plotting ToF vs f_{rf}, as can be seen in Figure 2.5.

The theoretical derivation of this interference pattern, and the pattern created by other excitation schemes can be found in [30]. This results in $\sim 3\times$ improvement in precision over the continuously applied quadrupolar excitation technique. The downside to this technique occurs when there are moderate levels of contaminant ions present. Due to the lack of easily definable baseline ToF, the interference pattern can be more difficult to distinguish from noise than the single dip in ToF generated by the traditional method. Therefore, a measurement usually begins with a continuous quadrupolar measurement in order to confirm the presence of the ion of interest and then moves on to the Ramsey method to increase precision.

2.5 Cleaning Contaminants from the Trap

In order to perform any type of measurement, whether TOF, SIPT, or PI-ICR, it is best for all ions not being measured to be cleaned from the trap. This has the benefit of minimizing ion-ion interaction in the trap and increasing signal strength. LEBIT employs 7 different

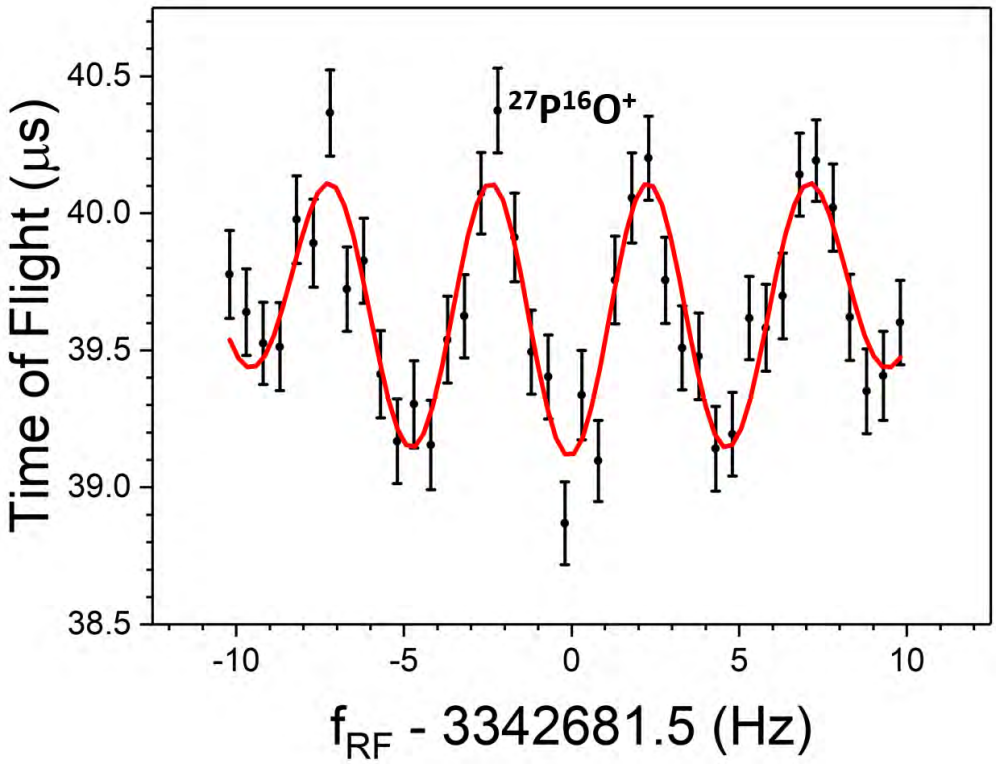

Figure 2.5: Sample 250 ms Ramsey resonance of $^{27}PO^{+}$. Instead of a continuous 250 ms excitation, an excitation scheme of 50 ms RF, 150 ms free evolution, 50 ms RF was applied to generate the above interference pattern. The above theoretical fit (red), and fits for other complex schemes are described in [30]. The central ToF minimum corresponds to the cyclotron frequency f_c.

arbitrary function generators (AFGs) just for the purpose of cleaning. The cleaning AFGs remove contaminant ions from the trap by applying a dipolar excitation of sufficient amplitude at the contaminant ion's reduced cyclotron frequency, $f_{+(contaminant)}$, to increase the radius, $\rho_{+,contaminant}$, such that the ions either collide with the walls of the Penning trap, removing them from the system, or at least have $\rho_{+,contaminant} > 2$ mm, the radius of the exit hole in the Penning trap endcap. If they have this large radius, the ions will collide with the endcap instead of exiting upon ejection from the trap, which would create background signals on the MCP. Five of the cleaning AFGs (affectionately named MrClean 2-6) apply a specific frequency for a fixed duration. These target specific contaminants, usually isobars with the ion of interest, which enter the trap in the pulsed beam from the cooler/buncher. Which contaminants are present and must be cleaned is determined by performing dipolar scans over a broad frequency range and searching for drops in count rate as contaminant ions are excited and driven out of the trap. When a contaminant is identified using this method, the output frequency of one of the five cleaning AFG's is set to its reduced cyclotron frequency.

One cleaning AFG (MrClean 1) applies a cleaning dipolar excitation at the f_+ of a contaminant continuously in the trap instead of for a specified duration. This is useful in the scenario that an ionic contaminant is somehow continuously appearing in the trap, e.g. as a breakup product of weakly bound chemical contaminant.

The last cleaning AFG is the Stored Waveform Inverse Fourier Transform (SWIFT) AFG. Instead of targeting a specific contaminant, SWIFT offers a versatile broadband, mass-selective excitation scheme. It allows the user to simultaneously clean all isobaric contaminant ions with sufficiently different reduced cyclotron frequency from the ion of interest (IoI): $|f_{+(contaminant)} - f_{+(IoI)}| > 400$ Hz. This broad band cleaning occurs without

substantial impact to the count rate or beam spot quality of the ion of interest. SWIFT is a powerful tool for making measurements of the often highly contaminated rare isotope beams arriving from the gas stopper at FRIB. Details on this technique can be found in Kwiatkowski et al.'s paper detailing its development and implementation at LEBIT [32]. SWIFT is the preferred method for cleaning contaminant ions from the trap as it requires no knowledge of what the contaminant ions are, and thus doesn't waste valuable beam time identifying them. However, if a contaminant species is particularly close in frequency to the IoI, then a targeted dipolar excitation is required.

2.6 The PI-ICR Technique

The Phase Imaging Ion Cyclotron Resonance (PI-ICR) technique was invented by the SHIP-TRAP group at GSI [18]. Compared to TOF-ICR, PI-ICR can reach the same levels of precision with an order of magnitude fewer detected ions. In addition, PI-ICR has greater than an order of magnitude increased resolving power compared to TOF-ICR. This additional information comes from one important piece of information: the phase of the ion motion. It is possible to measure this phase using a position sensitive MCP (PS-MCP) detector, which relays the information of where it has been struck by an ion. The position measured using the PS-MCP can be correlated to the phase of the ion motion in the trap. This hardware will be discussed in much greater detail in Section A.

While its implementation is complex, the principles behind PI-ICR are actually quite simple. At its most simplified, PI-ICR can be described as follows: if one can measure an ion's initial phase, ϕ_1, at time $t = t_1$, its phase later, ϕ_2, at $t = t_2$, and know how long phase was allowed to accumulate, $t_{acc} = t_2 - t_1$, they need only divide accumulated phase, ϕ_{acc}, by time in order to determine the angular frequency: $\omega = \frac{\phi_{acc}}{t_{acc}}$. This simplified explanation of the technique can be seen diagrammatically in Figure 2.6. In a Penning trap, ions can

trivially be prepared such that they are initially in state of nearly pure reduced cyclotron (with frequency ω_+) or magnetron (with frequency ω_-) motion, which can both be measured to acquire ω_c via equation 2.5.

2.6.1 Determining Orbit Center for PI-ICR

An angle can only be measured if there is an origin to measure with respect to. This origin correlates to the center of the Penning trap, which the ions are orbiting about. In theory this center can be found by injecting the ions into the trap on-center and then immediately ejecting them. At LEBIT, due to the particulars of ejection optics, the path ions travel from the trap to the position sensitive MCP varies depending on the radius the ions are orbiting at, e.g. if the ions are ejected while on center, they will appear at (-2,-2) (arbitrary units) on the MCP, but if they're ejected with an orbital radius of 2 mm, they'll appear to orbit around (0,0) when projected onto the MCP, striking the detector in a circle (or ellipse) centered at (0,0). The solution to this issue is to find the center of the orbit by painting the entire path "off-center" ions will take, and calculating the center of this path. An example of this path can be seen in Figure 2.7. This elliptical projection of the ion path is achieved by preparing ions at the same radius measurements will be performed at and scanning over t_{acc}. The projected ellipse has been found to minimally deviate from a theoretical ellipse when the ions are prepared with pure magnetron motion and t_{acc} is varied from $t_{acc} = 0us$ to $t_{acc} = \frac{1}{\omega_-}$ in at least 20 steps.

The center of this ellipse can be found quickly by fitting the ellipse using a non-iterative least squared minimization [45]. While it takes longer than simply injecting then ejecting ions on center, this technique provides a far more robust method for determining the center about which ions rotate, and which all phases must be taken with respect to. In addition, this center is quite stable, so during an on-line experiment when time is valuable, one ellipse

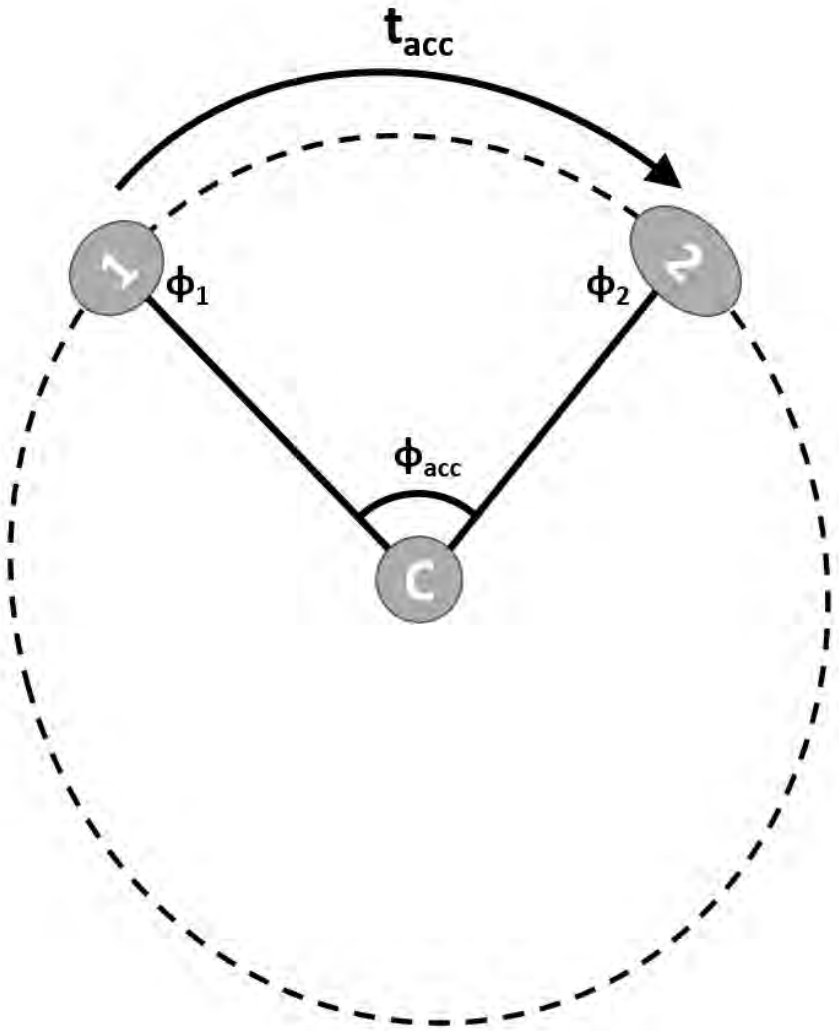

Figure 2.6: The PI-ICR technique. At LEBIT the center, C, is found via elliptical fit to the orbit path projected onto the position sensitive MCP. Spot 1 is the start phase, spot 2 the final phase after the ions have been orbiting for a time t_{acc}. Angular velocity of ion motion is determined by $\omega = \frac{\phi_{acc}}{t_{acc}}$. The image does not convey important fact that, for precise measurement, ions make a large number of full orbits N, in addition to accumulating phase ϕ_{acc}.

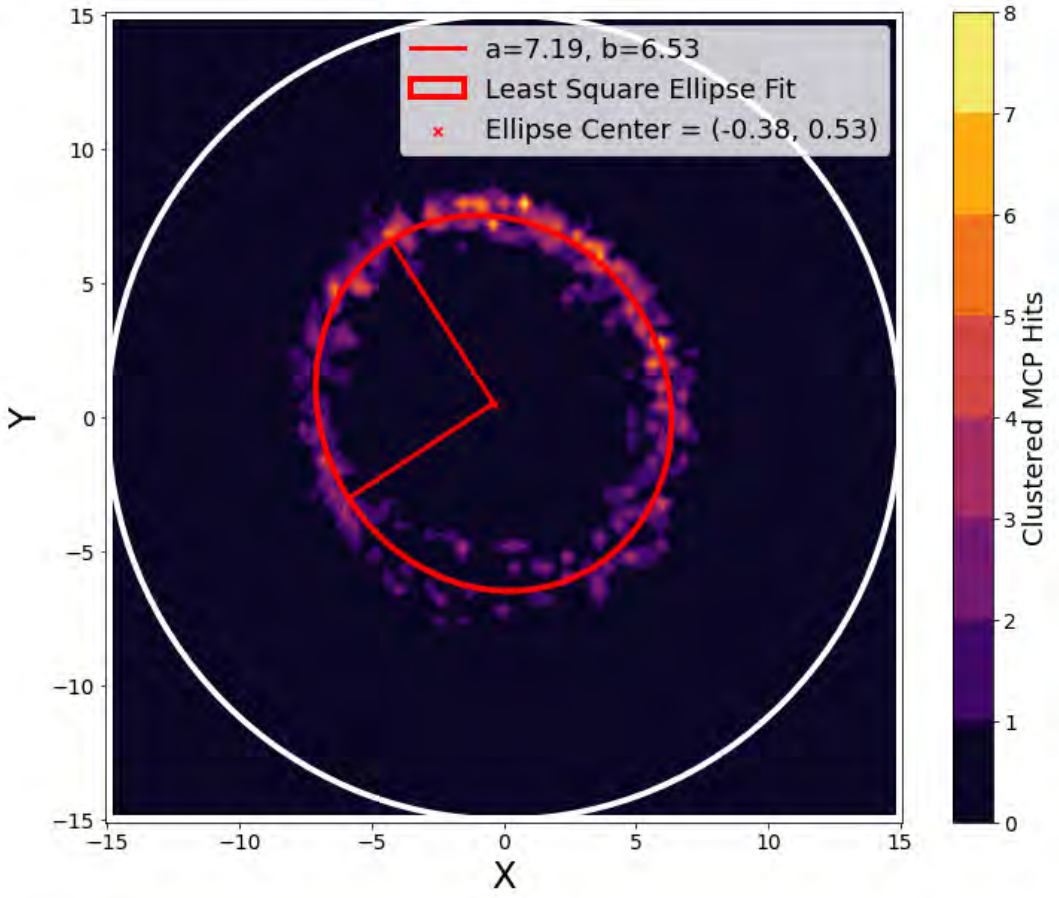

Figure 2.7: Elliptical projection of the circular path ions in the Penning trap follow. An ellipse is fit to the position data using the techniques in [45], and the center of this fit–in this case (-0.38, 0.53)–is used as the origin which all phases in PI-ICR calculations are taken with respect to. "a" and "b" are the radii of the major and minor axes, respectively.

measurement should be taken—usually using a stable isobar to the exotic isotope of interest—immediately before and after the experiment. While this center should shift by at most a negligible amount, it is straightforward to linearly interpolate the center location for each measurement made using the pre-and-post experiment ellipse fits in order to sufficiently account for any drift in the projection of the ions.

2.6.2 Determining Number of Full Turns for PI-ICR

In order to perform a mass measurement of any reasonable precision, t_{acc} must be such that ions in the trap make a large number of orbits, n. Knowing this, the angular velocity measured by PI-ICR is described by

$$\omega = \frac{2\pi n + \phi_{acc}}{t_{acc}}. \tag{2.14}$$

The uncertainty in this frequency is dependent on the angular distribution of the ions forming spots 1 and 2, $\Delta\phi_1$ and $\Delta\phi_2$, the number of ions in each spot, N_1 and N_2, and the phase accumulation time t_{acc}:

$$\Delta\omega = \left(\frac{\Delta\phi_1}{\sqrt{N_1}} + \frac{\Delta\phi_2}{\sqrt{N_2}}\right) \Big/ t_{acc} \tag{2.15}$$

While the number of full turns, n, cannot be measured directly, it can be inferred to be

$$n = floor(\frac{\omega \times t_{acc}}{2\pi}) \tag{2.16}$$

as long a suitable value for t_{acc} is chosen based on how well the frequency to be measured is already known. A good rule of thumb to use when determining the maximum value of phase accumulation time which can safely be used is:

$$\frac{t_{acc}\Delta\omega}{2\pi} = t_{acc}\Delta f < 0.2 \tag{2.17}$$

This ensures that one's knowledge of the frequency would need to be off by $> 5\sigma$ in order for the guess for n to be incorrect. In analysis, however, one should always check if $n+1$ yields a resulting value of ω much closer to the known value, in case the floor function in Equation 2.16 rounded down to a value of n when the un-rounded value was extremely close to $n+1$ *and* the frequency turned out to be higher than the guess, so $n+1$ full turns were actually made. For instance, if the frequency one wishes to measure is known to within $\sigma = 1$ Hz, they can safely use $t_{acc} = 200$ ms. Even for a very poorly known frequency, one can simply make a PI-ICR measurement using a very low value of t_{acc} (e.g. 2 ms) then use the result of this measurement to reduce uncertainty in ω and safely increase t_{acc}.

It may rarely occur that an ion with an uncertain number of nucleons makes it into the trap and needs to be measured; this is unlikely enough that it need not be covered in this document. Should one be in this scenario, see Section 5.5.4 of Rodney Orford's McGill University PhD thesis [44] for a robust strategy on how to proceed.

2.6.3 Excitation Schemes used in PI-ICR

The act of performing PI-ICR involves a series of dipolar and quadrupolar rf-excitations applied to the trap's segmented ring electrodes in order to manipulate the ions in the trap. The exact order and delay between these excitations depends on the spot type (i.e. start phase or final phase, see Figure 2.6) and frequency which is meant to be measured. The different strategies employed by LEBIT at this time will be discussed here, but it is by no means an exhaustive list of potential excitation schemes for PI-ICR.

At LEBIT, there are three different excitation schemes used for PI-ICR: start phase (1), final phase with reduced cyclotron (f_+) phase accumulation (2), and final phase with magnetron (f_-) phase accumulation (-). It is important to note that in PI-ICR, **all excitations and conversions applied are phase-locked**. This means that each time the pulse schemes

in this chapter, Figures 2.8, 2.9, and 2.10, show that an rf is applied, the phase of the applied sine wave produced by the relevant AFG always starts at 0°. A dipole excitation applied to on-center ions with a randomly varying start-phase yields a randomly varying start spot. In practice, this means that no matter what is done to the ions afterwards, if they were excited off-center with a random-phase dipole pulse they will always show up on the PS-MCP evenly distributed about their elliptical projection. If the quadrupolar conversion pulse is applied without phase-locking, it will lead to systematic errors in the measured final phase spot.

If performed correctly, the start phase needs to be measured only once before and once after an experiment for each calibrant and ion of interest. The start phase measurement is the same regardless of whether it will be followed by an f_+ or f_- phase accumulation spot:

1. Ions injected radially on-center, trap's injection side endcap and correction tubes are raised as the ions reach axial trap center.

2. Cleanings, described in Section 2.5, applied to ions to remove contaminants from trap.

3. Ions excited outwards using dipole pulse at ion of interest's f_+. Amplitude of pulse tuned to put the ions at radius slightly less than 2 mm.

4. Quadrupolar conversion pulse at f_c applied to convert fast reduced cyclotron motion at ω_+ to slow magnetron motion at ω_-.

5. Ejection side endcap and correction tube lowered, sending ions to PS-MCP, where ϕ_1 is measured.

The excitation scheme can be seen in Figure 2.8. Regardless of the type of spot being measured, it is vital that the ions are ejected while undergoing pure magnetron motion. This is because ions ejected while oscillating at ω_+ will accumulate a substantial amount of

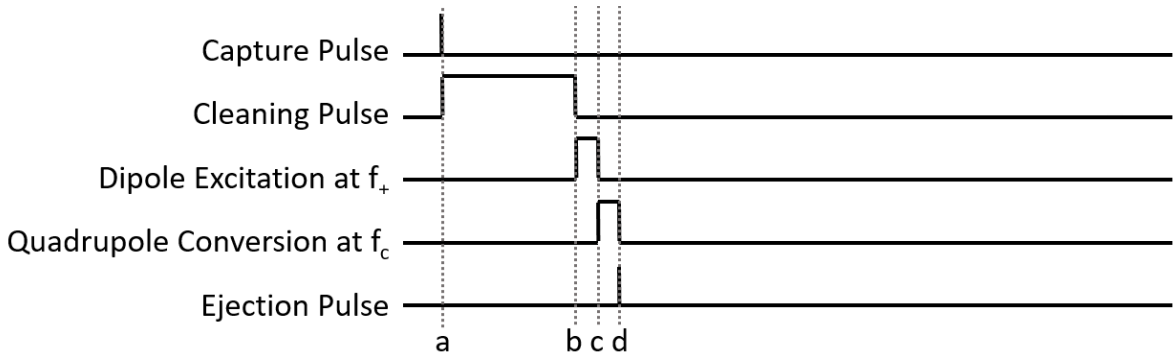

Figure 2.8: Pulse scheme for measurement of the start phase, regardless of whether f_+ or f_- is to be measured. At "a", all injected ions are at the center of the Penning trap, the dipole cleaning pulse will remove contaminant ions while leaving the ion of interest on-center. At "b", the ion of interest is excited outwards, and begins to orbit the center of the trap at it's reduced cyclotron frequency, ω_+. At "c", a quadrupolar conversion pulse at f_c is applied, converting reduced cyclotron to magnetron motion, after which, at "d", the ions are ejected from the trap and the start phase ϕ_1 is measured at the PS-MCP.

phase from even minor axial variations upon ejection. This yields *substantial* smearing on the PS-MCP, often resulting in the full path of the ions being projected instead of a beam spot.

The benefit of this excitation scheme over using a dipolar excitation at f_- to measure an f_- start phase, and f_+ to measure an f_+ start phase is that one need take only a single start phase per ion being measured. f_- and f_+ final phase measurements share this start phase. This is possible because the amount of phase offset caused by the dipolar excitation at f_+ and quadrupolar conversion at f_c is constant, regardless of when they are applied. Therefore, in order to measure a final phase a delay must be added to the pulse scheme, between "b" and "c" to allow reduced cyclotron phase to accumulate, or between "c" and "d" to allow magentron phase to accumulate.

To measure ω_-, a delay of t_{acc-} is added after the ion motion has been converted to pure magnetron, between "c" and "d". Equation 2.14 is applied

$$\omega_- = \frac{2\pi n_- + \phi_{acc-}}{t_{acc-}} \tag{2.18}$$

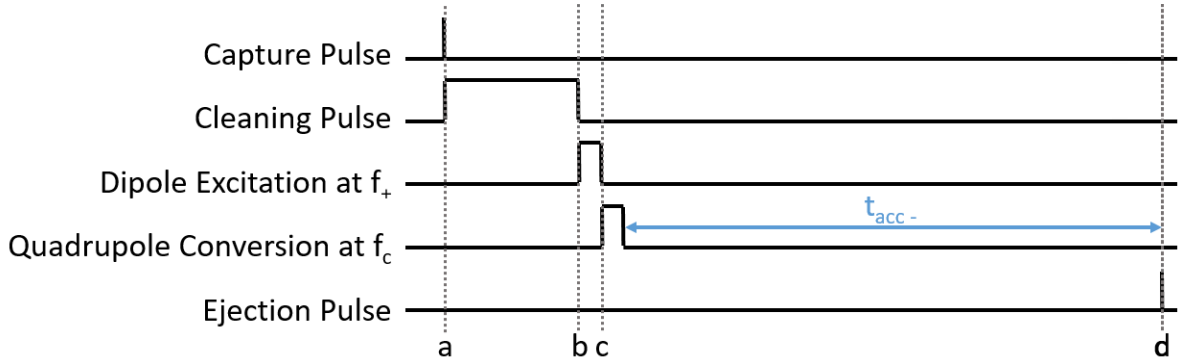

Figure 2.9: Pulse scheme for measurement of the final phase in a measurement of f_-. This scheme is identical to that in Figure 2.8 except that the delay t_{acc-} is added between "c" and "d". The ejected ions form a beam spot with phase ϕ_2 on the PS-MCP.

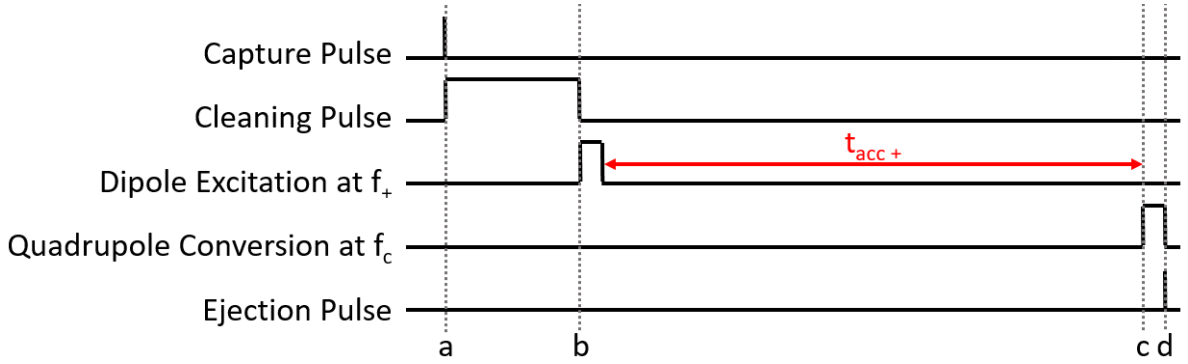

Figure 2.10: Pulse scheme for measurement of the final phase in a measurement of f_+. This scheme is identical to that in Figure 2.8 except that the delay t_{acc+} is added between "b" and "c". The ejected ions form a beam spot with phase ϕ_2 on the PS-MCP.

where ω_- is the magnetron angular frequency, n_- is the number of full turns the ion accumulated while undergoing pure magnetron motion during t_{acc-}. t_{acc-} is the user defined delay *added* between "c" and "d". Note this is NOT the amount of time between "c" and "d", as this would include the time the quadrupolar conversion at f_c is being applied, which must be subtracted off, as it is already included in the start phase. ϕ_{acc-} is the phase difference between the final and initial spot $\phi_{acc-} = \phi_2 - \phi_1$. The scheme can be seen in Figure 2.9

To measure ω_+, a delay of t_{acc+} is added after the ion motion has been converted to pure reduced cyclotron motion, between "b" and "c". The scheme can be seen in Figure 2.10.

Equation 2.14 is again applied

$$\omega_+ = \frac{2\pi n_+ + \phi_{acc+}}{t_{acc+}} \tag{2.19}$$

Again, it is important that t_{acc+} is the delay *added* between "b" and "c", not the total amount of time between them.

Another **important** difference between a magnetron and reduced cyclotron final phase measurements at LEBIT is that these two motions accumulate phase in the **opposite direction**. The two radial motions occur in the same direction, but the quadrupolar conversion pulse inverts the accumulated phase of the reduced cyclotron motion [43] so it can be treated as if it were advancing in the opposite direction as the magnetron motion. Therefore, $\phi_{acc+} = \phi_1 - \phi_2$.

To reiterate this important point:

$$\phi_{acc-} = \phi_2 - \phi_1 \tag{2.20}$$

$$\phi_{acc+} = \phi_1 - \phi_2 \tag{2.21}$$

With all of this info, equation 2.5 and 2.1 are used to convert ω_- and ω_+ to mass, and voila! PI-ICR has been performed.

Chapter 3

The LEBIT Mass Spectrometer Facility at the NSCL/FRIB

The Low Energy Beam and Ion Trap (LEBIT) facility is a high-precision mass spectrometry facility located at the Facility for Rare Isotope Beams (FRIB) on the campus of Michigan State University in East Lansing, MI. FRIB is a brand new, state of the art facility, designed to be the most powerful heavy-ion accelerator on earth, generating isotopes further from stability than ever produced on earth. The vast majority of the work done for this thesis was conducted at the previous accelerator facility, the National Superconducting Cyclotron Laboratory (NSCL), discussed below. However, LEBIT is fully equipped and prepared for the exciting new capabilities and challenges of the FRIB era.

3.1 Delivery of Rare Ion Beams at the NSCL

Rare isotopes were produced at the NSCL by Coupled Cyclotron Facility (CCF). The CCF, as its name implies, is a pair of cyclotrons, the K500 and K1200, connected and able to produce fully stripped ions travelling at $\sim$50% the speed of light. Primary beams are produced with electron-cyclotron resonance ion sources [36] and injected into the K500, which accelerats the beam to about 10 MeV/u. Beams are then extracted and sent to the larger cyclotron, the K1200, where a stripper foil near the center of the cyclotron strips most of the electrons from ions in the beam. This highly charged ion beam is accelerated to about 100 MeV/u. This beam, now travelling at about half the speed of light, is impinged onto a beryllium target, causing ions in the beam to undergo projectile fragmentation, breaking up into a variety of rare isotopes. In order to select the isotope of interest from this slurry of rare-isotopes, this cocktail beam is sent to the A1900 fragment separator [41].

The A1900 is composed of four dipole magnets, twenty-four quadrupole magnets, and an energy degrading wedge. The first two dipole magnets select the isotope of interest by

magnetic rigidity $B\rho = p/q$, where B is the dipole magnetic field strength, ρ is the radius of the ion's motion, p is the ion momentum, and q is the charge. The beam is then passed through the energy degrading wedge, creating an atomic number dependent momentum separation for ions in the beam. Finally, the beam is sent through a second pair of dipole magnets, again selecting on magnetic rigidity. This beam, now a much more pure beam of the rare isotope of interest, could be sent to any of the experimental setups at the NSCL. When being sent to LEBIT, the secondary beam's next destination is gas stopping.

The gas stopping facility slows ions from half the speed of light to room temperature where LEBIT, and other high-precision experiments, can successfully capture, manipulate, and measure them. The NSCL has two helium-filled gas stoppers: The Argonne National Laboratory cell (ANL) [65], the Advanced Cryogenic Gas Stopper (ACGS) [35]. The basic principles of each gas stopper are the same, therefore just ANL, the gas stopper used in the mass measurement of ^{27}P will be discussed here.

First, the rare-isotope beam delivered from the A1900 is slowed down using uniform, precision metal degrader plates, then dispersed on a monochromatic wedge. Without these plates and wedge, the momentum distribution of the beam from the A1900, $\Delta p/p \approx 2\%$, would be too great for all of the beam to be efficiently stopped in a gas. They are then stopped in ultra-pure helium gas. In the stopping process, the ions generally capture electrons until they reach a 1^+, or occasionally 2^+, charge state, at which point it would become energetically unfavorable for the strongly bound helium electrons to be lost to the exotic ions. An electrode structure in the gas stopper provides a combination of DC gradient and RF field which simultaneously keeps ions from colliding with the walls of the chamber and guides them towards an extraction hole. The extraction hole is followed by a radio-frequency quadrupole (RFQ) ion guide which spans three differentially pumped chambers,

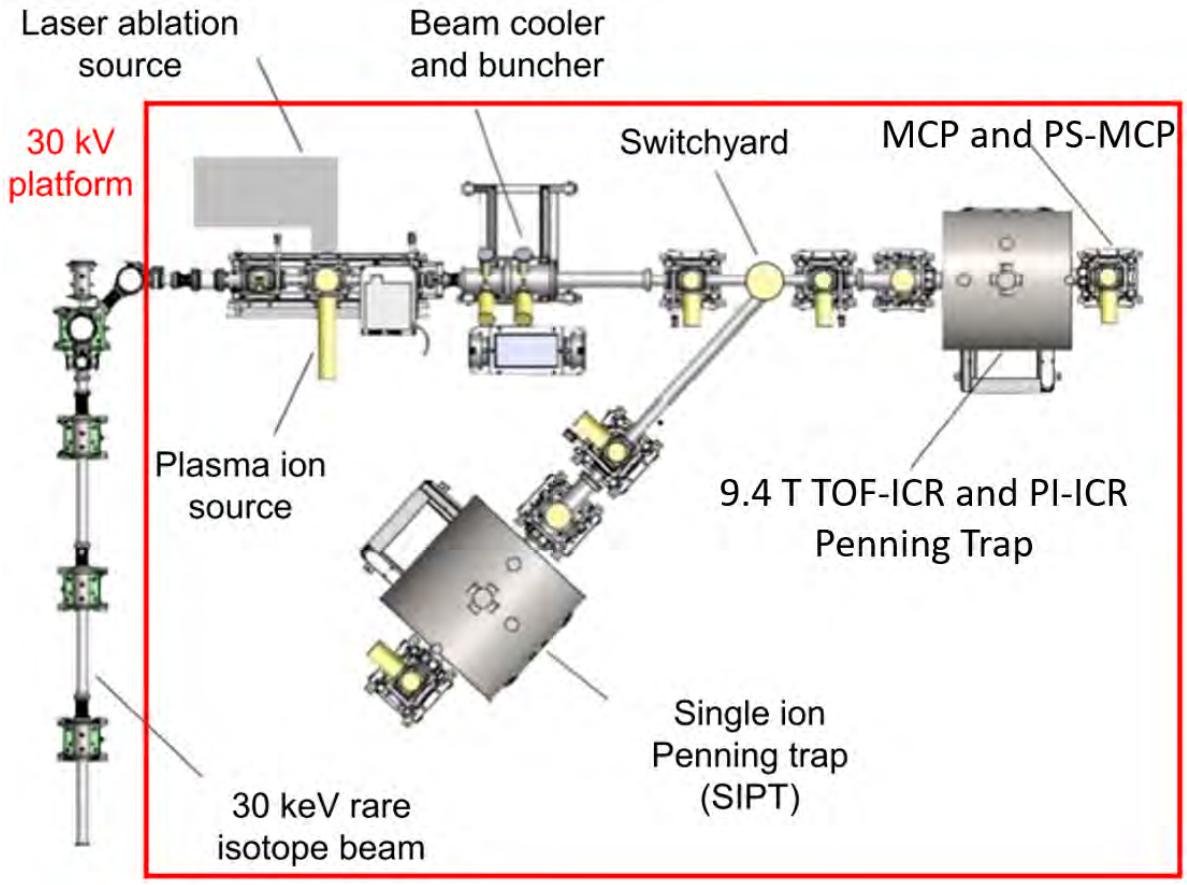

Figure 3.1: Layout of the Low Energy Beam and Ion Trapping (LEBIT) facility. Adapted from [26]

which gradually reduce pressure as the ions leave the gas stopper. The ANL gas stopper is mounted on a 30 kV platform, so the ions enter an accelerating section which transitions the ions to a beam pipe at ground, accelerating the ions to 30 keV/Q. Before they are finally sent to LEBIT, these ions pass through a magnetic dipole mass separator with a set of adjustable slits, which provides a mass resolving power around 1500, allowing for some ion filtering within the same A/Q as the isotope of interest.

3.2 The Major Components of LEBIT

A schematic of LEBIT's layout can be seen in Figure 3.1.

Continuous ion beams are delivered from the gas stopping facility at an energy of 30 keV/Q. In order to slow the ions so that they can be finely manipulated, all of the equipment

in the LEBIT facility sits on a high-voltage (HV) platform, in red in Figure 3.1. When not receiving beam from the gas stopping facility, LEBIT sits at ground, making it possible to work in the lab while it is in operation. When receiving beam from the gas stopping facility, both facilities are connected to the same HV power supply, while base potential of the ion-beam transport system connecting the two is ground. This setup ensures that short lived beam is rapidly delivered from gas-stopping to LEBIT, but slows down to precisely the low energy it attained in the gas stopping facility once it arrives in LEBIT. An additional DC offset can be applied to the LEBIT HV platform in order to fine-tune the energy of the incoming beam. The first destination of this beam after it has been decelerated is the LEBIT cooler and buncher (often called cooler/buncher) [60]. The ion bunches are then sent to either the 9.4 T magnet for TOF-ICR or PI-ICR to be performed, or around a 115° bend to the single ion Penning trap (SIPT) [26].

3.2.1 Offline Ion Sources

When not receiving beam from the gas stopping facility (which is most of the time), LEBIT still must be able to continuously test its functionality, improve existing hardware, and install and validate upgraded hardware. To further these goals, LEBIT has two offline ion sources, a thermal ion source (TIS) and a laser ablation source (LAS) [28]. These offline sources are occasionally useful in an online experiment as a source of stable calibrant ions of well-known mass. The TIS is essentially a thin tungsten filament encased in a ceramic chamber with a gas inlet, which a large current can be run through in order to heat the filament. In addition to the current drive, a positive or negative voltage bias can be applied to the filament. A positive bias is useful for driving off alkali metal impurities in the tungsten, producing positive ions. Greater than 90% of measurements performed at LEBIT are of $^{39}K^{+}$ simply because it is so easy to produce in this manner, and the rest of the system is tested and

calibrated using it. If the filament is biased negatively, it will ionize any gas which has been added to the ceramic TIS chamber and suppress surface-ionized alkali ions.

The LAS uses a pulsed neodymium-doped yttrium aluminum garnet (Nd:YAG) Quantel Ultra laser to produce laser pulses of green 532 nm light to irradiate a solid target, producing ions. The solid target is mounted to a target holder which uses a stepper motor to keep the target rotating continuously while its surface is being ablated by the laser. This prevents the laser from boring a hole straight through the target. It also allows for two different targets to be simultaneously mounted to the target holder, and to remotely switch which target is being ablated at a given time. The LAS is not only important as a source of reference ions, but has recently been used to produce ions for high-precision measurements for ultra-low Q value [55] and highly forbidden [54] β-decay studies of merit without requiring an online beam at all.

3.2.2 The Cooler/Buncher

In the cooler/buncher, the beam is cooled via collisions with room temperature helium, and bunched, i.e. converted from a continuous to a pulsed beam by gathering incoming ions in an electromagnetic well, and periodically releasing them for capture in the Penning trap.

More technically, the cooler/buncher is a three-stage, gas-filled linear Paul trap. The Paul traps utilize a radiofrequency quadrupolar (RFQ) field to radially confine the ions, while a DC electrostatic field transports and confines them axially [60].

In order to fine-tune the ions' energies such that they stop when they reach the center of the Penning trap, a voltage-pulsed drift tube is used immediately after the buncher. Ions enter a long drift tube, $\sim$ 1 m in length, which is held at a potential V1. When the ion bunch is approximately in the middle of the drift tube the potential is switched to 0V, resulting in an energy adjustment of -V1/Q. This is adjusted until the average ion has a kinnetic energy

equals the potential energy at trap-center, minimizing the axial oscillations of trapped ions.

3.2.3 The 9.4 T Penning Trap

After exiting the cooler/buncher, but before entering the magnetic field which houses the Penning trap, the ions pass through a time-of-flight gate in order to pre-filter contaminant ions which have a different mass-to-charge ratio, A/Q, than the ions of interest. Because all ions in the buncher have been thermalized to the same kinetic energy, ions with a different mass, have a different velocity $E_k = \frac{1}{2}mv^2$. The time-of-flight gate is a steering element which takes advantage of this by steering all ions sharply into the wall with a 1 kV potential, except for during an $\sim$ 500 ns period when the element is instead grounded, allowing ions to pass. It is straightforward to calibrate the time between an ion pulse's release from the buncher, and when this gate should be lowered in order to allow only ions of the desired A/Q to pass.

After the time-of-flight gate, the ions pass through three Einzel lenses to focus them as they enter the magnetic field. In the magnetic field, a set of injection optics guide the ions to the Penning trap entrance hole while reducing their energy to minimize axial oscillations once the ions have been captured in the trap.

Immediately before the trap, Lorentz steerers, allow for precise control of injection into the trap [50]. They utilize the $\vec{E} \times \vec{B}$ drift motion of the ions in the strong magnetic field to place the ions at a desired location radially in the trap. For TOF-ICR, the Lorentz steerers are used to inject the ions off-center with pure magnetron motion. For PI-ICR, this means injecting the ion exactly on-center with no initial magnetron motion; in Section 5.1 this will be shown to be vital in eliminating systematic errors related to initial magnetron motion.

The Penning trap, housed in the 9.4 T magnet shown in Figure 3.2, consists of a a hyperbolic electrode structure with correction tube and ring electrodes included to allow for

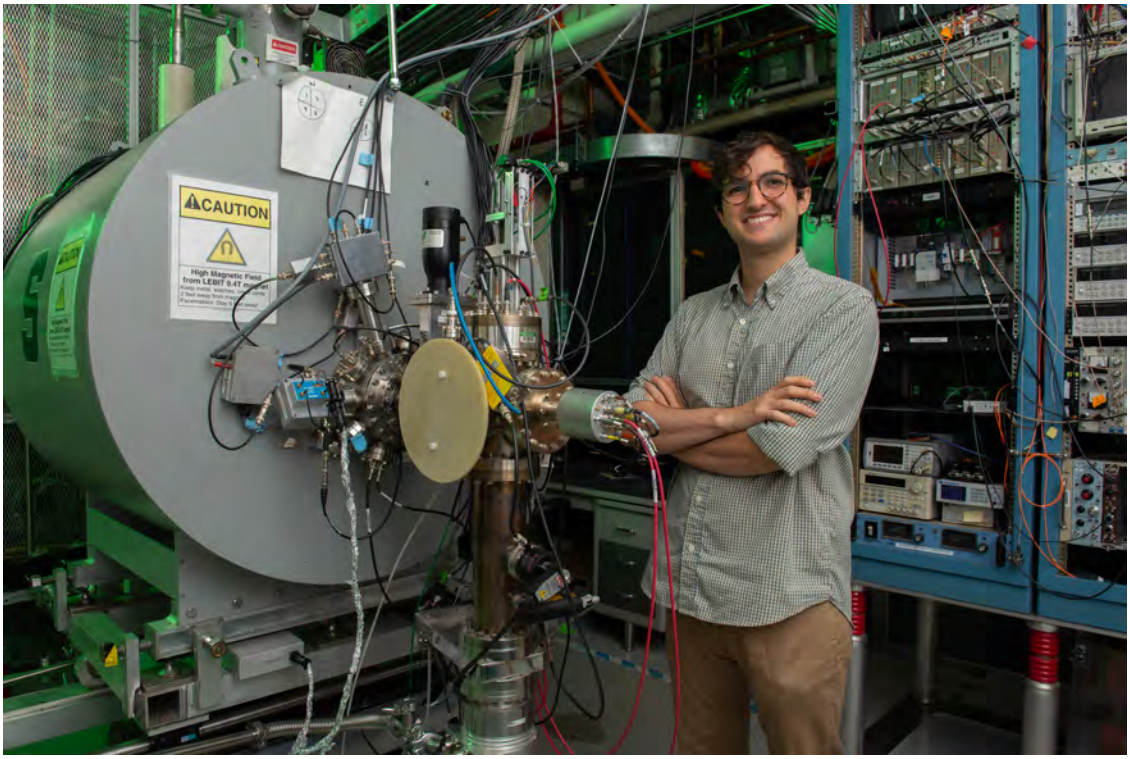

Figure 3.2: The 9.4 T magnet which houses the Penning trap (left) used for TOF-ICR and PI-ICR with the author of this document for scale (right)

field corrections approaching a true quadrupolar electrostatic potential [51]. The endcap and correction tube electrodes have $r = 2$ mm holes in them in order to allow for injection and ejection on either side of the penning trap.

Once the ions are ejected, they travel through a series of drift tubes which accelerate the ions to the detector. In the case of TOF-ICR, the ions are ejected slowly, relying in part on the force of the magnetic field's reduction in amplitude to accelerate the ions. This maximized the impact of the radial energy gain on time of flight. These ions then strike an MCP mounted in a Daly configuration [13] to improve detection efficiency. The positive ions are guided to the strongly negatively biased Daly collector. When ions strike the Daly collector, a shower of electrons is generated, which is picked up by the MCP. The time between trap ejection and MCP signal is recorded, this is the time of flight.

In the case of PI-ICR, the ions are rapidly ejected in order to minimize the amount of

additional ion phase accumulation on the path from the trap to the PS-MCP. The Daly collector and MCP are retracted, and replaced with a drift tube immediately before the PS-MCP, which is in-line with the beam. While detection efficiency is $\sim 2-3\times$ lower without the Daly configuration, position information is lost when ions strike a Daly collector so it cannot straightforwardly be used with a PS-MCP. Ejection optics and detector operation will be discussed in detail in Chapter 5 and Appendix A.

Chapter 4

^{27}P Mass Measurement and X-Ray Burst Simulations

4.1 Motivation for Mass Measurement of ^{27}P

The motivation behind a high-precision mass measurement of ^{27}P is to reduce the uncertainty in simulations of type-I x-ray bursts. The concepts behind these astrophysical events are introduced in Section A.4, so we will jump directly into more technical details here. The relevant nuclear process which governs the energy production in an x-ray burst is the rapid proton capture (rp) process. The specific conditions of an x-ray burst—high temperature around one GK and high proton density around 10^6 g/cm^3—are the required conditions for the rp process to occur. The rp process produces neutron-deficient nuclei lighter than A$\sim$106 via a series of proton captures (p,γ), photodisintegrations (γ,p) α captures (α,p) and β^+-decays. The exact rp process path is dependent on a large number of these reaction rates. Of particular importance is the determination of the intensities of (p,γ)-(γ,p) reactions at "waiting point nuclei"—which have relatively long half-lives of at least a few seconds—which determine the direction of the flow at these nuclei.

In order to accurately simulate x-ray bursts, nuclear data for the isotopes along the rp process reaction pathway are critical. For some isotopes, slight changes in mass result in a change in direction of the (p,γ)-(γ,p) flow due to the exponential dependence of photodisintegration on Q-value as can be seen in equation 4.1.

$$\lambda_{(\gamma,p)} = 2\frac{G_f}{G_i}\left(\frac{\mu kT}{2\pi\hbar^2}\right)^{\frac{3}{2}} exp\left(-\frac{\mathbf{Q_{(p,\gamma)}}}{kT}\right)\langle\sigma\nu\rangle_{(p,\gamma)} \tag{4.1}$$

This flow change can lead to a significant shift in the energy production and therefore shape of the light curve. A sensitivity study by Schatz and Ong [58] looked at the dependence of x-ray burst models on the uncertainty of nuclear masses on and around the rp process path.

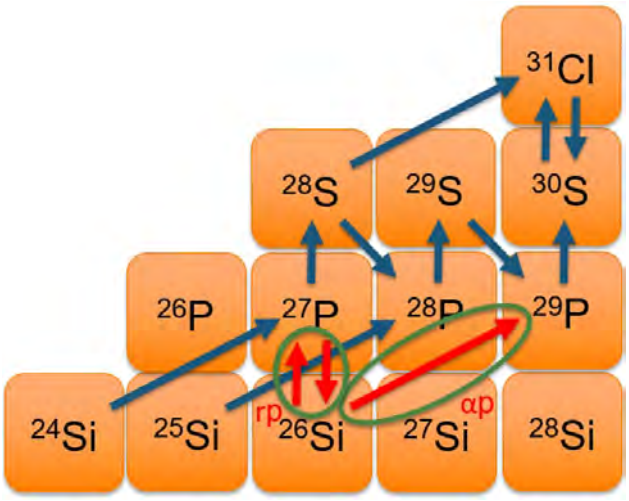

Figure 4.1: *rp* process path near the 2.25 s ^{26}Si waiting point, the reactions of interest are indicated by the red arrows with green circles. The *rp* process competes with the αp process as an escape to this waiting point.

The study used a one-zone x-ray burst model to identify the isotopes whose uncertainties had the greatest effect on the light curve by increasing and decreasing the mass of each isotope by 3σ and visually inspecting the resultant light curves.

Schatz and Ong identified ^{27}P as one of three nuclei which had a measurable effect on the light curve of a typical hydrogen/helium burst. The mass used in the study was the Atomic Mass Evaluation 2016 (AME2016) reported mass excess of -722.5±26.34 keV. The mass of ^{27}P is necessary to determine the equilibrium of the $^{26}\mathrm{Si}(p,\gamma)^{27}\mathrm{P}$ – $^{27}\mathrm{P}(\gamma,p)^{26}\mathrm{Si}$ reaction, which is important to determine the branching between proton capture (p,γ) and α capture (α,p) on ^{26}Si, a waiting point in the *rp* process with a β^+ decay half-life of 2.25 s. The pathway competition in the *rp* process is shown in Figure 4.1. The predicted magnitude of this effect can be seen in the left side of Figure 4.2. While the changes in the simulation may seem small, any remaining x-ray burst uncertainties that are detectable simply by visual inspection are significant. The reduction of the burst simulation uncertainties from ^{27}P's mass to an inconsequential level required a mass measurement with an error of ∼1 keV.

As can be seen on the right side of Figure 4.2 Schatz and Ong also used the Isobaric

Multiplet Mass Equation (IMME) [70] to attempt to reduce the uncertainty in the mass of ^{27}P, and predicted the mass excess to be -716±7 keV. An additional motivation for a precision mass measurement of ^{27}P is to evaluate the predictive capabilities of the IMME, and determine whether it should be used in a predictive capacity for nuclear astrophysics.

4.2 The Isobaric Multiplet Mass Equation (IMME)

Isospin symmetry was posited by Heisenberg in 1932 as a formalism to address the similarities of the neutron and proton in nuclear physics [27]. This formalism treats the proton and neutron as degenerate states of the same hadron which are simply different projections of the new quantum number, isospin: T. The free neutron has isospin projection $T_z = +1/2$, and the free proton $T_z = -1/2$. In a nucleus with $A = N + Z$ nucleons, isospin coupling yields $T_z = (N - Z)/2$, and allows states $T = |T_z|, |T_z| + 1, ..., A/2$. Isotopes with the same number of nucleons, A, i.e. isobars, can have states with the same isospin, T, and similar properties. These are called isobaric analog states, and knowledge of some isobaric analog states can be used to predict properties of of other isotopes in the same isospin-degenerate multiplets.

If isospin symmetry were a true symmetry, all members of a multiplet would have identical mass. However, neutrons and protons have neither identical mass, nor charge, breaking isospin symmetry. Perturbation theory can be used to calculate a correction to the masses of isobaric analogue states in a multiplet, even with the broken isospin symmetry. Some of these states will be excited states of the isobars, which is fine as long as the excitation energy of the isobaric analogue state is well measured. To first order perturbations, this yields the isobaric multiplet mass equation (IMME) [70]:

$$BE(A, T, T_z) = a(A, T) + b(A, T)T_z - c(A, T)T_z^2 \tag{4.2}$$

where BE is the nuclear binding energy, a positive representation of the mass excess, A is the number of nucleons, T and T_z are the isospin and its projection, and a, b, and c are coefficients determined theoretically, or by fitting to mass measurements. The negative sign in front of c is included so that these coefficients are all positive.

Certain nuclear properties, such as second-order Coulomb effects, three-body interactions, and isospin-mixing require the addition of the term dT_z^3, but the d coefficient is expected to be comparatively small in magnitude unless there is a substantial breakdown of isospin symmetry [67]. Attempts have been made to theoretically predict the cubic d coefficient of the IMME, and while having some agreement with experimentally measured d-coefficients, there are several outlier masses which have required large, difficult to predict d-coefficients in order to properly describe the masses of an isospin multiplet [16].

The IMME has been used in nuclear astrophysics to generate models that involved isotopes of unmeasured or poorly measured mass. For ^{27}P, Schatz and Ong utilized IMME to reduce the uncertainty in their predicted light curve, as can be seen in Figure 4.2, the IMME predicted mass uncertainty of 7 keV [58] was substantially better than the AME2016 uncertainty of 26.3 keV, with a 1σ consistent value for the mass excess.

If the result of a high-precision mass measurement, such as the one performed at LEBIT, showed good agreement with the IMME prediction, it would be a piece of evidence in favor of using the IMME in a predictive manner when some members of an isospin multiplet are well measured, but some are not. Theoretical predictions of the magnitude of the d-coefficient [16] specifically for the $A = 27$, $T = \frac{3}{2}$ isospin quartet yield $d < 1$ keV, so deviation from the quadratic version of the IMME should be minimal. For an isospin quartet, requiring a d-coefficient would eliminate the predictive capacity of the IMME, as has four coefficients to fit four masses, guaranteeing a perfect fit, but requiring all four masses to have already

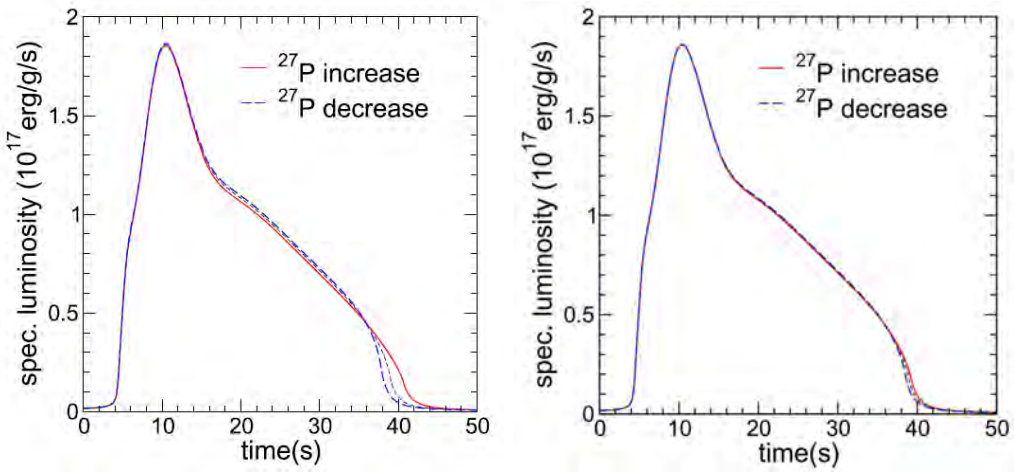

Figure 4.2: Single-zone 1-D type-I XRB light curve model using AME2016's mass (left) vs the IMME predicted mass (right) for ^{27}P. The XRB simulation has been re-run with the only changes being the mass of ^{27}P increased by 3σ (red), or decreased by by 3σ (blue). 3σ = 21 keV (left), 79 keV (right)

been well measured.

4.3 Experimental Procedure

In this experiment, short-lived ^{27}P was generated by impinging 150 MeV/u ^{36}Ar on a 1034 mg/cm^2 Be target at the Coupled Cyclotron Facility at the NSCL. The beam produced was then sent through the A1900 fragment separator with a 150 mg/cm^2 99.99% pure aluminum wedge [41] to separate the secondary beam.

The beam proceeded to the ANL gas stopper in the beam-stopping area [65] via a momentum-compression beam line, where it was degraded with aluminum degraders of total thickness 2759 μm before passing through an aluminum wedge of center thickness 1016 μm, at 4.1 mrad and entering the gas stopper at an energy less than 1 MeV/u. Once in the gas stopper, ions were stopped by impacts with high-purity helium gas at about 52 torr and a temperature of -7° C. During these collisions, the highly charged ions recombined down to the singly charged +1 state. The ions were transported through the gas cell by a combination of RF and DC fields and gas flow. They were then extracted into an RFQ ion guide

and separated by a magnetic dipole mass separator with a resolving power of approximately 1500.

The activity of the beam after the dipole mass separator was measured with an insertable Si detector, which found the highest activity at a charge to mass ratio of $A/Q = 43$, indicating that the majority of the ^{27}P was being extracted in the form of singly charged phosphorus oxide, $^{27}P^{16}O^{+}$, though there were trace amounts ($\sim$1%) of $[^{27}P^{16}O2]^{+}$ detected as well. This is likely due to the fact that phosphorus reacts readily with oxygen, which is one of a small number of known contaminant gasses in the helium gas cell. The $^{27}P^{16}O^{+}$ ions were delivered from the ANL gas stopper to LEBIT.

The time-of-flight ion cyclotron resonance technique [8], described in Section 2.4, was used to determine the cyclotron frequency – and therefore mass via Equation 2.1 – of the $^{27}P^{16}O^{+}$ which remained in the trap. A 50-, 100-, 150-, or 200-ms quadrupolar RF excitation was used. In order to determine just the presence of the $^{27}P^{16}O^{+}$ a continuous excitation was used and fitted to a theoretical line shape[1]. The center of this fit was used to determine an initial cyclotron frequency and mass, which was checked against all chemically possible molecules composed of stable or long-lived atoms. It was determined that no potential contaminants were within 3 σ of the measured resonance, and therefore the observed resonance must be $^{27}P^{16}O^{+}$.

Once identified, the excitation was switched from continuous to the pulsed Ramsey resonance technique [30] which improved precision by a factor of $\sim$4. A sample 250 ms Ramsey resonance of $^{27}P^{16}O^{+}$ can be found in Figure 4.3; a sample continuous excitation resonance can be seen in Figure 2.4. Because the half-life of ^{27}P is 260 ms–just under the 300 ms average human blink of an eye–excitation times greater than 250 ms were never attempted, as substantial count rate losses occur due to ion decay in the trap. In between each $^{27}P^{16}O^{+}$

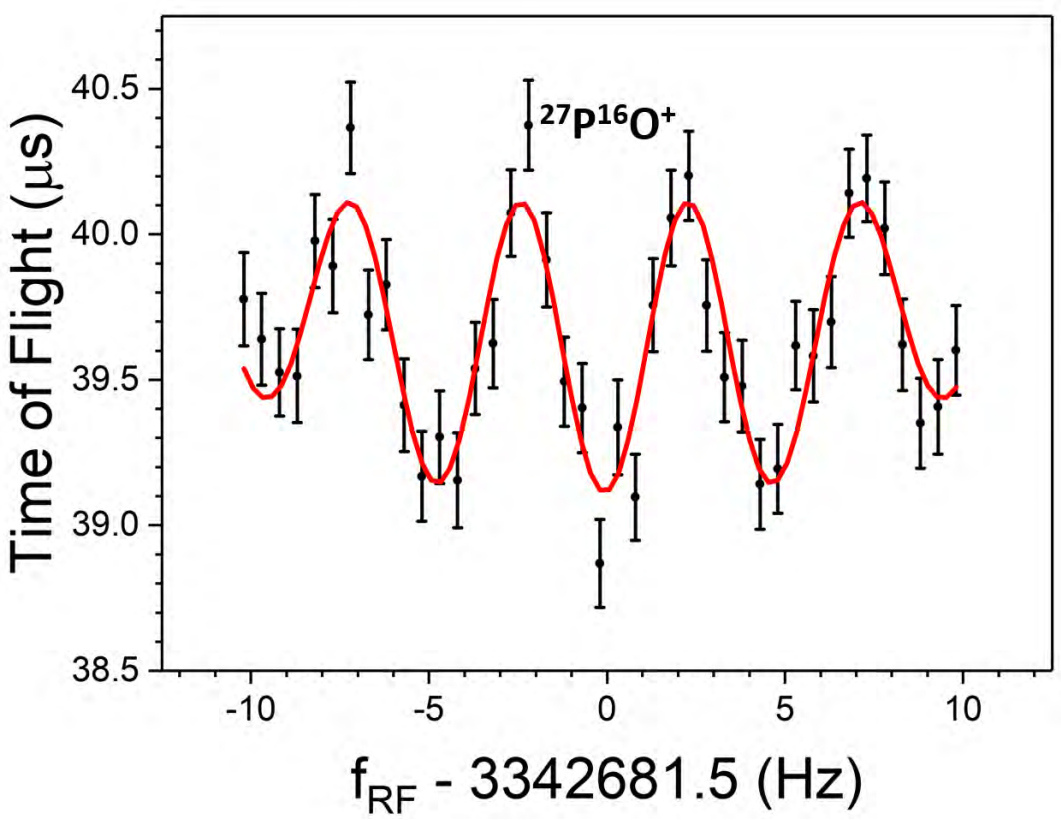

Figure 4.3: A sample $^{27}P^{16}O^{+}$ time-of-flight ion cyclotron Ramsey resonance measurement. The central dip in the interference pattern corresponds to the resonant cyclotron frequency. The red curve is a fit to the theoretical profile [30].

cyclotron frequency measurement, a reference ion measurement was performed in order to determine the exact magnetic field. In this experiment, the reference used was $HCNO^{+}$, as an abundance of it was produced in the gas stopper with $A/Q = 43$.

4.4 The Mass of ^{27}P

The mass measurement results are given in terms of the frequency ratio ($R = \frac{f_{ref}^{int}}{f_c}$), where the ion of interest is $^{27}P^{16}O^{+}$ and the reference ion is $HCNO^{+}$. The final reported atomic mass M is found by taking the average of all of the frequency ratios, $\bar{R}$, and using

$$M = \bar{R}[M_{ref} - m_e] + m_e \tag{4.3}$$

where M_{ref} is the atomic mass of the neutral HCNO molecule, and m_e is the electron mass. Electron ionization energy is neglected, as it is on the order of a few eV's, and the dominant

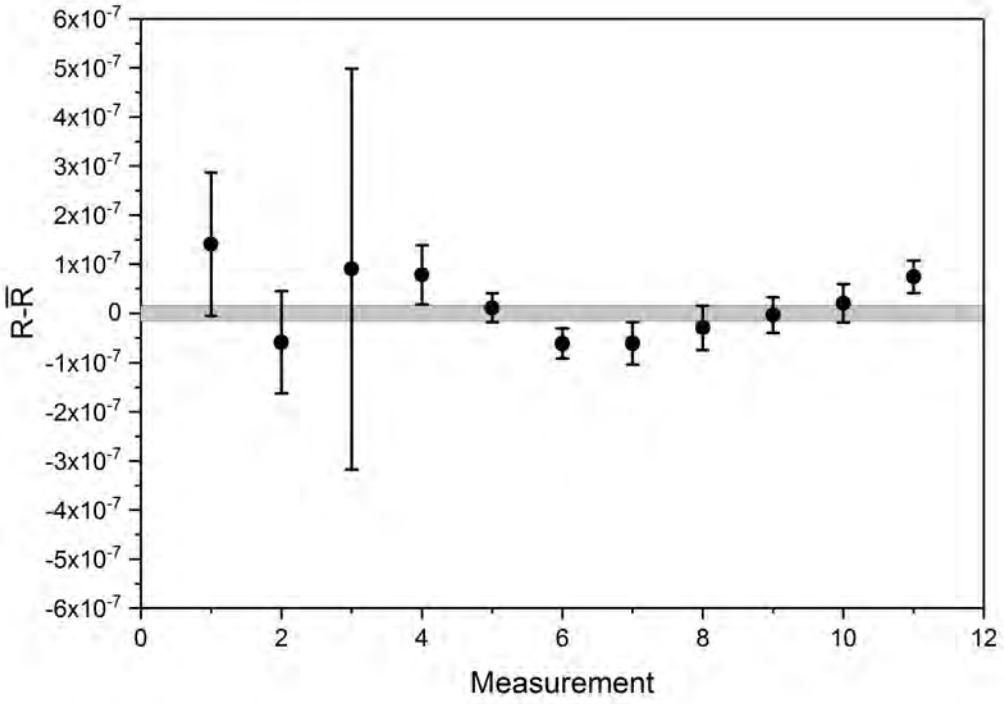

Figure 4.4: Measured cyclotron frequency ratios $R = \frac{f_{ref}^{int}(HCNO^+)}{f_c(^{27}P^{16}O^+)}$ relative to the average value $\bar{R} = 1.000270250(16)$. The gray bar represents $\pm 1\sigma$ uncertainty in $\bar{R}$ and has been scaled by the Birge Ratio of 1.23 [5].

uncertainties are two orders of magnitude greater than this.

Eleven measurements of $^{27}P^{16}O^+$ were performed over the course of approximately 15 hours. These resulted in weighted average of $\bar{R} = 1.000270250(16)$, as can be seen in Figure 4.4. The distribution of individual values of R were statistically above average, resulting in a Birge ratio [5] of 1.23(14). Because it was greater than one, the uncertainty was scaled by this Birge Ratio. This correlates to a ^{27}P mass excess of -670.7± 0.6 keV

Systematic shifts in $\bar{R}$ have been found to scale linearly with mass difference between the calibrant and target ions. Systematic shifts include trap misalignment with magnetic field, magnetic field inhomogeneities, harmonic electric potential distortions, and nonharmonic trapping potential imperfections [8]. These mass dependent shifts have been thoroughly

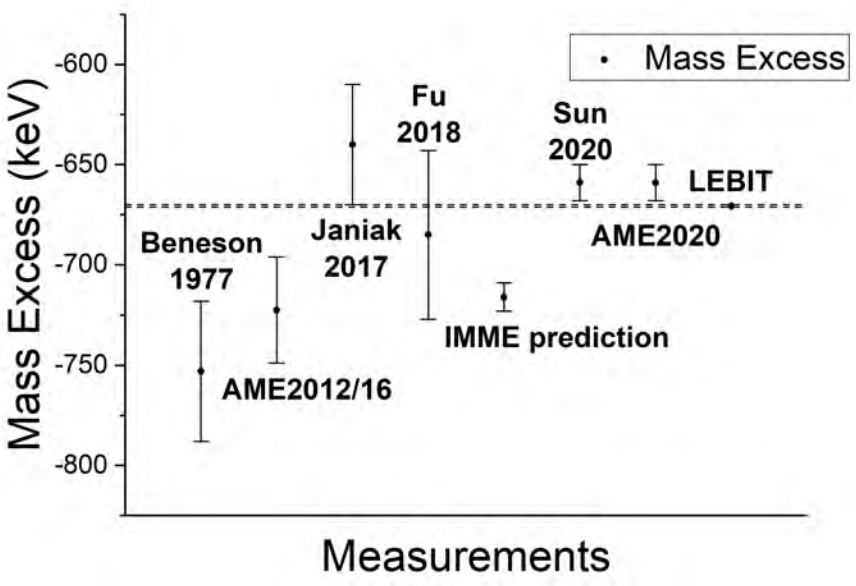

Figure 4.5: Past measurements and predictions of ^{27}P's mass compared to the LEBIT result (dotted line). [66]

investigated at LEBIT and found to be $\Delta R \sim 2 \times 10^{-10}/u$ [25] which is negligible in comparison to statistical uncertainties.

Further systematic effects include nonlinear shifts in the magnetic field, relativistic effects on f_c, and ion-ion interactions in the Penning trap. Nonlinear magnetic field fluctuations have been shown to have an effect less than 1×10^{-9} over one hour [52], which was the approximate time required for a single $^{27}P^{16}O^+$ measurement. Relativistic effects were negligible because of the large ion masses, and the fact that the IoI and reference both had the same A/Q [52]. Isobaric contaminant ions were identified and cleaned as described in Section 2.5 in order to maximize signal strength. For both $^{27}P^{16}O^+$ and $HCNO^+$, events where enough ions were present in the trap to potentially cause a systematic frequency shift were excluded by analyzing only events in which five or fewer ions were detected.

Due largely to its astrophysical importance, ^{27}P's mass has been measured several times.

The LEBIT measurement is shown in comparison to past measurements and the AME2020 evaluation in Figure 4.5.

4.5 Analysis

4.5.1 IMME Prediction

The IMME predicted a ^{27}P mass excess of -716 ± 7 keV [58] (orange band in Figure 4.6), but the LEBIT mass measurement found an excess of -670.7 ± 0.6 keV. This difference exceeds 6σ, indicating an only two in a *billion* chance that this difference is purely from statistical fluctuations. Even including the AME2020 recommended value for ^{27}P as a fit parameter when determining the coefficients for the first order IMME doesn't resolve the issue. Including the AME2020 mass causes the IMME to predict a ^{27}P mass excess of -685 ± 7 keV (blue band in Figure 4.6). This is still greater than 2σ from the LEBIT result. This result implies a substantial value for a cubic term in the IMME. This term's coefficient, d, is expected to be less than 1 keV [16], however, the LEBIT result requires a substantial d-coefficient of 9 keV (green band in Figure 4.6). Other masses have yielded even larger deviations from expected cubic coefficients, the $A = 53$, $T = \frac{3}{2}$ quartet, for instance, requires a d-coefficient of 39 keV [74]. It is clear to see from Figure 4.6 that only including the AME2020 mass and a cubic d-coefficient causes the IMME to yield a reasonable prediction of ^{27}P's mass. As including a cubic term in a fit with four points guarantees a line whose center passes through each point, this is not good news for IMME's predictive capacity. This should be a cautionary tale for those in astrophysics who rely on the IMME for masses of unmeasured or poorly measured isotopes.

4.5.2 Astrophysical Implications

The LEBIT ^{27}P mass of -670.7$\pm$ 0.6 keV was used to calculate the photodisintegration rate $^{27}\mathrm{P}(\gamma, p)^{26}\mathrm{Si}$, which is exponentially dependent on Q-value. As can be seen in Figure 4.7,

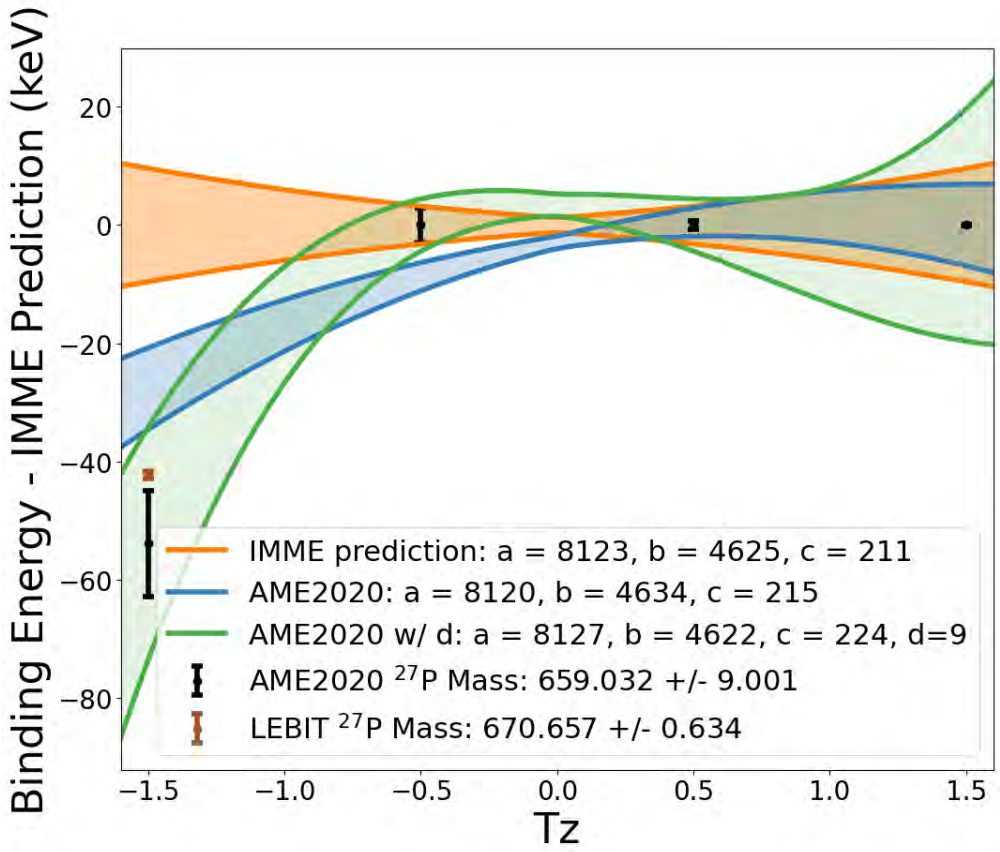

Figure 4.6: Isobaric Multiplet Mass Equation prediction of the binding energy of the $A = 27$, $T = 3/2$ quartet. IMME's form is $BE = a + bT_z + cT_z^2(+dT_z^3)$. A d-coefficient is required for a good fit (green).

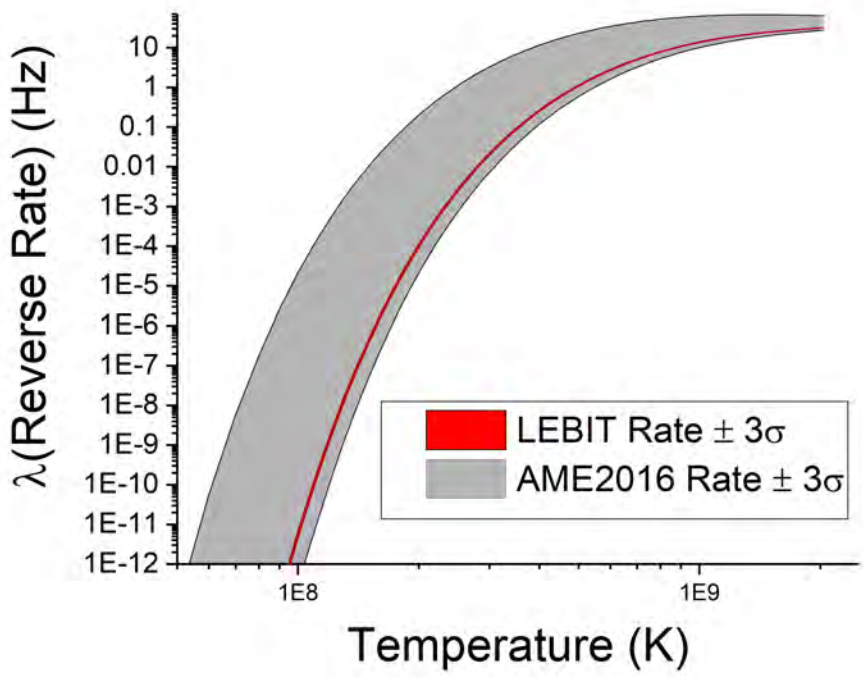

Figure 4.7: Reverse proton capture rate of ^{26}Si varied by uncertainty in the mass of ^{27}P. AME2016 is used for comparison in order to more readily compare to Schatz and Ong's sensitivity study [58]

the LEBIT-based result has a drastically reduced uncertainty as compared to that based on AME2016.

Even though this critical rate was much better determined, MESA (Modules for Experiments in Stellar Astrophysics) simulations using the techniques laid out by Z. Meisel in [39] yielded light curves not substantively different than using the AME2016 ^{27}P mass value. In order to determine if the mass of ^{27}P could have an impact on the light curve of any XRB, the accretion rate of the simulated XRB system was decreased compared to the GS 1826-24 clock burster typically used in simulations (decreased from 2.98×10^{-9} to 1.23×10^{-9} msol/yr). This increases the burst temperature and helium fraction upon ignition, causing more pronounced competition between the (p, γ) and (α, p) pathways. The increased path competitiveness maximizes the change in simulated light curve due to the LEBIT ^{27}P mass

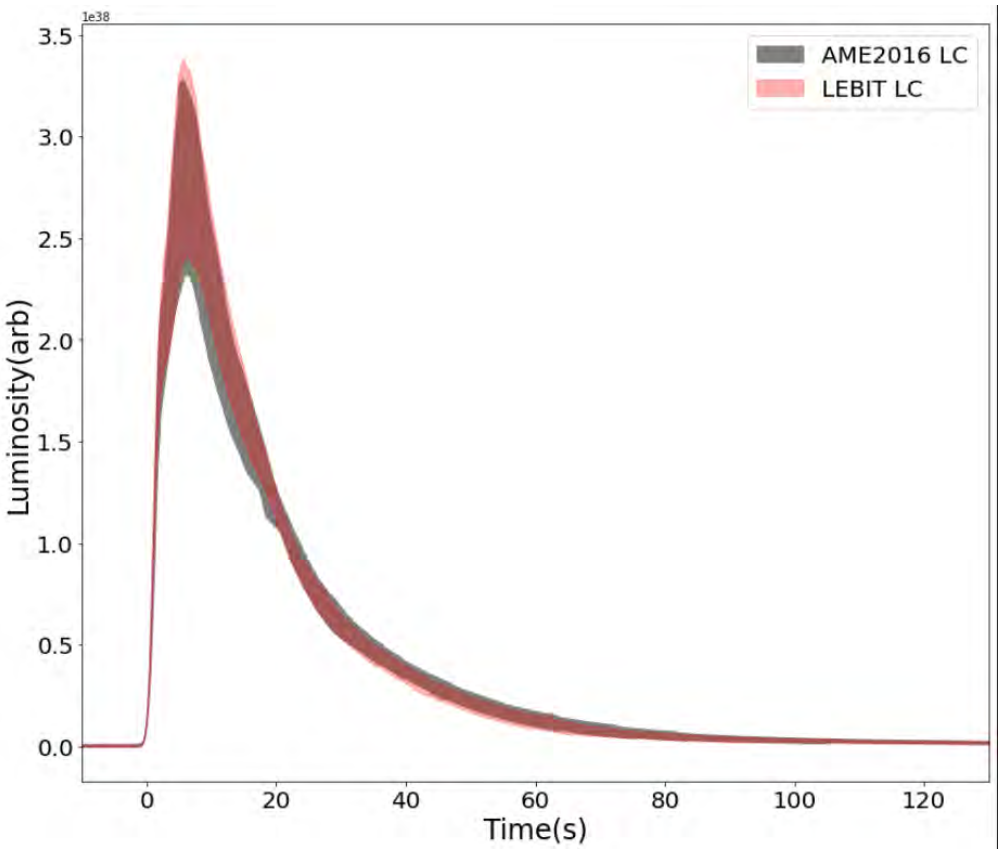

Figure 4.8: MESA multizone XRB light curve generated using the mass of ^{27}P from LEBIT (red) and AME2016, each varied $\pm 3\sigma$. The burster is "GS 1826-24"-like, with accretion rate decreased from 2.98×10^{-9} to 1.23×10^{-9} msol/yr in order to enhance ^{27}P's impact.

measurement, or any variation in the ^{27}P mass. Even in this situation the mass of ^{27}P had nowhere near the impact on the XRB light curve predicted by the single-zone sensitivity study [58], which can be seen in Figure 4.8.

The cause of this result likely lies in the difference between the simple single-zone model result used in [58] compared to the complexity of the multi-zone MESA simulation. One can see in Figure 4.2 that the predicted light curve difference lies primarily in the sharp luminosity drop-off at the very end of the light curve. However, Figure 4.8 shows that this drop-off does not exist. Cyburt et al. point out in [12], this non-physical region "is mainly the result of the absence of radiation transport modeling" in single-zone XRB models and that single-zone models run much hotter than multi-zone models. It was theorized that

^{26}Si$(\alpha, p)^{28}$P requires a temperature higher than is reached in real physical systems and multi-zone XRB models in order to actually compete with proton capture.

In order to test this theory, the flow from ^{26}Si$(p, \gamma)^{27}$P and ^{26}Si$(\alpha, p)^{29}$P was calculated for an array of temperature and density environments potentially achievable in an XRB. The rate of ^{26}Si$(\alpha, p)^{29}$P is unmeasured, so 3$\times$ the NonSmoker calculated rate was used. The multiplication factor of 3$\times$ was chosen based on an uncertainty study of reaction rates in proton rich nuclei [48], which found that while usually the true reaction rate is within 2$\times$ the NonSmoker rate, it is in some cases about 3$\times$ the rate. As it was our goal to find the scenario where the (α, p) path was the most competitive, the highest plausible rate was chosen. Finally, to this contour plot was added the path of temperatures and densities in the XRB in the case of a single-zone model of the clock-burster, as was used in [58], and the peak temperature achieved in a MESA simulated train of 39 XRBs using LEBIT's ^{27}P mass value. The results of this simulation are available in Figure 4.9.

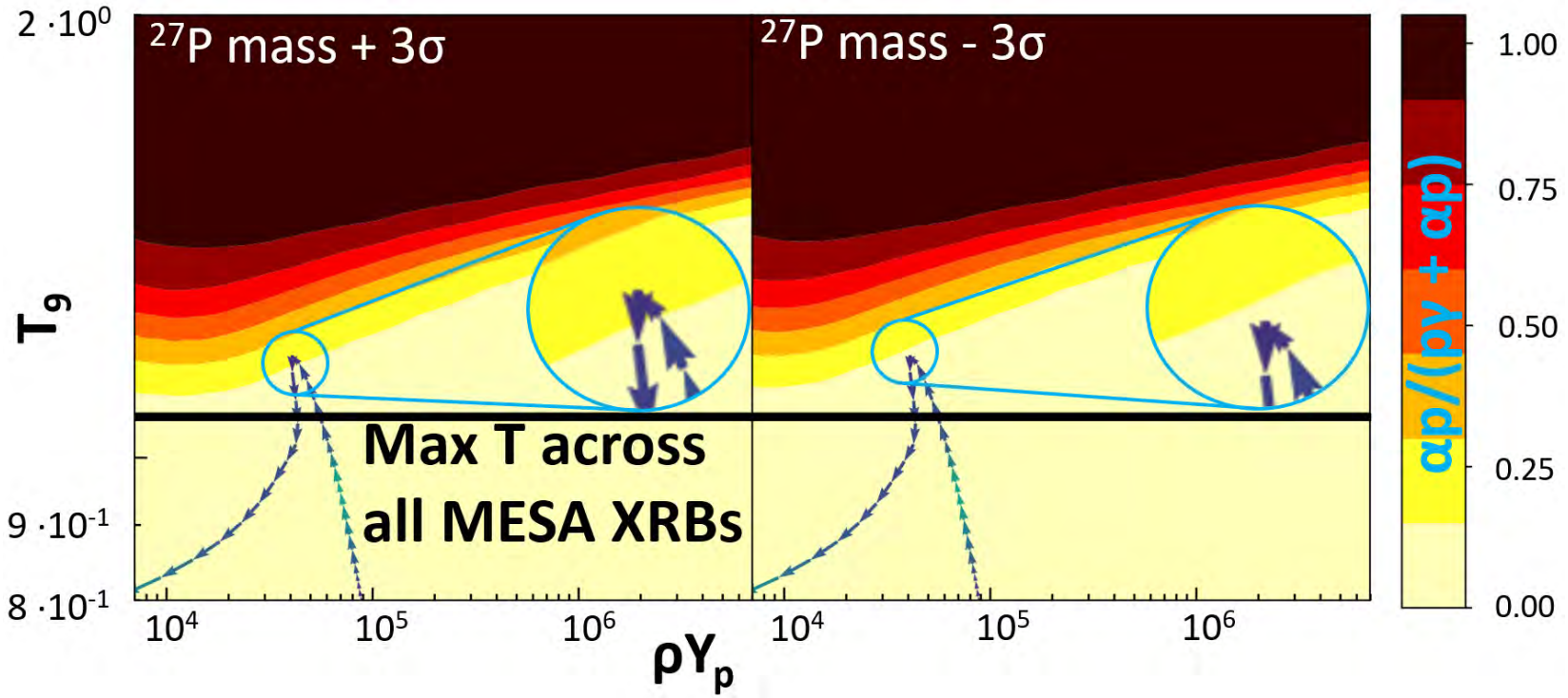

Figure 4.9: Contour plots of the fraction of escape from the ^{26}Si waiting point via alpha capture—$(\alpha, p)/((p, \gamma)+(\alpha, p))$—during a type-I XRB. Contours generated using a ^{27}P mass value of AME2016 $\pm$ 3σ (left: $+3\sigma$, right : -3σ). T_9 is the temperature in GK, ρY_p is the proton density. AME2016 used to demonstrate why sensitivity study [58] predicted the mass of ^{27}P to impact the *rp* process path.
Arrows show the temperature-density profile of the single-zone model over the course of an XRB and are identical in each plot. The horizontal line shows the maximum temperature reached in any multi-zone MESA XRB simulation. Credit and thank you to Wei Jia Ong for producing this plot.

In conclusion, a high-precision mass measurement of ^{27}P has been performed, improving precision by greater than an order of magnitude. Both single-zone type-I x-ray burst models and the isobaric multiplet mass equation have been shown to not reproduce physical observations.

Chapter 5

Implementation of PI-ICR at LEBIT

An overview of the systematic studies and experimental results from PI-ICR will be discussed in this chapter. The details on hardware set up and software created to perform these studies are included in Appendices A, B, and C. While the details of the hardware and software are not necessary for understanding this chapter, the basics will be briefly summarized below. Also, Section 2.6 contains several important concepts which should be understood before delving into this chapter.

The primary hardware change for implementing PI-ICR was the installation of the Roendek-Handels GmbH position sensitive MCP (PS-MCP) detector system. When struck by an ion, the PS-MCP generates an electron shower which drifts to a pair delay-line anodes. The anodes produce a set of four distinct nanosecond precision timing signals. The order delay between these signals uniquely correspond to the x-y position at which the PS-MCP was struck. These signals are amplified, filtered, and digitized by a series of devices before being acquired and analysed by LEBIT custom made software.

A series of codes were developed by LEBIT students and collaborators to control the laboratory equipment in order to automate the acquisition of PI-ICR data, interpret timing signals into positions, filter and cluster position data to minimize noise, and analyse processed position data into mass measurements.

5.1 Studies of Systematics

PI-ICR has many systematic uncertainties which have been thoroughly explored at LEBIT. This is not an exhaustive list of all systematic errors in PI-ICR, nor nearly all which have been investigated during my time at LEBIT.

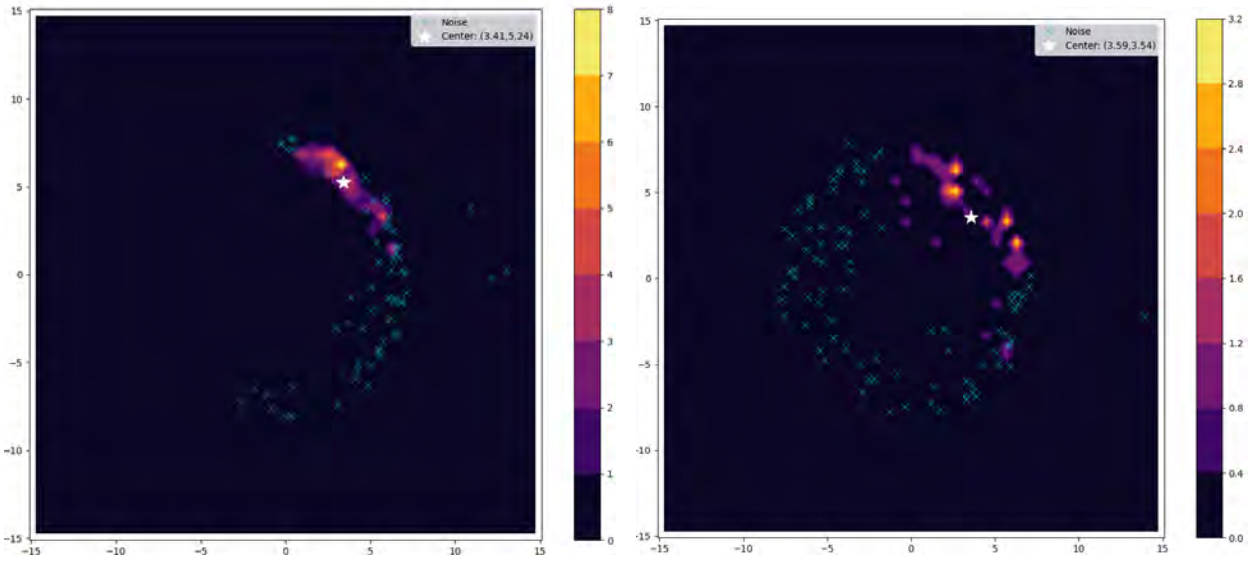

Figure 5.1: A PI-ICR beam spot with a tail after only 10 ms of phase accumulation due to poor trap tuning (left). The same beam spot but with 100 ms of phase accumulation shows almost complete loss of any distinguishable spot (right).

5.1.1 Trap Tuning and Beam Spot Smearing

One of the most common sources of uncertainty in PI-ICR come from "smearing" of the beam spot. The ions that are imaged in this spot have been appropriately excited and converted, but instead of showing up in a tight beam spot, they form a tail. This makes it difficult to determine the location of the beam spot, as the tails are very difficult to filter or cluster in a consistent manner without introducing some systematic phase shift. The tails get worse with more phase accumulation time. Figure 5.1 shows that they can be bad enough that the beam spot becomes nearly impossible to confidently distinguish.

After extensive investigations, the cause of this smearing was determined to be trap tuning, defined by the correction ring and correction tube (see Section 3.2.3) voltages applied in the Penning trap in order to approximate a perfect trapping potential which would be formed if the trap electrodes did not have entrance and exit holes, and were infinite hyperbolas. The tails are formed when ions, which have an approximately Gaussian distribution in

axial position when they are enter the trap, have substantial axial oscillations. Even perfect capture in the trap yields some ions which are oscillating axially, only ions at the center of the Gaussian position distribution can be free of axial oscillations. These ions spend time further from trap center, where the trapping field imperfections are more severe. This creates a small systematic shift in the ion's magnetron and reduced cyclotron frequency, causing the tails to form.

In addition to forming tails, bad trap tuning has been found to cause systematic shifts to actual measured masses. Figure 5.2 shows the scale of these shifts for a variety of correction ring-correction tube pairs. While these measurements were used to attempt to tune the trap, no technique using PI-ICR is yet as trusted as the methods using TOF-ICR described by Brodeur et al. in [9].

5.1.2 Power Supply Noise

When PI-ICR was first being implemented, home-built power supplies which generated their high voltage from S5D140 American Power Design 140 V DC/DC converters were used to control the trapping potentials. These DC/DC converters have an output ripple of $\sim 0.5\%$ V_{p-p}; for standard trapping potentials, this amounts to fluctuations on the order of 100-200 mV. Mathematica simulations of the ion motion in the trap were run in order to determine the shift on the final phase these fluctuations would produce, the results of which can be seen in Figure 5.3. These $\pm 300^\circ$ shifts caused PI-ICR to be useless until the power supplies controlling Penning trap electrode voltages were replaced with a stable, low noise, high long term stability, 16 channel power supply from Stahl Electronics. The short term fluctuations of the Stahl supply are on the order of 0.13 mV_{rms}, yielding a phase uncertainty of $\sim 0.4^\circ/100$ ms phase accumulation time.

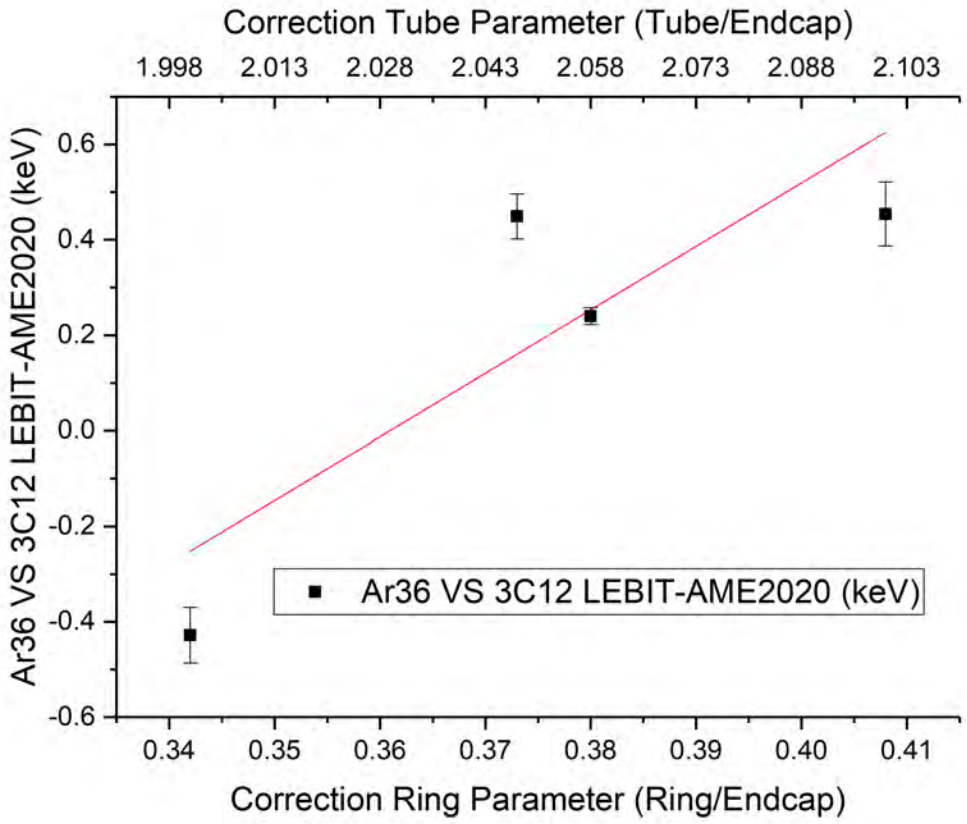

Figure 5.2: Mass measurements of ^{36}Ar with a calibrant of $^{12}C_3$ for a variety of correction ring correction tube pairs.

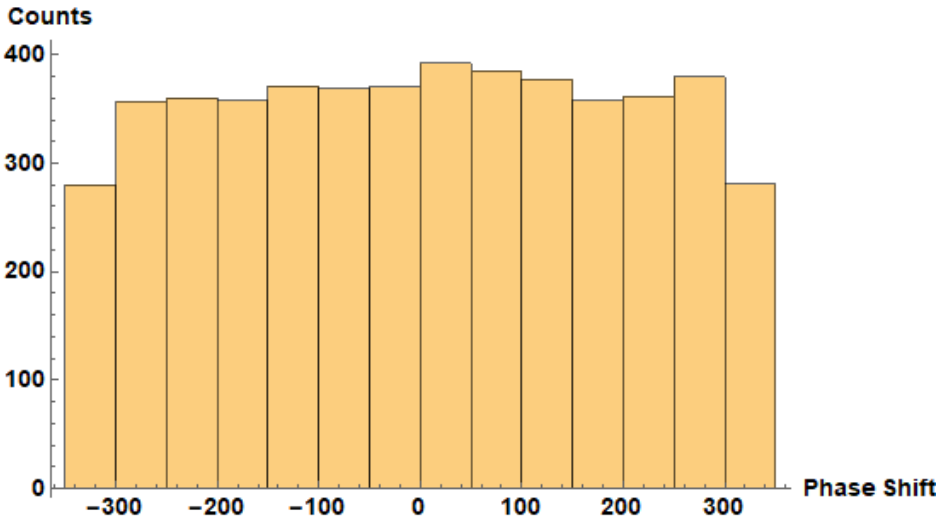

Figure 5.3: Histogram showing the distribution of final phase values for 100 ms of phase accumulation time for 5000 simulated ions with 125 mV fluctuations in trapping potential. Ions are consistently shifted by up to ±300°

5.1.3 Bore Tube Adjustments

The bore tube within the 9.4 T magnet contains the Penning trap, and can be translated and angled in very small increments in order to ensure that the trap is precisely centered at the center of the magnetic field, and that the trap and subsequent ejection optics are parallel to the magnetic field. Simulations using SIMION ion trajectory simulation software was used to find the impact of bore tube shifts, a sample of the results can be seen in Figure 5.4.

These simulations show that the bore tube shifts cause:

- shifts to the projection of the trap center with respect to PS-MCP center
- shifts to trap center measured for on-center ions vs measured by finding the center of a projected ellipse
- the ellipticity of the projection
- asymmetrical distributions of ions within the elliptical projection

All of these shifts can be neglected if trap center is found by fitting the projected ellipse, as described in Section 2.6.1, and using a small angle for the difference between a start phase and a final phase. Attempts to find a better bore tube position using these simulations as a guide have just commenced at LEBIT. Assuming their success, in the future, any angle between start and final phases can be trusted, and trap center can be found by injection ions on-center, releasing them, and measuring their projection onto the PS-MCP. These improvements will be vital for saving time, and ensuring all measurements are valuable in low rate exotic isotope measurements.

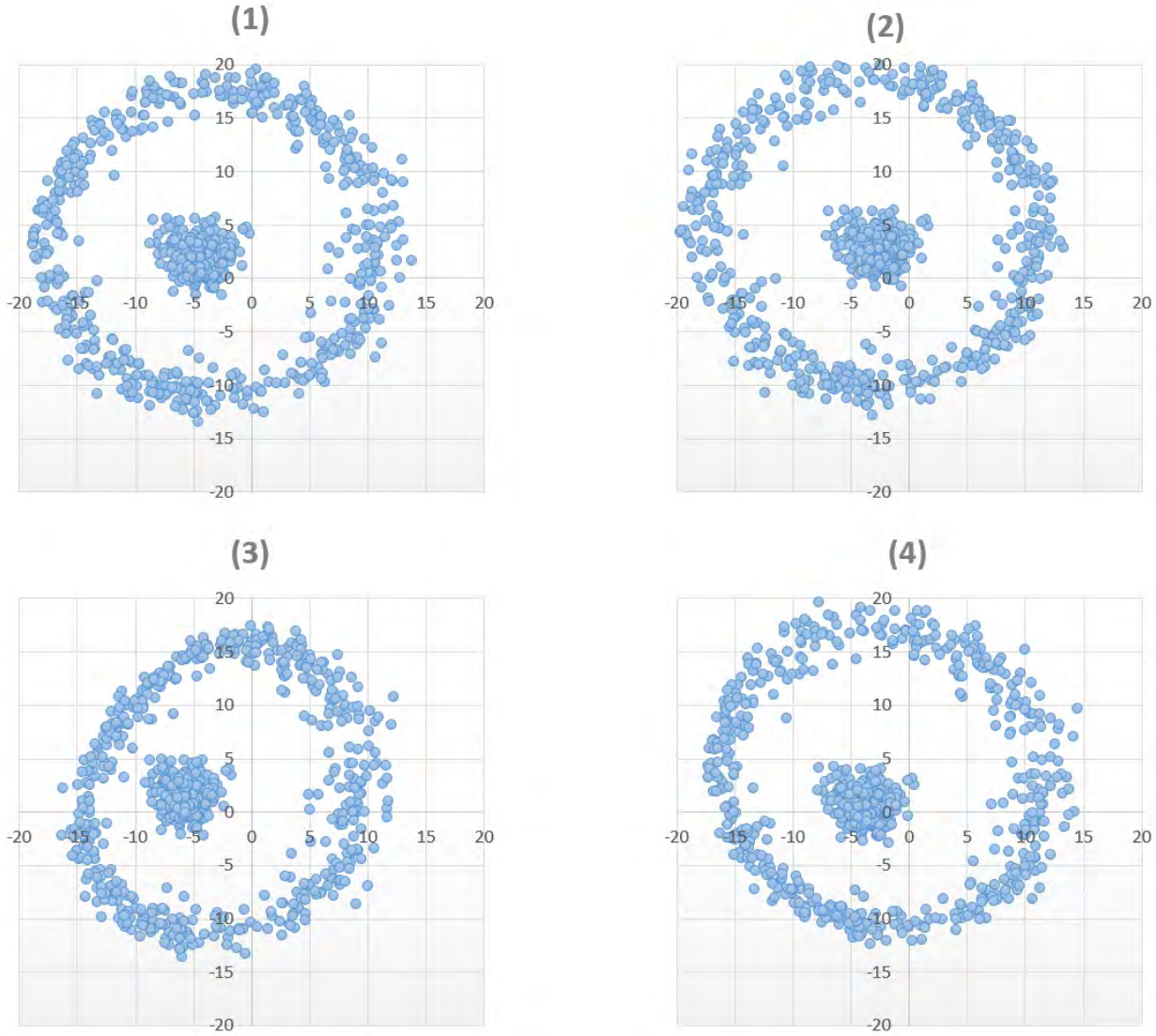

Figure 5.4: Results of SIMION simulations where bore-tube is translated with respect to B-field center and tilted with respect to B-field lines. Ions excited off-center and left on-center before ejection simulated simultaneously. (1) 0.5 mm translation in +Y direction and perfect angular alignment of bore and B-field lines. Shows shift in projection location but little to no distortion. (2) adds $+0.75°$ shift in XY-plane to (1). Shows negligible additional distortion. (3) adds $-0.75°$ shift in XY-plane to (1). Shows substantial shift in center as measured by on-center vs. off-center ions, some elliptical distortion, and asymmetric ion distribution. (4) adds $+0.75°$ shift in XZ plane, perpendicular to the translation, to (1). Shows shift in center as measured by on-center vs. off-center ions, minimal elliptical distortion, and some asymmetry in ion distribution. (4) is very similar to observed data in LEBIT.

5.1.4 Setting The Phase Accumulation Time, t_{acc}

Originally, the phase accumulation time, t_{acc}, was set using a custom timing generator consisting of a National Instruments FPGA card in a PXI chassis. This device is controllable via MM8 timing file (see Appendix B), and produces a set of high/low signals at start-time and with duration set by the user. They are used to control every component in the lab which must switch states with precise timing, such as the ToF gate and buncher ejection described in Sections 3.2.2 and 3.2.3. For t_{acc}, a high signal was sent to first AFGmag for the duration of the excitation time, and after a delay of equal to t_{acc}, another high signal was sent to AFG8 for the duration of the conversion time. These AFGs were working in gated burst mode such that they only output their RF signal to the trap when a high signal was being received. When t_{acc} was systematically varied, however, it was discovered that the frequency measured, and therefore mass, drastically varied, as can be seen in Figure 5.5. The cause of this shifting result is a systematic non-constant jitter in t_{acc} as produced by the FPGA causing the true t_{acc} to be increasingly less than the set t_{acc}. The reason for the large jumps at points 15, 30, and 45 are that the analysis automatically guesses that number of full turns, n, and these were the points when $n+1$ yielded a frequency measurement closer to the MM8 calculated frequency than n.

This error in generated timings is small enough that it had never caused problems in LEBIT before, but for PI-ICR, a difference on the order of 10's of ns can cause significant shifts, like we see here.

The solution was to rely on the timing-generator only to send one start-pulse to both AFGmag and AFG8, which were each placed in triggered burst mode instead of gated burst. When each arbitrary function generator receives start-pulse, they wait for a specified delay,

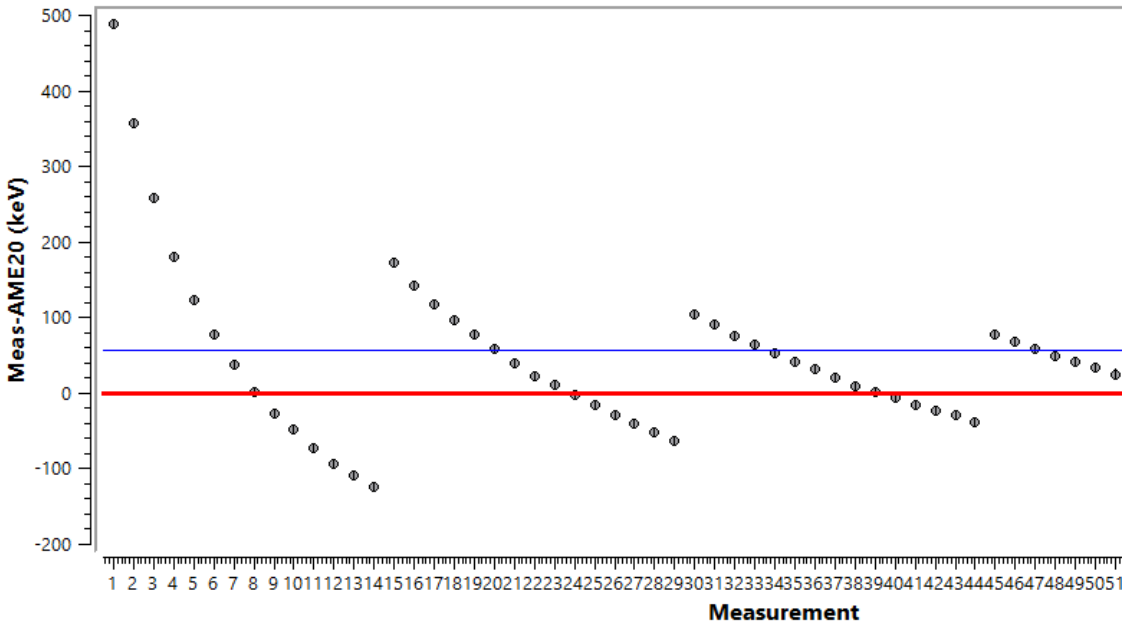

Figure 5.5: A mass measurement of ^{41}K with ^{39}K as a reference. The phase accumulation time t_{acc} was varied from 10 ms to 100 ms in 51 steps.

then execute a specified number of cycles of their RF-signals. The mechanics of calculating and setting these delays and number of bursts is described in Appendix B. The results are that t_{acc} is set by the precise delay in AFG8 and mass measurements do not depend on t_{acc}–aside from their uncertainties, of course.

5.1.5 Buncher Ejection

As mentioned in Section 5.1.1 and 3.2.2, ions ejected from the buncher have an approximately Gaussian distribution of positions and energies. This leads to unavoidable axial oscillations in the trap, leading to smearing as described in Section 5.1.1. While good trap tuning can minimize the tails by minimizing the frequency shifts associated with spending time accumulating phase axially away from trap center, recently efforts have been made to minimize smearing by narrowing the energy and position distribution of ions as they exit the buncher. The work is preliminary but results so far, visible in Figure 5.6, are good. With the bias amplitude of buncher ejection electrodes set to half their usual values, a substantial

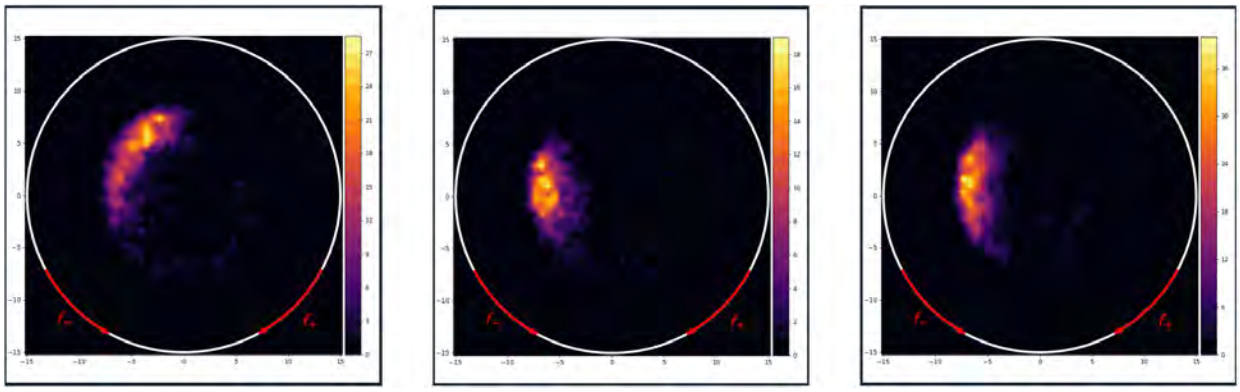

Figure 5.6: Beam spot images with 150 ms of reduced cyclotron phase accumulation. The only difference between the ion preparation for each spot is the buncher ejection potentials are: (left) the usual potentials used at LEBIT for the past ≈10 years, (center) half the usual value, (right) on quarter the usual value.

reduction in smearing is observed. This reduction in smearing was enhanced further, Figure 5.7, when the ion energy was readjusted using the voltage-pulsed drift tube, and the timing of the Penning trap closing was shifted so that the center of the Gaussian axial distribution of ions was centered at trap center at the time of closing. This investigation is still in its early phases; it is likely that systematic variation of buncher ejection settings, followed by Penning trap injection optimization, will yield further improvements to the quality of the beam-spot.

5.1.6 Ion Extraction from Trap to MCP

Ejection settings for TOF-ICR and PI-ICR cannot be the same for either methodology to work well. TOF-ICR requires a slow ejection from the magnetic field. This allows the changing magnetic field to exert the maximum force on the orbiting ions, enhancing the ToF effect as discussed in Section 2.4. PI-ICR, on the other hand, works best if the ions leave the magnetic field as quickly as possible, minimizing the amount of additional phase accumulation the ions gain outside of the Penning trap. In addition, ejection optics can introduce distortions to the projection of the ions in the trap onto the PS-MCP. Several changes were made in order to update the ejection optics to accommodate for PI-ICR.

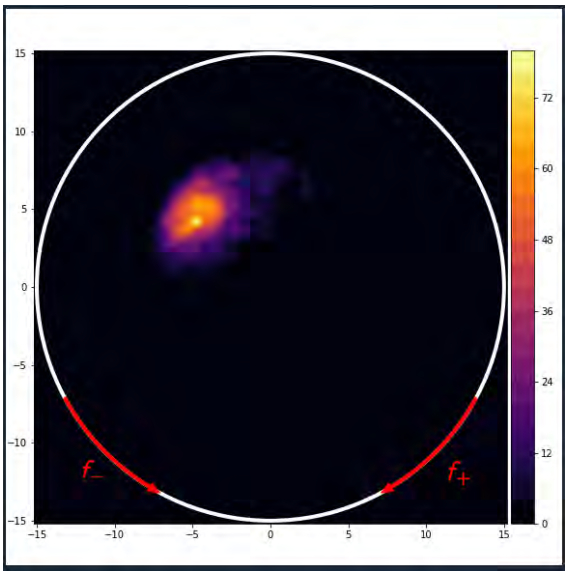

Figure 5.7: Beam spot with 200 ms of reduced cyclotron phase accumulation using half the usual buncher ejection potentials, post optimization of ion energy with pulsed drift tube 1 and trap injection timing (see Section 3.2.2 for more info)

To increase the rate at which the ions exit the magnetic field. The power supplies which bias the first two drift tubes immediately after the trap were replaced to increase their range from ±100 V to ±400 V. Voltages much greater than this were found to occasionally cause sparking between the Penning trap and drift tube 1, risking damage to the trap and the PS-MCP.

The Daly collector and MCP (non-position sensitive) are placed perpendicular to the path of the ions, while the PS-MCP sits in-line with the ions, just past the Daly collector and MCP. These components break the cylindrical symmetry of the rest of the ejection optics and had the potential to interfere with the cylindrical symmetry of the projection, thus, an actuator was installed which can remotely shift the Daly collector and MCP to below the ejection beam line, replacing them with a conical drift tube which gradually increases in radius from the radius of the ejection drift tubes to the radius of the PS-MCP, maintaining cylindrical symmetry of the ejection optics, and allowing ions to be able to impinge on the full surface of the PS-MCP.

Ejection Element	TOF-ICR Bias (V)	PI-ICR Bias (V)
DT1	-27	-200
DT2	-30	-290
DT3	-290	-1100
DT4	-700	-2000
DT5	-2000	-2250
DT6	-4600	-2450
DT7	-2100	-3400
DT8	-2900	-2600
DT9 (conic)	N/A	-2350
PS-MCP	N/A	-2350
Daly Collector	4500	N/A
MCP	2150	N/A

Table 5.1: Bias voltage of each ejection optical element after the Penning Trap for both TOF-ICR and PI-ICR. "DT" stands for "drift tube".

Finally, the ejection optics were programmatically optimized using an code written originally by Erich Leistenschneider, improved by this author, and converted from ROOT to Python and further improved by Scott Campbell. The script systematically varies user defined potentials while making a measurement, and attempts to maximize an optimization parameter. In this case, the potentials were ejection drift tubes 1-9, the measurement was a PI-ICR ellipse projection (see Section 2.6.1 and Appendix B), and the optimization parameter p_{opt} was:

$$p_{opt} \propto \frac{NR^{\frac{3}{2}}}{\bar{e}^2(|a-b|+1)^2(1+x_{center}^2+y_{center}^2)^{\frac{1}{3}}} \tag{5.1}$$

where N is the number of detected ions, R is the mean radius of the ellipse, and $\bar{e}$ is the mean of the residuals of the ellipse fit. a and b are the major and minor axis of the ellipse fit, respectively, and "1" is added to them so that p_{opt} does not go to infinity at very circular fits. x_{center} and y_{center} are the center of the ellipse fit, and similarly have 1 added to them to avoid a singularity at a well centered ellipse fit. Table 5.1 shows the results of the optimization compared to the ejection settings used for TOF-ICR.

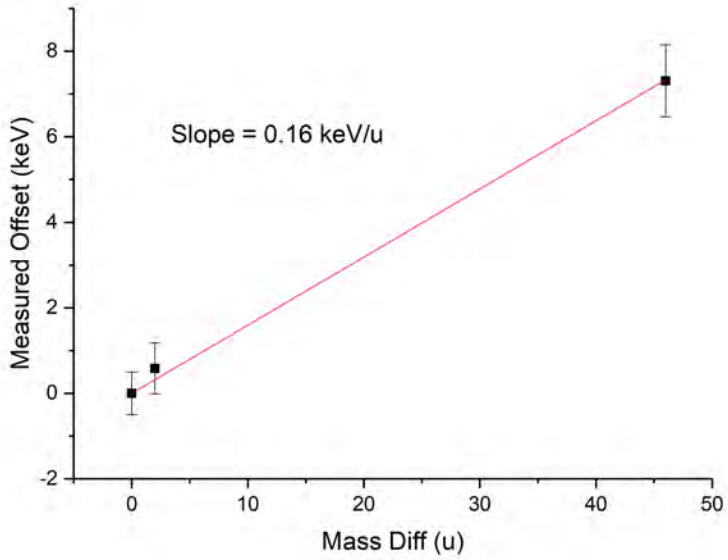

Figure 5.8: Mass shift measured for a difference of 0, 2, and 46 u. Uncertainty in measured offset increased to account for uncertainty in trap tuning.

5.1.7 Mass Dependent Shifts

When making a precision mass measurement using any method, it is best to use a reference mass of an ion that is an isobar of the ion of interest. This causes a number of mass dependent systematic shifts, such as those due to electric-field imperfections, magnetic-field inhomogeneities, or relativistic shifts to reduce to a level well below 10^{-10} [24]. When an isobaric calibrant is not available, it is important to know the scale of the shift in measured mass depending on the mass difference between the ion of interest and reference ion.

This exact value is still under investigation, but initial results are shown in Figure 5.8. Using a variety of measurements of ^{36}Ar vs $^{12}C_3$, ^{39}K vs ^{41}K, and ^{39}K vs ^{85}Rb, the approximate mass shift is calculated to be ~ 0.16 keV/u.

5.1.8 Off-Center Injection

One common issue associated with PI-ICR is shifts associated with imperfect on-center injection into the Penning trap. This issue is discussed extensively in Section 5.6.3 of Rodney

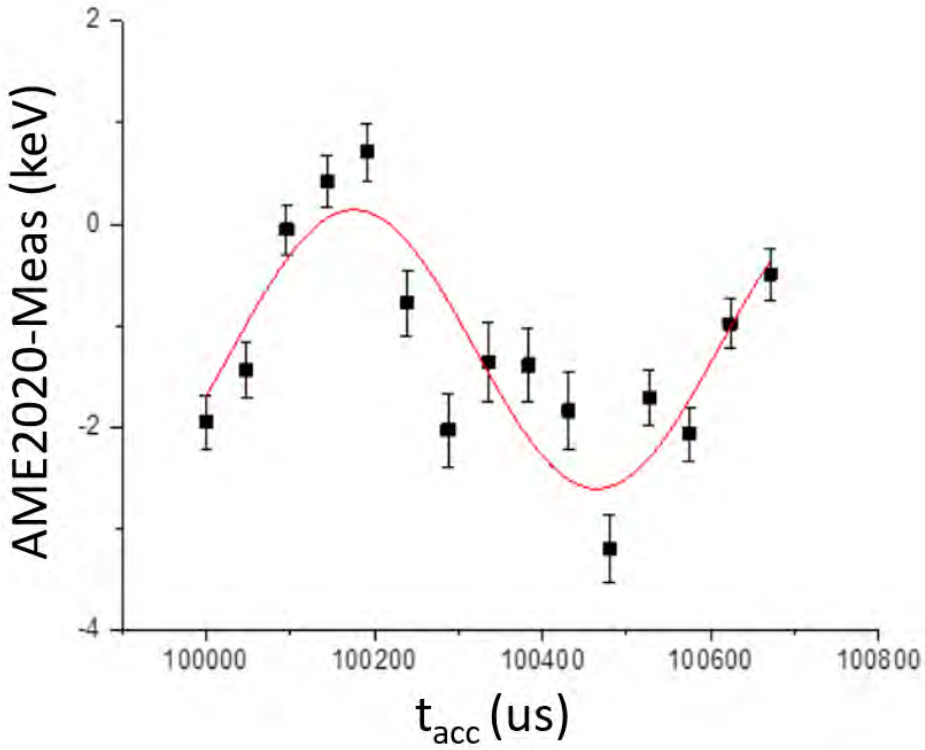

Figure 5.9: Mass measurements made with intentional off-center injection into the penning trap. Measurements were made over a series of 15 accumulation times spanning 700 us, just over one reduced cyclotron period $T_- = 535$ us.

Orford's Thesis [44]. Briefly, it can be described as an effect which occurs due to the fact that ions injected off-center having initial magnetron motion. This motion does not go away when the ions are excited outward with a dipole pulse at f_+, and result is a constant offset in the measured final phase which varies sinusoidally at a frequency equal to the magnetron frequency, f_-. Due to LEBIT's Lorentz steerers [50] providing precision control of ion injection, this has never been an issue. In order to validate the effect, however, ions were intentionally injected off-center before PI-ICR was performed repeatedly at a series of phase accumulation times spanning just over one magnetron period. The resulting mass measurements indeed varied sinusoidally at the ion's magnetron frequency, as can be seen in Figure 5.9. Here, $f_- = 1869 \pm 1$ Hz and the frequency the sinusoidal fit to the t_{acc} dependent mass measurements, $f_{mass} = 1733Hz \pm 91$ Hz, consistent within 2σ.

5.2 Rare Isotope Measurements Using PI-ICR

For the first time, PI-ICR was used to make rare isotope mass measurements at the FRIB facility. These measurements demonstrated LEBIT's capabilities to perform precision PI-ICR mass measurements not only of stable ions, but of short lived exotic isotope produced by projectile fragmentation. The two measurements, ^{105}Sn and ^{22}Al will be part of future publications written by other authors. As such, this section will be a brief demonstration of the capabilities PI-ICR provides as MSU enters the FRIB era.

5.2.1 ^{105}Sn

The PI-ICR measurement of ^{105}Sn was made in preparation for a measurement of doubly-magic ^{100}Sn. With identical chemistry, but a much longer half-life of 33 s, ^{105}Sn was a perfect candidate to test the system, from FRIB all the way through LEBIT, and ensure that once FRIB is brought up to a beam power of 10 kW, ^{100}Sn's mass will be successfully measured.

^{105}Sn was delivered by the gas stopper in its doubly charged state, $^{105}Sn^{2+}$, with a mass to charge number ratio of 52.5. A contaminant within 1 mass unit $(^{1}H^{12}C_2{}^{28}Si)^{+}$ at mass to charge number ratio of 53.0 was found and used as a reference ion. A set of three measurements were carried out over the course of only $\sim$2 hours. Each used a reduced cyclotron phase accumulation time of 100 ms. The result of these measurements can be seen in Figure 5.10. The LEBIT mass excess value of -73338.1 ± 0.8 keV is in excellent agreement with the AME2020 recommended value of -73338 ± 4 keV, but is $\sim 5\times$ as precise.

This result shows that using PI-ICR, LEBIT can produce high quality results in short periods of time, and is fully prepared to run important mass measurements like ^{100}Sn.

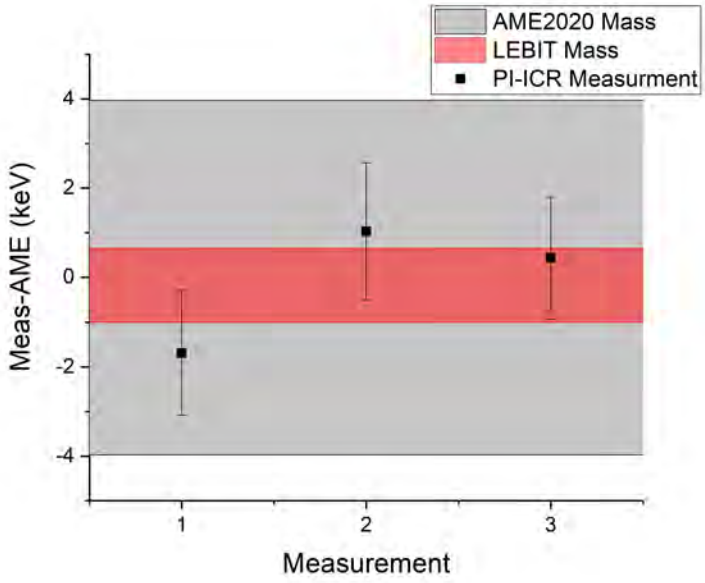

Figure 5.10: The difference between the AME2020 and LEBIT measured mass excess of ^{105}Sn. LEBIT value -73338.1 ± 0.8 keV in red, AME2020 value -73338 ± 4 keV in grey. The error bars of the LEBIT data have been inflated by the Birge ratio [5] value of 1.221 to account for a greater than statistically expected fluctuation in measurements.

5.2.2 ^{22}Al

This thesis presents preliminary results for the world's first mass measurement of ^{22}Al. This short-lived, exotic isotope has a half-life of only 91 ms, and is the first mass measurement of a proton drip line [2] isotope performed at LEBIT. The ^{22}Al was delivered by the gas stopper in a singly charged state, free of isobaric contamination. Due to the lack of available isobars as reference, ^{23}Na delivered by the gas stopper was used as the calibrant. LEBIT had one 12 hour overnight shift to perform this experiment. Due partly to the uncontaminated nature of the delivered beam, it was decided to use this as an opportunity to compare the precision gain of PI-ICR versus TOF-ICR in an on-line setting. The results in Figure 5.11 demonstrate, again, the potential of PI-ICR for precision mass measurements of short lived isotopes. Four measurements were made using TOF-ICR with a 75 ms quadrupolar excitation time, and resulted in a mass excess of 18094.3 ± 1.4 keV. Three PI-ICR meausrements

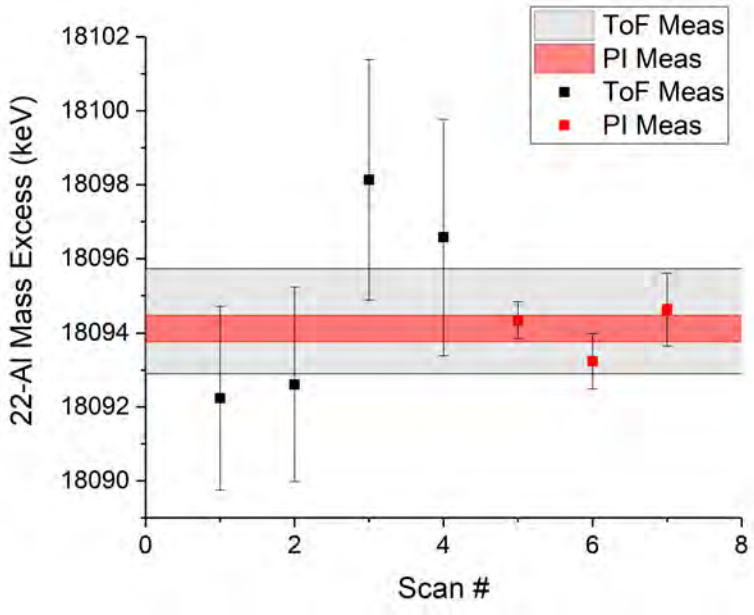

Figure 5.11: PRELIMINARY. World's first measurement of the mass excess of ^{22}Al using both TOF-ICR and PI-ICR.

with reduced cyclotron phase accumulation time of 50 ms resulted in a mass excess and statistical uncertainty of 18094.1 ± 0.4 keV, which is in excellent agreement with the TOF-ICR measurement, but more than three times as precise. As can be seen in Equations 2.11 and 2.15, the statistical uncertainty in the frequency determination both scale as $\delta\omega \propto \frac{1}{T\sqrt{N}}$, where T is the characteristic observation time of the technique, and N is the number of measurements. Therefore, a precision comparison can be made by scaling the ratio of PI to TOF uncertainty by $\frac{t_{excite}}{t_{acc}} = 1.5$ and $\sqrt{\frac{N_{TOF}}{N_{PI}}} = 1.16$. This implies that with LEBIT's current setup a PI-ICR measurement has about 6.5× the statistical precision of a continuous quadrupolar excitation TOF-ICR measurement for the same excitation time.

The preliminary result from all measurements together is 18094.1 ± 0.4 keV

Chapter 6

Conclusion

A mass measurement of ^{27}P was successfully performed at LEBIT, improving the precision by over an order of magnitude. This result drastically constrained the ^{26}Si rp process waiting point equilibrium, $^{26}\mathrm{Si}(p,\gamma)^{27}\mathrm{P}$ – $^{27}\mathrm{P}(\gamma,p)^{26}$, which depends exponentially on the mass of ^{27}P. This new mass was used in a series of MESA supercomputer simulations of type-I x-ray bursts to determine the impact of the change in mass on the light-curve. It was determined that the impact predicted in [58] was not confirmed. An explanation is that the prediction was made using a simple single-zone XRB model which ran hotter than a realistic XRB, resulting in false competition between the (p,γ)-path and (α,p)-path from the ^{26}Si waiting point. In addition, this measurement showed $> 6\sigma$ disagreement with the IMME predicted mass. It serves as a cautionary tale for dependence on the IMME in nuclear astrophysics for predicting unmeasured or poorly measured masses.

The Phase Imaging Ion Cyclotron Resonance technique has been successfully implemented at LEBIT. PI-ICR improves on the precision of any other technique in LEBIT's arsenal, and has already been demonstrated to be a valuable tool in the FRIB era by performing two high precision measurements of exotic isotopes produced at FRIB, ^{105}Sn and, measured for the first time ever, ^{22}Al. PI-ICR has been systematically studied, systematic errors reduced, hardware improved, and more user-friendly software developed. The work performed as a part of this thesis to get it to its current state makes it a staple of LEBIT mass measurements for the foreseeable future.

BIBLIOGRAPHY

[1] Quadrupole excitation of stored ion motion at the true cyclotron frequency. *International Journal of Mass Spectrometry and Ion Processes*, 142:95–116, 1995.

[2] Thomas Baumann and Michael Thoennessen. Proton and neutron drip lines. *AccessScience*, Mar 2020.

[3] D. Bazin, J.A. Caggiano, B.M. Sherrill, J. Yurkon, and A. Zeller. The s800 spectrograph. *Nuclear Instruments and Methods in Physics Research Section B: Beam Interactions with Materials and Atoms*, 204:629–633, 2003. 14th International Conference on Electromagnetic Isotope Separators and Techniques Related to their Applications.

[4] Sönke Beck, Brian Kootte, Irene Dedes, Timo Dickel, A. A. Kwiatkowski, Eleni Marina Lykiardopoulou, Wolfgang R. Plaß, Moritz P. Reiter, Corina Andreoiu, Julian Bergmann, Thomas Brunner, Dominique Curien, Jens Dilling, Jerzy Dudek, Eleanor Dunling, Jake Flowerdew, Abdelghafar Gaamouci, Leigh Graham, Gerald Gwinner, Andrew Jacobs, Renee Klawitter, Yang Lan, Erich Leistenschneider, Nikolay Minkov, Victor Monier, Ish Mukul, Stefan F. Paul, Christoph Scheidenberger, Robert I. Thompson, James L. Tracy, Michael Vansteenkiste, Hua-Lei Wang, Michael E. Wieser, Christian Will, and Jie Yang. Mass measurements of neutron-deficient yb isotopes and nuclear structure at the extreme proton-rich side of the $n = 82$ shell. *Phys. Rev. Lett.*, 127:112501, Sep 2021.

[5] Raymond T. Birge. The calculation of errors by the method of least squares. *Phys. Rev.*, 40:207–227, Apr 1932.

[6] Klaus Blaum. High-accuracy mass spectrometry with stored ions. *Physics Reports*, 425(1):1–78, 2006.

[7] G. Bollen, S. Becker, H. J. Kluge, M. Koenig, R. B. Moore, T. Otto, H. Raimbault-Hartmann, G. Savard, L. Schweikhard, and H. Stolzenberg. Isoltrap: a tandem penning trap system for accurate on-line mass determination of short-lived isotopes. *Nuclear Instruments and Methods in Physics Research Section A, Accelerators, Spectrometers, Detectors and Associated Equipment*, 368(3):675–697, Jan 1996.

[8] G. Bollen, R. B. Moore, G. Savard, and H. Stolzenberg. The accuracy of heavy-ion mass measurements using time of flight-ion cyclotron resonance in a penning trap. *Journal of Applied Physics*, 68(9):4355–4374, 1990.

[9] M. Brodeur, V.L. Ryjkov, T. Brunner, S. Ettenauer, A.T. Gallant, V.V. Simon, M.J. Smith, A. Lapierre, R. Ringle, P. Delheij, M. Good, D. Lunney, and J. Dilling. Verifying the accuracy of the titan penning-trap mass spectrometer. *International Journal of Mass Spectrometry*, 310:20–31, 2012.

[10] Lowell S. Brown and Gerald Gabrielse. Precision spectroscopy of a charged particle in an imperfect penning trap. *Phys. Rev. A*, 25:2423–2425, Apr 1982.

[11] Lowell S. Brown and Gerald Gabrielse. Geonium theory: Physics of a single electron or ion in a penning trap. *Rev. Mod. Phys.*, 58:233–311, Jan 1986.

[12] R. H. Cyburt, A. M. Amthor, A. Heger, E. Johnson, L. Keek, Z. Meisel, H. Schatz, and K. Smith. Dependence of x-ray burst models on nuclear reaction rates. *The Astrophysical Journal*, 830(2):55, oct 2016.

[13] N. R. Daly. Scintillation type mass spectrometer ion detector. *Review of Scientific Instruments*, 31(3):264–267, 1960.

[14] H. G. Dehmelt. Radiofrequency Spectroscopy of Stored Ions I: Storage. *Advances in Atomic and Molecular Physics*, 3:53–72, January 1968.

[15] T. Dickel, W. R. Plaß, A. Becker, U. Czok, H. Geissel, E. Haettner, C. Jesch, W. Kinsel, M. Petrick, C. Scheidenberger, A. Simon, and M. I. Yavor. A high-performance multiple-reflection time-of-flight mass spectrometer and isobar separator for the research with exotic nuclei. *Nuclear Instruments and Methods in Physics Research A*, 777:172–188, March 2015.

[16] J. M. Dong, J. Z. Gu, Y. H. Zhang, W. Zuo, L. J. Wang, Yu. A. Litvinov, and Y. Sun. Beyond wigner's isobaric multiplet mass equation: Effect of charge-symmetry-breaking interaction and coulomb polarization. *Phys. Rev. C*, 99:014319, Jan 2019.

[17] P. Duhamel and M. Vetterli. Fast fourier transforms: A tutorial review and a state of the art. *Signal Processing*, 19(4):259–299, 1990.

[18] S. Eliseev, K. Blaum, M. Block, C. Droese, M. Goncharov, E. Minaya Ramirez, D. A. Nesterenko, Yu. N. Novikov, and L. Schweikhard. Phase-imaging ion-cyclotron-resonance measurements for short-lived nuclides. *Phys. Rev. Lett.*, 110:082501, Feb 2013.

[19] B. Franzke. The Heavy Ion Storage and Cooler Ring Project ESR at GSI. *Nucl. Instrum. Meth.*, B24/25:18–25, 1987.

[20] G. Gabrielse. Why is sideband mass spectrometry possible with ions in a penning trap? *Phys. Rev. Lett.*, 102:172501, Apr 2009.

[21] G. Gabrielse, L. Haarsma, and S.L. Rolston. Open-endcap penning traps for high precision experiments. *International Journal of Mass Spectrometry and Ion Processes*, 88(2):319–332, 1989.

[22] Roentdek Handels GmbH. *MCP Delay Line Detector Manual*. Im Vogelshaag 8, D-65779 Kelkheim-Ruppertshain, Germany, 2022.

[23] J. Grindlay, H. Gursky, H. Schnopper, D. R. Parsignault, J. Heise, A. C. Brinkman, and J. Schrijver. Discovery of intense X-ray bursts from the globular cluster NGC 6624. , 205:L127–L130, May 1976.

[24] K. Gulyuz, J. Ariche, G. Bollen, S. Bustabad, M. Eibach, C. Izzo, S. J. Novario, M. Redshaw, R. Ringle, R. Sandler, S. Schwarz, and A. A. Valverde. Determination of the direct double-β-decay q value of ^{96}Zr and atomic masses of $^{90-92,94,96}$Zr and $^{92,94-98,100}$Mo. *Phys. Rev. C*, 91:055501, May 2015.

[25] K. Gulyuz, J. Ariche, G. Bollen, S. Bustabad, M. Eibach, C. Izzo, S. J. Novario, M. Redshaw, R. Ringle, R. Sandler, S. Schwarz, and A. A. Valverde. Determination of the direct double--decay q value of 96zr and atomic massesof 9092,94,96zr and 92,9498,100mo. *Phys. Rev. C*, 91:055501, May 2015.

[26] Alec Hamaker, Georg Bollen, Martin Eibach, Christopher Izzo, Daniel Puentes, Matthew Redshaw, Ryan Ringle, Rachel Sandler, Stefan Schwarz, and Isaac Yandow. Sipt - an ultrasensitive mass spectrometer for rare isotopes. *Hyperfine Interactions*, 240, Apr. 2019.

[27] W. Heisenberg. Über den bau der atomkerne. i. *Zeitschrift für Physik*, 77, 1 1932.

[28] C. Izzo, G. Bollen, S. Bustabad, M. Eibach, K. Gulyuz, D.J. Morrissey, M. Redshaw, R. Ringle, R. Sandler, S. Schwarz, and A.A. Valverde. A laser ablation source for offline ion production at lebit. *Nuclear Instruments and Methods in Physics Research Section B: Beam Interactions with Materials and Atoms*, 376:60–63, 2016. Proceedings of the XVIIth International Conference on Electromagnetic Isotope Separators and Related Topics (EMIS2015), Grand Rapids, MI, U.S.A., 11-15 May 2015.

[29] V.S. Kolhinen, T. Eronen, J. Hakala, A. Jokinen, S. Kopecky, S. Rinta-Antila, J. Szerypo, and J. Äystö. Penning trap for isobaric mass separation at igisol. *Nuclear Instruments and Methods in Physics Research Section B: Beam Interactions with Materials and Atoms*, 204:502–506, 2003. 14th International Conference on Electromagnetic Isotope Separators and Techniques Related to their Applications.

[30] Martin Kretzschmar. The ramsey method in high-precision mass spectrometry with penning traps: Theoretical foundations. *International Journal of Mass Spectrometry*, 264(2):122–145, 2007.

[31] A. Kwiatkowski, Corina Andreoiu, J. Bale, Thomas Brunner, A. Chaudhuri, Usman Chowdhury, P. Delheij, S. Ettenauer, Dieter Frekers, A. Gallant, A. Grossheim, G. Gwinner, F. Jang, Annika Lennarz, Tasneem Ma, E. Mané, M. Pearson, B. Schultz,

M. Simon, and Jens Dilling. Titan: An ion trap facility for on-line mass measurement experiments. *Hyperfine Interactions*, 225, 10 2013.

[32] A.A. Kwiatkowski, G. Bollen, M. Redshaw, R. Ringle, and S. Schwarz. Isobaric beam purification for high precision penning trap mass spectrometry of radioactive isotope beams with swift. *International Journal of Mass Spectrometry*, 379:9–15, 2015.

[33] E. Leistenschneider, M. P. Reiter, S. Ayet San Andrés, B. Kootte, J. D. Holt, P. Navrátil, C. Babcock, C. Barbieri, B. R. Barquest, J. Bergmann, J. Bollig, T. Brunner, E. Dunling, A. Finlay, H. Geissel, L. Graham, F. Greiner, H. Hergert, C. Hornung, C. Jesch, R. Klawitter, Y. Lan, D. Lascar, K. G. Leach, W. Lippert, J. E. McKay, S. F. Paul, A. Schwenk, D. Short, J. Simonis, V. Somà, R. Steinbrügge, S. R. Stroberg, R. Thompson, M. E. Wieser, C. Will, M. Yavor, C. Andreoiu, T. Dickel, I. Dillmann, G. Gwinner, W. R. Plaß, C. Scheidenberger, A. A. Kwiatkowski, and J. Dilling. Dawning of the $n = 32$ shell closure seen through precision mass measurements of neutron-rich titanium isotopes. *Phys. Rev. Lett.*, 120:062503, Feb 2018.

[34] Walter H. G. Lewin. X-ray bursts. *Space Science Reviews*, 62:223, sep 1993.

[35] K.R. Lund, G. Bollen, D. Lawton, D.J. Morrissey, J. Ottarson, R. Ringle, S. Schwarz, C.S. Sumithrarachchi, A.C.C. Villari, and J. Yurkon. Online tests of the advanced cryogenic gas stopper at nscl. *Nuclear Instruments and Methods in Physics Research Section B: Beam Interactions with Materials and Atoms*, 463:378–381, 2020.

[36] G. Machicoane, D. Cole, J. Ottarson, J. Stetson, and P. Zavodszky. Artemis-b: A room-temperature test electron cyclotron resonance ion source for the national superconducting cyclotron laboratory at michigan state university. *Review of Scientific Instruments*, 77(3):03A322, 2006.

[37] I. Mardor, S. Ayet San Andrés, T. Dickel, D. Amanbayev, S. Beck, J. Bergmann, H. Geissel, L. Gröf, E. Haettner, C. Hornung, N. Kalantar-Nayestanaki, G. Kripko-Koncz, I. Miskun, A. Mollaebrahimi, W. R. Plaß, C. Scheidenberger, H. Weick, Soumya Bagchi, D. L. Balabanski, A. A. Bezbakh, Z. Brencic, O. Charviakova, V. Chudoba, Paul Constantin, M. Dehghan, A. S. Fomichev, L. V. Grigorenko, O. Hall, M. N. Harakeh, J.-P. Hucka, A. Kankainen, O. Kiselev, R. Knöbel, D. A. Kostyleva, S. A. Krupko, N. Kurkova, N. Kuzminchuk, I. Mukha, I. A. Muzalevskii, D. Nichita, C. Nociforo, Z. Patyk, M. Pfützner, S. Pietri, S. Purushothaman, M. P. Reiter, H. Roesch, F. Schirru, P. G. Sharov, A. Spătaru, G. Stanic, A. State, Y. K. Tanaka, M. Vencelj, M. I. Yavor, and J. Zhao. Mass measurements of as, se, and br nuclei, and their implication on the proton-neutron interaction strength toward the $n = z$ line. *Phys. Rev. C*, 103:034319, Mar 2021.

[38] Alan G. Marshall, Christopher L. Hendrickson, and George S. Jackson. Fourier transform ion cyclotron resonance mass spectrometry: A primer. *Mass Spectrometry Reviews*, 17(1):1–35, 1998.

[39] Zach Meisel. Consistent modeling of gs 1826-24 x-ray bursts for multiple accretion rates demonstrates the possibility of constraining rp-process reaction rates. *The Astrophysical Journal*, 860(2):147, jun 2018.

[40] Zach Meisel. Mapping the frontiers of the nuclear mass surface. *Journal of Physics: Conference Series*, 1668:012026, 10 2020.

[41] D.J. Morrissey, B.M. Sherrill, M. Steiner, A. Stolz, and I. Wiedenhoever. Commissioning the a1900 projectile fragment separator. *Nuclear Instruments and Methods in Physics Research Section B: Beam Interactions with Materials and Atoms*, 204:90–96, 2007.

[42] M. Mougeot, D. Atanasov, J. Karthein, R. N. Wolf, P. Ascher, K. Blaum, K. Chrysalidis, G. Hagen, J. D. Holt, W. J. Huang, G. R. Jansen, I. Kulikov, Yu. A. Litvinov, D. Lunney, V. Manea, T. Miyagi, T. Papenbrock, L. Schweikhard, A. Schwenk, T. Steinsberger, S. R. Stroberg, Z. H. Sun, A. Welker, F. Wienholtz, S. G. Wilkins, and K. Zuber. Mass measurements of 99–101in challenge ab initio nuclear theory of the nuclide 100sn. *Nature Physics*, 17, Oct 2021.

[43] D. A. Nesterenko, T. Eronen, Z. Ge, A. Kankainen, and M. Vilen. Study of radial motion phase advance during motion excitations in a penning trap and accuracy of jyfltrap mass spectrometer. *The European Physical Journal A*, 57:302, nov 2021.

[44] R. Orford. *A phase-imaging technique for precision mass measurements of neutron-rich nuclei with the Canadian Penning Trap mass spectrometer*. PhD thesis, Montreal, QC, Canada, 2019.

[45] Radim Hal oy and Jan Flusser. Numerically stable direct least squares fitting of ellipses. 1998.

[46] B. Paczynski. Evolutionary processes in close binary systems. *Annual Review of Astronomy and Astrophysics*, 9(1):183–208, 1971.

[47] Sascha Rau, Fabian Heiße, Florian Köhler-Langes, Sangeetha Sasidharan, Raphael Haas, Dennis Renisch, Christoph E. Düllmann, Wolfgang Quint, Sven Sturm, and Klaus Blaum. Penning trap mass measurements of the deuteron and the hd+ molecular ion. *Nature*, 585(7823):43–47, Sep 2020.

[48] T. Rauscher, N. Nishimura, R. Hirschi, G. Cescutti, A. St. J. Murphy, and A. Heger. Uncertainties in the production of p nuclei in massive stars obtained from Monte Carlo variations. *Monthly Notices of the Royal Astronomical Society*, 463(4):4153–4166, 09 2016.

[49] M. P. Reiter, S. Ayet San Andrés, J. Bergmann, T. Dickel, J. Dilling, A. Jacobs, A. A. Kwiatkowski, W. R. Plaß, C. Scheidenberger, D. Short, C. Will, C. Babcock, E. Dunling,

A. Finlay, C. Hornung, C. Jesch, R. Klawitter, B. Kootte, D. Lascar, E. Leistenschneider, T. Murböck, S. F. Paul, M. Yavor, and Titan Collaboration. Commissioning and performance of TITAN's Multiple-Reflection Time-of-Flight Mass-Spectrometer and isobar separator. *Nuclear Instruments and Methods in Physics Research A*, 1018:165823, December 2021.

[50] R. Ringle, G. Bollen, A. Prinke, J. Savory, P. Schury, S. Schwarz, and T. Sun. A "lorentz" steerer for ion injection into a penning trap. *International Journal of Mass Spectrometry*, 263(1):38–44, 2007.

[51] R. Ringle, G. Bollen, A. Prinke, J. Savory, P. Schury, S. Schwarz, and T. Sun. The lebit 9.4t penning trap mass spectrometer. *Nuclear Instruments and Methods in Physics Research Section A: Accelerators, Spectrometers, Detectors and Associated Equipment*, 604(3):536–547, 2009.

[52] R. Ringle, T. Sun, G. Bollen, D. Davies, M. Facina, J. Huikari, E. Kwan, D. J. Morrissey, A. Prinke, J. Savory, P. Schury, S. Schwarz, and C. S. Sumithrarachchi. High-precision penning trap mass measurements of ^{37,38}Ca and their contributions to conserved vector current and isobaric mass multiplet equation. *Phys. Rev. C*, 75:055503, May 2007.

[53] Ryan Ringle, Stefan Schwarz, and Georg Bollen. Penning trap mass spectrometry of rare isotopes produced via projectile fragmentation at the lebit facility. *International Journal of Mass Spectrometry*, 349:87–93, 2013.

[54] R. Sandler, G. Bollen, J. Dissanayake, M. Eibach, K. Gulyuz, A. Hamaker, C. Izzo, X. Mougeot, D. Puentes, F. G. A. Quarati, M. Redshaw, R. Ringle, and I. Yandow. Direct determination of the ^{138}La β-decay q value using penning trap mass spectrometry. *Phys. Rev. C*, 100:014308, Jul 2019.

[55] R. Sandler, G. Bollen, N. D. Gamage, A. Hamaker, C. Izzo, D. Puentes, M. Redshaw, R. Ringle, and I. Yandow. Investigation of the potential ultralow q-value β-decay candidates ^{89}Sr and ^{139}Ba using penning trap mass spectrometry. *Phys. Rev. C*, 100:024309, Aug 2019.

[56] H. Savajols. The speg mass measurement program at ganil. *Hyperfine Interactions*, 132:243–252, 01 2001.

[57] G. Savard, R.C. Barber, D. Beeching, F. Buchinger, J.E. Crawford, S. Gulick, X. Feng, E. Hagberg, J.C. Hardy, V.T. Koslowsky, J.K.P. Lee, R.B. Moore, K.S. Sharma, and M. Watson. The canadian penning trap mass spectrometer. *Nuclear Physics A*, 626(1-2):353–356, nov 1997.

[58] H. Schatz and W. Ong. Dependence of x-ray burst models on nuclear masses. *The Astrophysical Journal*, 844, 10 2016.

[59] P. Schury, T. Niwase, M. Wada, P. Brionnet, S. Chen, T. Hashimoto, H. Haba, Y. Hirayama, D. S. Hou, S. Iimura, H. Ishiyama, S. Ishizawa, Y. Ito, D. Kaji, S. Kimura, H. Koura, J. J. Liu, H. Miyatake, J.-Y. Moon, K. Morimoto, K. Morita, D. Nagae, M. Rosenbusch, A. Takamine, Y. X. Watanabe, H. Wollnik, W. Xian, and S. X. Yan. First high-precision direct determination of the atomic mass of a superheavy nuclide. *Phys. Rev. C*, 104:L021304, Aug 2021.

[60] S. Schwarz, G. Bollen, R. Ringle, J. Savory, and P. Schury. The lebit ion cooler and buncher. *Nuclear Instruments and Methods in Physics Research Section A Accelerators Spectrometers Detectors and Associated Equipment*, 816:131–141, 04 2016.

[61] G. Sikler, D. Ackermann, F. Attallah, D. Beck, J. Dilling, S.A. Eliseev, H. Geissel, D. Habs, S. Heinz, F. Herfurth, F. Heßberger, S. Hofmann, H.-J. Kluge, C. Kozhuharov, G. Marx, M. Mukherjee, J. Neumayr, W.R. Plaß, W. Quint, S. Rahaman, D. Rodrıguez, C. Scheidenberger, M. Tarisien, P. Thirolf, V. Varentsov, C. Weber, and Z. Zhou. First on-line test of shiptrap. *Nuclear Instruments and Methods in Physics Research Section B: Beam Interactions with Materials and Atoms*, 204:482–486, 2003. 14th International Conference on Electromagnetic Isotope Separators and Techniques Related to their Applications.

[62] M. Smith, M. Brodeur, T. Brunner, S. Ettenauer, A Lapierre, R. Ringle, V. L. Ryjkov, F. Ames, P. Bricault, G. W. F. Drake, P. Delheij, D. Lunney, F. Sarazin, and J. Dilling. First penning-trap mass measurement of the exotic halo nucleus ^{11}Li. *Phys. Rev. Lett.*, 101:202501, Nov 2008.

[63] Andrew W. Steiner, James M. Lattimer, and Edward F. Brown. The equation of state from observed masses and radii of neutron stars. *The Astrophysical Journal*, 722(1):33, sep 2010.

[64] H. Stolzenberg, St. Becker, G. Bollen, F. Kern, H.-J. Kluge, Th. Otto, G. Savard, L. Schweikhard, G. Audi, and R. B. Moore. Accurate mass determination of short-lived isotopes by a tandem penning-trap mass spectrometer. *Phys. Rev. Lett.*, 65:3104–3107, Dec 1990.

[65] C.S. Sumithrarachchi, D.J. Morrissey, S. Schwarz, K. Lund, G. Bollen, R. Ringle, G. Savard, and A.C.C. Villari. Beam thermalization in a large gas catcher. *Nuclear Instruments and Methods in Physics Research Section B: Beam Interactions with Materials and Atoms*, 463:305–309, 2020.

[66] L.J. Sun, X.X. Xu, S.Q. Hou, C.J. Lin, J. José, J. Lee, J.J. He, Z.H. Li, J.S. Wang, C.X. Yuan, F. Herwig, J. Keegans, T. Budner, D.X. Wang, H.Y. Wu, P.F. Liang, Y.Y. Yang, Y.H. Lam, P. Ma, F.F. Duan, Z.H. Gao, Q. Hu, Z. Bai, J.B. Ma, J.G. Wang, F.P. Zhong, C.G. Wu, D.W. Luo, Y. Jiang, Y. Liu, D.S. Hou, R. Li, N.R. Ma, W.H. Ma, G.Z. Shi, G.M. Yu, D. Patel, S.Y. Jin, Y.F. Wang, Y.C. Yu, Q.W. Zhou, P. Wang, L.Y. Hu, X. Wang, H.L. Zang, P.J. Li, Q.Q. Zhao, H.M. Jia, L. Yang, P.W. Wen,

F. Yang, M. Pan, X.Y. Wang, Z.G. Hu, R.F. Chen, M.L. Liu, W.Q. Yang, and Y.M. Zhao. Experimentally well-constrained masses of 27p and 27s: Implications for studies of explosive binary systems. *Physics Letters B*, 802:135213, 2020.

[67] J. Surbrook, G. Bollen, M. Brodeur, A. Hamaker, D. Pérez-Loureiro, D. Puentes, C. Nicoloff, M. Redshaw, R. Ringle, S. Schwarz, C. S. Sumithrarachchi, L. J. Sun, A. A. Valverde, A. C. C. Villari, C. Wrede, and I. T. Yandow. First penning trap mass measurement of ^{36}Ca. *Phys. Rev. C*, 103:014323, Jan 2021.

[68] A. A. Valverde, G. Bollen, M. Brodeur, R. A. Bryce, K. Cooper, M. Eibach, K. Gulyuz, C. Izzo, D. J. Morrissey, M. Redshaw, R. Ringle, R. Sandler, S. Schwarz, C. S. Sumithrarachchi, and A. C. C. Villari. First direct determination of the superallowed β-decay Q_{EC} value for ^{14}O. *Phys. Rev. Lett.*, 114:232502, Jun 2015.

[69] A. A. Valverde, M. Brodeur, G. Bollen, M. Eibach, K. Gulyuz, A. Hamaker, C. Izzo, W.-J. Ong, D. Puentes, M. Redshaw, R. Ringle, R. Sandler, S. Schwarz, C. S. Sumithrarachchi, J. Surbrook, A. C. C. Villari, and I. T. Yandow. High-precision mass measurement of ^{56}Cu and the redirection of the *rp*-process flow. *Phys. Rev. Lett.*, 120:032701, Jan 2018.

[70] S. Weinberg and S. B. Treiman. Electromagnetic corrections to isotopic spin conservation. *Phys. Rev.*, 116:465–468, Oct 1959.

[71] R.N. Wolf, F. Wienholtz, D. Atanasov, D. Beck, K. Blaum, Ch. Borgmann, F. Herfurth, M. Kowalska, S. Kreim, Yu. A. Litvinov, D. Lunney, V. Manea, D. Neidherr, M. Rosenbusch, L. Schweikhard, J. Stanja, and K. Zuber. Isoltrap's multi-reflection time-of-flight mass separator/spectrometer. *International Journal of Mass Spectrometry*, 349-350:123–133, 2013. 100 years of Mass Spectrometry.

[72] Robert Wolf, Markus Eritt, Gerrit Marx, and Lutz Schweikhard. A multi-reflection time-of-flight mass separator for isobaric purification of radioactive ion beams. *Hyperfine Interactions*, 199:115–122, 07 2011.

[73] J. W. Xia, W. L. Zhan, B. W. Wei, Y. J. Yuan, M. T. Song, W. Z. Zhang, X. D. Yang, P. Yuan, D. Q. Gao, H. W. Zhao, X. T. Yang, G. Q. Xiao, K. T. Man, J. R. Dang, X. H. Cai, Y. F. Wang, J. Y. Tang, W. M. Qiao, Y. N. Rao, Y. He, L. Z. Mao, and Z. Z. Zhou. The heavy ion cooler-storage-ring project (HIRFL-CSR) at Lanzhou. *Nuclear Instruments and Methods in Physics Research A*, 488(1-2):11–25, August 2002.

[74] Y. H. Zhang, H. S. Xu, Yu. A. Litvinov, X. L. Tu, X. L. Yan, S. Typel, K. Blaum, M. Wang, X. H. Zhou, Y. Sun, B. A. Brown, Y. J. Yuan, J. W. Xia, J. C. Yang, G. Audi, X. C. Chen, G. B. Jia, Z. G. Hu, X. W. Ma, R. S. Mao, B. Mei, P. Shuai, Z. Y. Sun, S. T. Wang, G. Q. Xiao, X. Xu, T. Yamaguchi, Y. Yamaguchi, Y. D. Zang, H. W. Zhao, T. C. Zhao, W. Zhang, and W. L. Zhan. Mass measurements of the neutron-

deficient ^{41}Ti, ^{45}Cr, ^{49}Fe, and ^{53}Ni nuclides: First test of the isobaric multiplet mass equation in fp-shell nuclei. *Phys. Rev. Lett.*, 109:102501, Sep 2012.

APPENDIX A

Hardware

The MCP detector system in this section was purchased from Roentdek-Handels GmbH (Roentdek). Technical specifications for these components not included here can be found at their website `http://www.roentdek.com/`. Ion positions are detected with the PS-MCP with a delay line anode, signals pre-processed and transmitted from vaccuum to air with the FT12TP A.2, filtered and converted to a Nuclear Instrument Models (NIM) standard signal by the ATR19 A.3, and finally converted from a timing pulse to a digital signal by the TDC8HP A.4. The digital signals are then sent to the LEBIT-ROENTDEK computer to be gathered and assigned positions by CSPPapp C.1. This process is visualized in Figure A.1.

A.1 Position Sensitive MCP and Delay Line Anode

PI-ICR requires the ability to detect an ion's location in order to be able to determine the phase of the ion. This is achieved using a position sensitive microchannel plate (PS-MCP) detector coupled with a delay line anode. The PS-MCP is composed of two image-quality Hamamatsu MCPs stacked in a chevron configuration. The MCPs have an active diameter of 40mm, a thickness of 1.5mm each, and together provide a gain up to G= 10^{14} [22]. The two MCPs are held in place by a pair of ceramic rings with an inner conductive ring for biasing the front and back of the MCP stack. The ceramic rings are pushed together by four spring clamps, keeping the entire stack in place. The stack, electrically isolated from the rest of the system by the ceramic rings, is housed in the anode holder, which supports and isolates the delay-line wires.

When in operating mode, a negative bias of up to -2400 V is applied to the front MCP (the one facing incoming ions) while the back MCP is held at ground. The two MCPs are

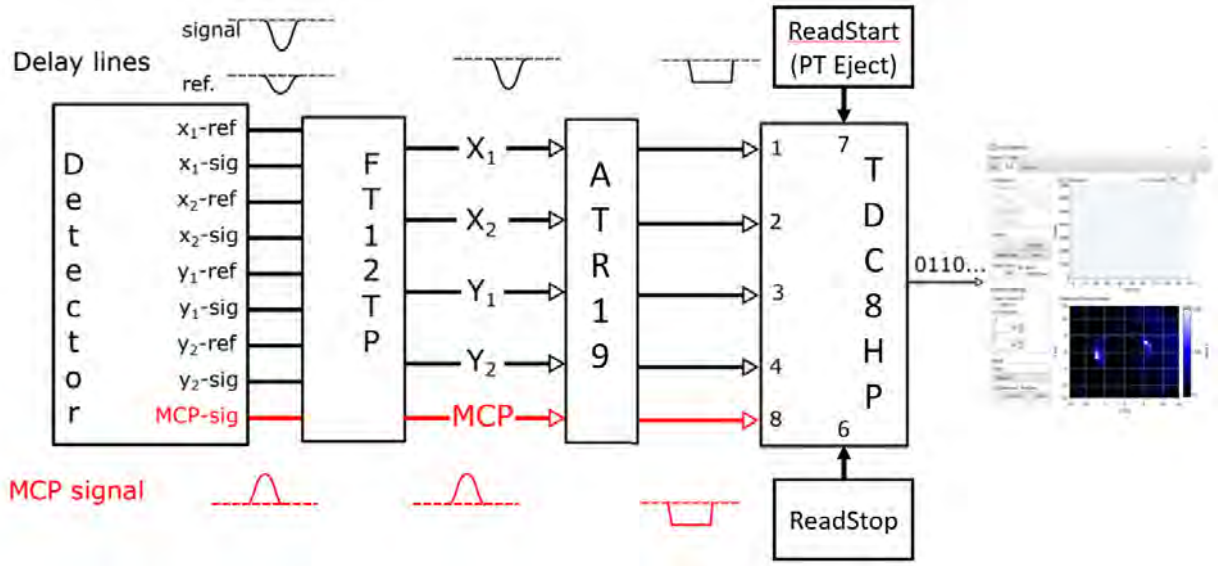

Figure A.1: Diagram showing the flow of signals from detector to computer. Adapted from [44]

resistively matched so that both see the same voltage applied. When an ion strikes the front MCP, an electron shower is generated. These electron shower is amplified by striking a series of pores in the MCP, which act as dynodes, multiplying the number of electrons in the shower in each layer. The substantial electron cloud generated at the back of the MCP stack then drifts towards the positively biased delay lines. The MCPs must be in a sufficiently low magnetic field zone (< 50 Gauss) in order to avoid distorting the path of the electron cloud. The delay lines form a tightly spaced grid of wires which allow the timing of current pulses generated by the electron shower to be converted into positions.

The mechanism of the delay line, and a photograph of the delay line anode used at LEBIT, can be seen in Figure A.2. The two delay lines are arranged in a perpendicular configuration so that the x and y positions can be simultaneously measured. Each delay line consists of a pair of copper wires wrapped around ceramic support structures. One of these wires is a "signal" wire, the other a "reference" wire. The signal wire is slightly more positively biased than the reference wire, causing the electron cloud to drift predominantly

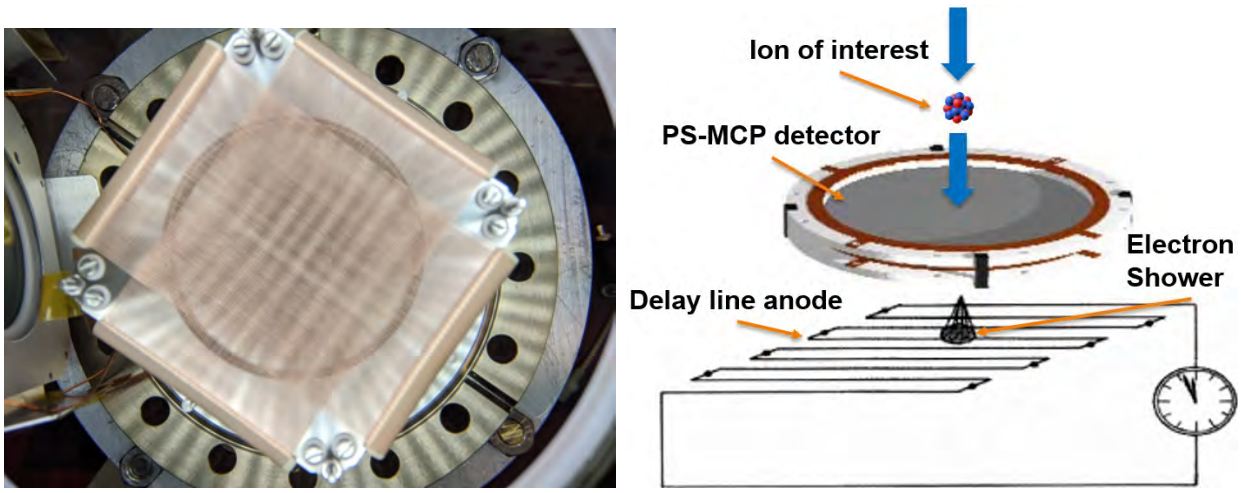

Figure A.2: A picture of the delay line anode (left) consisting of two pairs of delay lines arranged in a grid. A diagram showing how a delay line operates (right) shows that an electron shower striking a wire produces a unique pair of time of arrival signals which precisely correlate to the position of the shower in one dimension. Two stacked delay lines are used to acquire the 2D x-y position.

to it. Electrons collected on the signal wire generate a current pulse to propagate to each endpoint of each delay line, and the time of arrival of each signal is measured. When the ions strike the MCP, a current pulse is generated in the MCP, and the time is measured and used as t=0, the time delay line signals are measured with respect to. The four timing signals generated by the electron shower generated by the ion MCP strike are called $x1, x2, y1$, and $y2$.

The delay lines are electrically isolated, so great caution should be taken whenever it is removed from vacuum, as even a small speck of dust could create contact between the extremely closely spaced wires. Spraying down the delay line and MCPs with a can of compressed air or dry nitrogen is recommended before placing or replacing the setup in a vacuum system. Don't just blow own it, spit is not better than dust!

A.2 FT12TP vacuum feedthrough

The MCP and delay line produce nine useful outputs, one signal and one reference for each of $x1, x2, y1$, and $y2$, and one MCP signal. These signals must be both reduced down to the

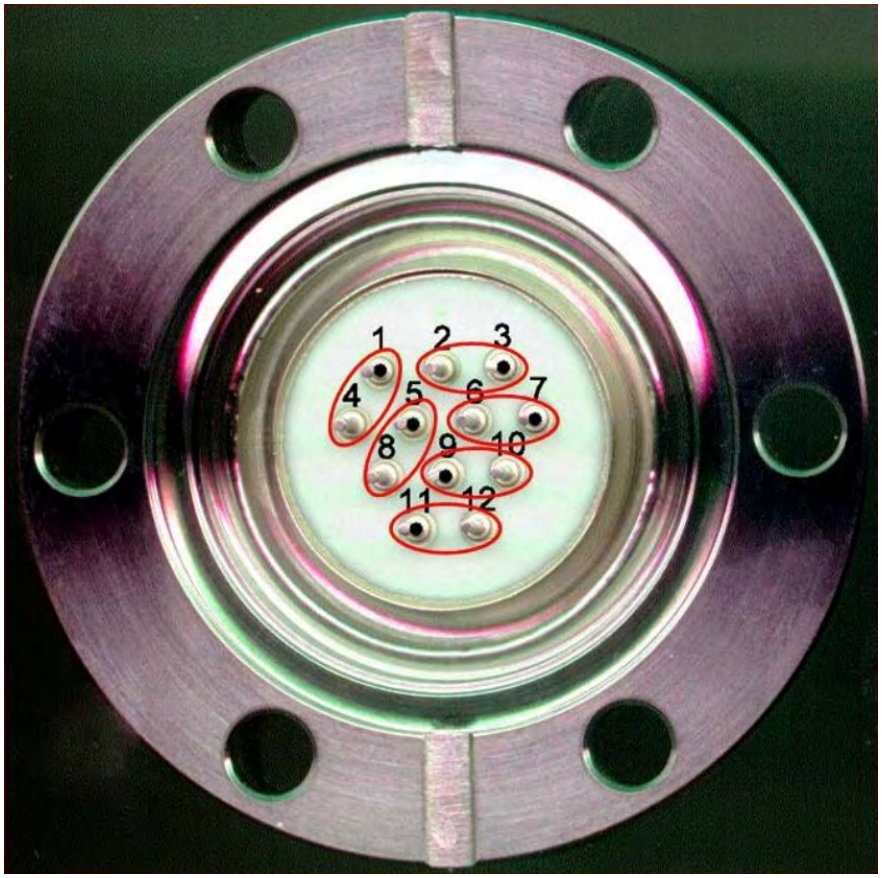

Figure A.3: Pinout for the vacuum side of the FT12TP. On the air side the pin numbers will be mirrored (e.g. top left pin is #3). Red ovals mark the pins for twisted cable pairs

five timing signals required for a position measurement. They must be transmitted from the vacuum where the MCP and delay line reside, to the air side for processing. This is achieved with the FT12TP vaccuum feedthrough, which is composed of a 12-pin vacuum feedthrough and air side connector plug. In addition to providing output signals, the vacuum feedthrough provides a means of biasing the relevant electrodes in the vacuum with power supplies on the air side. On the vacuum side, each signal is paired with another in a twisted pair configuration in order to minimize noise. Figure A.3 shows the vacuum side pin configuration, the red ovals mark the pins for twisted cable pairs. Table A.1 shows the pin assignments, typical bias voltages applied, and relevant input and outputs on the connector plug of the FT12TP.

The FT12TP connector plug slides into the cylindrical vacuum feedthrough assembly,

Pin #	Function	Bias (V)	Connector Plug I/O
1	Mesh (unused)	0	X (in)
2	MCP Front	2350	Front (in)
3	MCP Back	0	Back (in)
4	Anode Holder	0	Holder (in)
5	x1-reference	250	Ref (in), x1 (out)
6	x2-signal	286	Sig (in), x2 (out)
7	x2-reference	250	Ref (in), x2 (out)
8	x1-signal	286	Sig (in), x1 (out)
9	y1-reference	250	Ref (in), y1 (out)
10	y1-signal	286	Sig (in), x1 (out)
11	y2-reference	250	Ref (in), y2 (out)
12	y2-signal	286	Sig (in), y2 (out)

Table A.1: Pin assignments for the FT12TP vacuum feedthrough. Pin numbers in Figure A.3. Typical voltages shown in volts, 0 means the input is grounded with a 50 Ohm terminator. All inputs "(in)" are biases applied by external supplies, and have BNC inputs. All outputs "(out)" are LEMO.

providing 12 insulated slots for the pins to form connections through. This connection can become loose very easily, especially when working with the cabling on the connector plug. Even slightly jiggling the FT12TP can generate noise enough to drown out any real ion detection signal. A solution was to use the screw holes on the top and bottom of the FT12TP plug. A pair of screws were inserted into these holes with washers to ensure a tight fit and stable mounting, visible in A.4.

The LEMO cables carrying the four position and MCP signals from the FT12TP to the ATR19 constant fraction discriminator (CFD) were provided by Roentdek. These cables have the same length so no signal is delayed, which would lead to an error in ion position determination.

A.3 ATR19 Constant Fraction Discriminator

The five timing signals must be amplified, filtered from noise, and converted into NIM signals before they can be processed. This is all the job of the ATR19 constant fraction discriminator. The ATR19 has 6 inputs which provide amplification and discrimination for

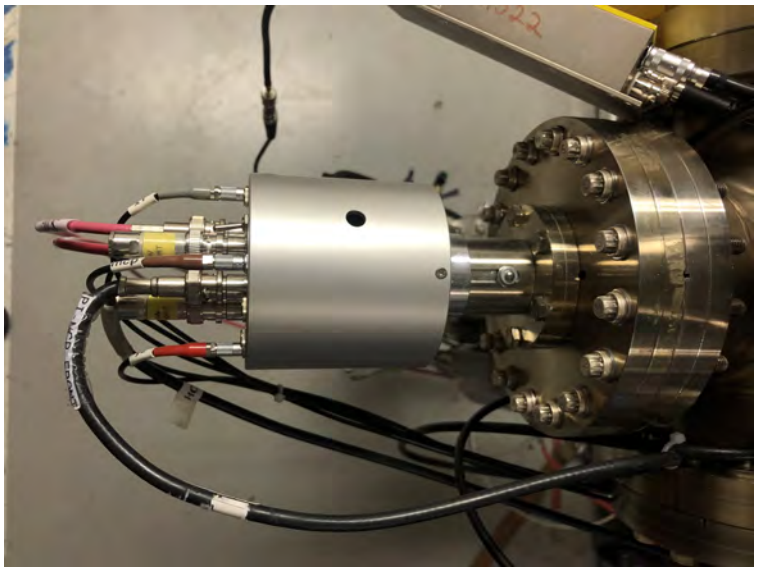

Figure A.4: The FT12TP vacuum feethrough and connector plug. A screw and pair of washers have been mountede on the right, just before the flange to keep the plug more stable. There is an identical screw and washer pair 180° away on the bottom side with the same function.

Figure A.5: The ATR19 constant fraction discriminator front panel. Two channels of six are shown.

the incoming signals, see Figure A.5. By default channels 1 and 2 are inverting amplifiers, and either is meant for the MCP signal, which is a positive pulse. Channels 3-6 are non-inverting, and are meant for the position signals which are negative. Each channel has an adjustable amplification gain between 20 and 100. The gain can in almost all circumstances be left unchanged, as adjusting the discrimination is a better way to manage signal quality.

Which input is used must match the polarity of the pulse being sent, i.e. "In+" for the positive MCP pulse, "In-" for the negative position pulses; the unused input should be

terminated with a 50 Ohm terminator in order to minimize potential noise. "NIM" provides a NIM signal of the amplified, discriminated input. "ECL" outputs a timing signal for the constant fraction discriminator circuit, and is unused in LEBIT. "Mon" provides an amplified but non-discriminated signal, and is useful for looking at the noise level of any of the input signals. "Width" outputs the duration of the NIM signal. Finally, "Threshold" outputs a voltage between 0 and +5V, adjustable via the potentiometer to the right of the LEMO connector. This voltage corresponds to the amplified voltage the input–as measured on "Mon"–must reach in order for a NIM signal to be produced.

The process for determining thresholds is as follows:

1. Send ions to the MCP at a reasonable rate, $\sim 1 - 20$ions/shot
2. Connect the "NIM" signal of the channel whose threshold is being calibrated to an oscilloscope.
3. Set the oscilloscope to trigger on the trap ejection signal. There should be a cluster of signals on every channel indicating detected ions within 100 us of the trap ejection signal.
4. Reduce the threshold until noise signals are clearly being generated.
5. Increase the threshold just until this noise disappears. Zoom out on the oscilloscope's time domain to ensure noise is observed only rarely (1 noise signal per $\sim$ 20-50 shots)
6. Repeat for each channel
7. To verify, plug all "NIM" outputs into the oscilloscope. Ensure that the majority of the time, if at least two signals trigger, all signals trigger (1 missing NIM per $\sim$ 20-50 shots)

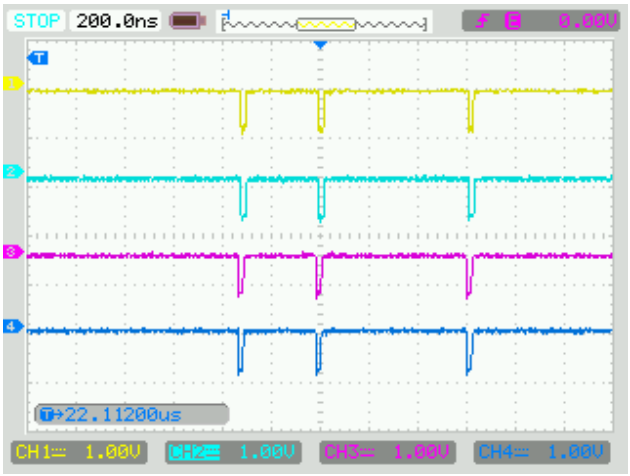

Figure A.6: Sample NIM signals heading to TDC8HP. When one signal arrives, all signals arrive, indicating a well tuned set of thresholds. One should still zoom out and ensure that no channels are swamped by noise.

8. reduce the threshold of any signal that is missing more consistently than others. Some noise on one channel is better than regularly losing all position data due to one insensitive channel.

An example of healthy looking signals going from the ATR19 into the TDC8HP is available in Figure A.6

While these levels are reasonably stable, the PS-MCP degrades over time, and power supplies drift, therefore this process should be performed before any important experiment to ensure good data is not being lost.

A.4 TDC8HP

The destination for the output NIM signals from the ATR19 is the data acquisition system: the TDC8HP. The TDC (Time to Digital Converter) has 10 NIM-compatible LEMO inputs, the first 8 of which are high resolution inputs with 25 ps bin sizes, the last two channels are low resolution inputs with 12.8 ns bin sizes, and unused at LEBIT. Table A.2 shows the required input of each channel. Just like the cables from the FT12TP to the ATR19, the cables from the ATR19 to the TDC8HP must be identical in length, as differences will cause

Channel	Signal
1	x1
2	x2
3	y1
4	y2
5	unused
6	read stop
7	read start
8	MCP
Clock	unused
Trigger	unused

Table A.2: Input assignments for the TDC8HP. Signals 1-4 and 8 originate from the ATR19. Signals 6 and 7 originate from a programmable timing generator.

signal delays, and impact the measured position.

A position measurement begins with the "read start" signal. This signal is generated by a controllable timing generator, and is exactly the same signal sent to the switch which puts the ejection side correction tube and endcap in the low position. It tells the TDC to begin reading data as soon as ions are ejected from the Penning trap. It also serves as t=0 for the purpose of calculating time of flight. Next, an MCP signal is received, indicating an ion has struck the PS-MCP. It acts as "stop" signal for the ToF, and a "start" signal for the delay line signals. Next, the four delay-line signals arrive in an order depending on the position the electron cloud struck the delay line. The equation determining position is simply

$$X = x1 - x2 + O_x \text{ and } Y = y1 - y2 + O_y \tag{A.1}$$

where $x1, x2, y1$, and $y2$ are the time, in ns, between the MCP trigger at the arrival of the identically named delay line position signal. O_x and O_y are arbitrary timing offsets. These yield a position in ns, an unusual choice for a position. The position can be converted to mm by multiplying by a constant, $k \approx .67$mm/ns, which is dependent on the pulse propagation speed and winding in the delay line. It is usually unnecessary to make this conversion as all

calculation in PI-ICR use relative phases, therefor the distance units cancel out. The delays for any given position measurement,

$$sumx = x1 + x2 \text{ and } sumy = y1 + y2, \tag{A.2}$$

are constant within less than one ns, a fact which is used to filter out noise signals. All five signals must successfully reach the TDC in order for a position to be recorded. If one or more of MCP, $x1, x2, y1$, or $y2$ are missing, the position cannot be calculated, and the data is neglected. Finally, the "read stop" signal arrives, usually $\sim$100 us after the "read start" signal, and data acquisition stops until the next bunch of ions is ejected from the Penning trap. This gating of accepted signals drastically cuts down on measured noise.

The TDC outputs is connected to a desktop computer, lebit-roentdek, via a PCI connector. This computer is used solely for processing PI-ICR data.

APPENDIX B

MM8 For PI-ICR

The LEBIT experiment control and data acquisition, MM8, and it's predecessors, MM6, have long been used to control timings and RF excitations at several PTMS facilities around the world. It is primarily used for conducting TOF-ICR, but the requirements for PI-ICR are extremely similar. This appendix will briefly explain how to set up MM8 to generate every different type of beam spot required to perform PI-ICR. These different spot types are all described in greater detail in Section 2.6. Note that much of this is extremely specific to the LEBIT control system and may not be relevant for other labs.

B.1 Relevant MM8 Panels

In order to make any changes to MM8, first the "Load config" panel, Figure B.1, must be opened by either pressing ctrl+s, or clicking the blue folder symbol at the top left of the MM8 main panel. While there are an almost overwhelming number of options on this panel, fear not, most of them do not need to be changed. Only the values in the red boxes (added) need to be manually adjusted for running all basic PI-ICR measurements.

There are several setting in these boxes which are rarely or never changed.

- Scan1: Usually 00dummy, indicating no value is being scanned over. The exception is when generating an ellipse to find trap center's projection onto the MCP, when Scan1 must be set to timing_C. This varies magnetron phase accumulation time, called "mag-wait" or "t_{acc-}", in order to paint an elliptical projection of the circular ion path onto the MCP.

- Scan2: Always 00noscan, indicating no 2D scan is being performed.

- ACQ: Currently MM8 doesn't acquire PI-ICR data, so irrelevant. In the future PI-ICR

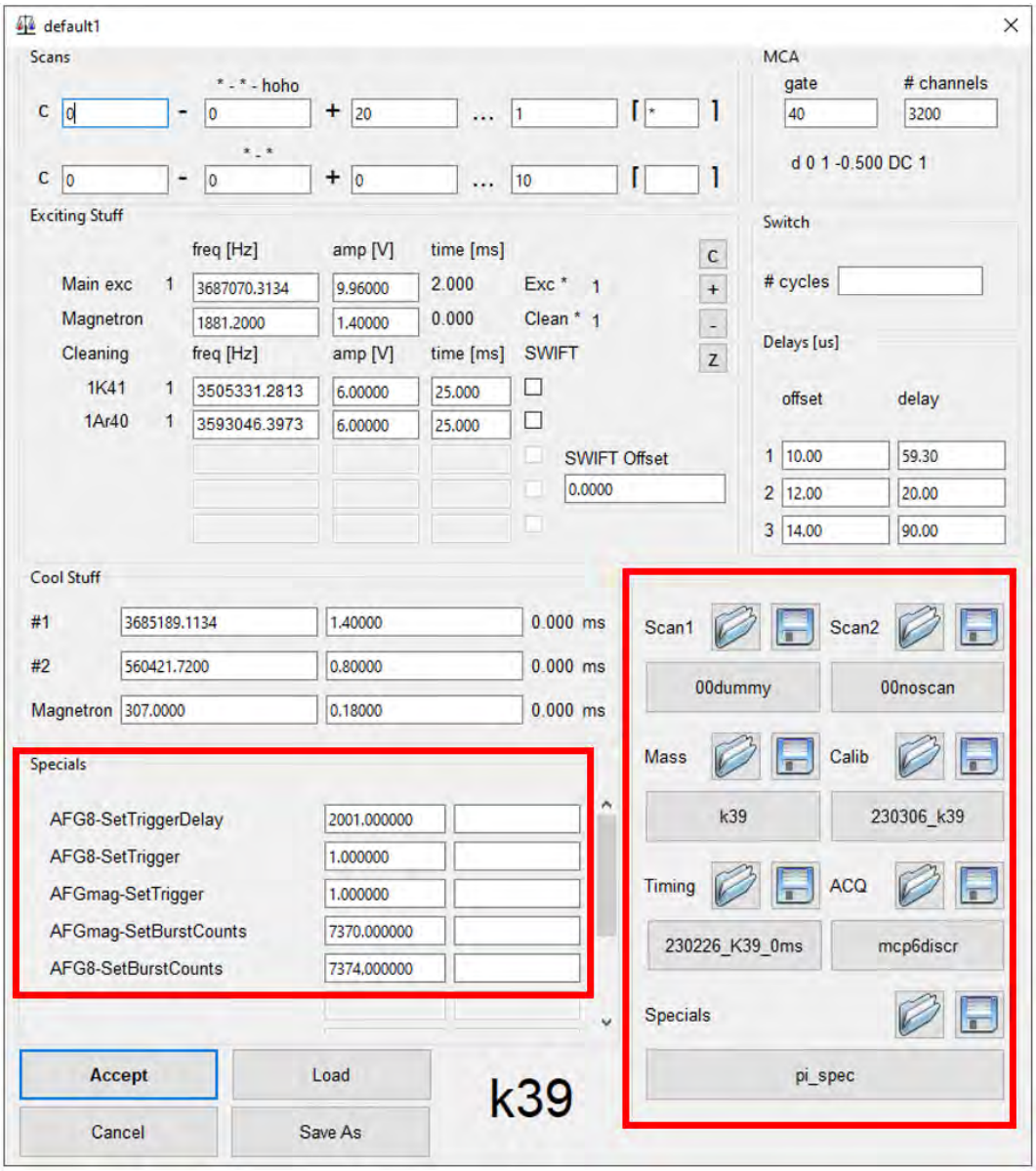

Figure B.1: The Load config panel of MM8. All timing and RF changes are made here. Red boxes added to this figure to show the setting which must be manually changed

will be integrated into MM, and this will have to be PS-MCP.

- AFG8-SetTrigger: Always 1.0. This tells AFG8 to run in triggered burst mode instead of free-running. AFG8 performs quadrupole conversions at F_c to convert from fast reduced cyclotron to slow magnetron motion before ejection

- AFGmag-SetTrigger: Always 1.0. This tells AFGmag to run in triggered burst mode instead of free-running. AFGmag performs dipole excitations at F_+ to move ions of interest from trap center to off-center.

The value for Calib must be periodically updated by measuring at least two of F_c, F_+ and F_- of a stable isotope of well known mass. These measurements can be made using either TOF-ICR or PI-ICR, and should only need to be done when the magnetic field compensator is reset. This calibration is used to calculate the RFs applied in the trap for any mass, assuming a simple linear relationship between mass and F_c, and that F_- is mass independent–a reasonable approximation here but not always. Due to the short, high amplitude excitations and conversion times, usually 2 ms each, PI-ICR is quite insensitive to poorly calibrated RFs being applied, so these only need to be accurate to within a $\sim$5 Hz. The Calibration panel can be seen on the left in Figure B.2. To update it, a new file including the current date can species of the calibrant should be saved. The species and charge info of the calibrant nuclide should be set. The two measured frequencies should be set in the "main trap" section, to the right of the label corresponding to which frequencies were measured. Finally, the calculate "c" button should be pressed on the unmeasured frequency to calculate it based on Equation 2.5. Accept than then be clicked, nothing else needs to be regularly adjusted.

The first step of any measurement type is to ensure that the correct mass file is selected. This file adjusts all mass dependent parameters such as the excitation and conversion fre-

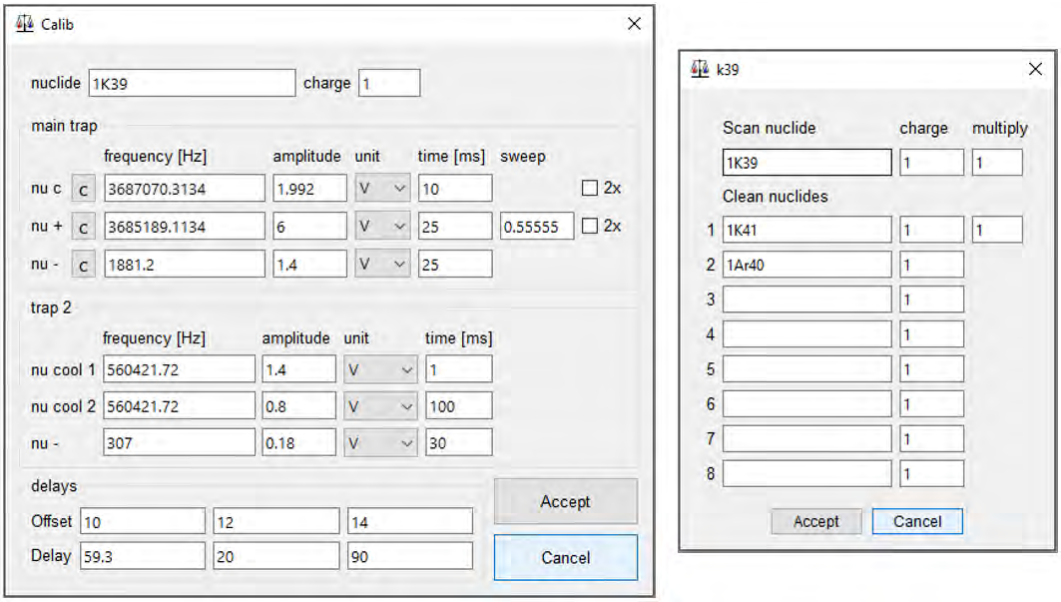

Figure B.2: The Calibration (left) and Mass (right) panels of MM8.

quencies, F_+ and F_c respectively, or the time-of-flight gate located after the buncher. It also lists expected contaminants for the selected species which can be cleaned. There are already a multitude of mass files created in the past which have common contaminants included, so check if there is already a mass file of the species to be measured by clicking the blue folder to the right of "Mass" in the Load config panel to check if the species being measured already has a mass file. It is good practice to open the mass file and ensure that its name actually matches the species listed in the mass file. An example mass panel can be seen on the right of Figure B.2. To create a new mass file, save the file as just the name of the species being measured (e.g. "k39", fe56 or "co2") then in the "Scan Nuclide" box, enter the name of the species to be measured using correct capitalization, mass A, and multiplicity of each component chemical of the species (e.g. 1K39, 1Fe56, or 1C12:2O16). Enter the charge of the species in the "charge" box it is usually 1, and occasionally 2. Finally, enter any known contaminants in the same manner under "Clean nuclides" 1-5 (channels 6-8 are not used in LEBIT) and Accept can be clicked. If any of the cleaned nuclides are too close in frequency

to the nuclide of interest, such that if that cleaning is used, the species of interest will be cleaned as well, then the reduced cyclotron frequency of that contaminant species will be highlighted in red in the cleaning section of the Load config panel.

The rest of the adjustments depend on the type of measurement being made. The values mag-wait and PhaseAccum will be referenced frequently, they can be found in the timing panel, in the red box in Figure B.3

B.2 No Phase Accumulation Spot and Ellipse

The start phase, spot 1 in Figure 2.6 and pulse scheme from 2.8, is measured as follows:

1. Set Scan1 to 00dummy
2. Save appropriately named Timing and Specials files, e.g. "230309_k39_0ms.xml"
3. Set mag-wait in the Timing panel to 1.0 us
4. Set PhaseAccum in the Timing panel to 1.0 us
5. Set AFG8-SetTriggerDelay in the Specials section of the Load config panel to the excitation time (2000 us) plus PhaseAccum
6. Set AFGmag-SetBurstCounts in the Specials section of the Load config panel to the product of F_+ (can be acquired by clicking the "+" button on the right side of the "Exciting Stuff" section) and excitation time (.002 s)
7. Set AFG8-SetBurstCounts in the Specials section of the Load config panel to the product of F_c (can be acquired by clicking the "c" button on the right side of the "Exciting Stuff" section) and conversion time (.002 s)

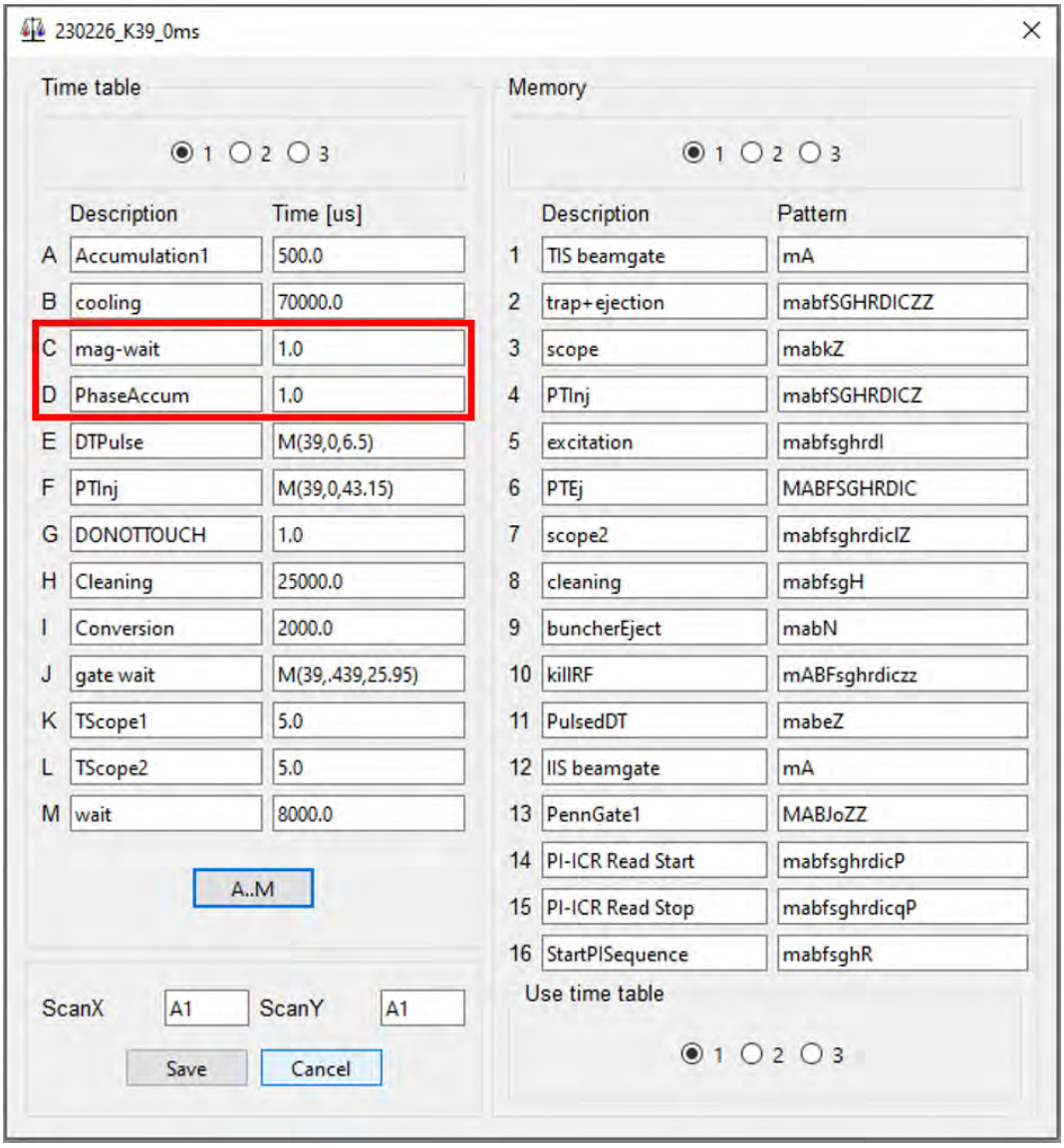

Figure B.3: The Timing panel. Red box added to this figure to show the two values which must regularly be manually changed. Mag-wait is t_{acc-} and PhaseAccum is t_{acc+}, as referenced in Figures 2.9and 2.10 respectively.

8. Hit accept, and begin the MM8 scan, observe the data with the GUI described in Section C.4

9. If desired, adjust both PhaseAccum and AFG8-SetTriggerDelay in order to adjust the phase of the start spot. MM8 has a resolution of 25ns, so these values must always end in ".X00, .X25, .X50, or .X75" where X is the hundreds place number of ns.

10. When satisfied with how the spot looks save the settings by clicking Save As, navigating to "I:/projects/lebit/Data Exchange/MM8/PISavedMainXML" and saving an XML file with a descriptive name, e.g. k39_0ms_20230208.xml. Make sure to hit "Accept" after saving this file, or the XML file will *not* be saved.

In order to run an Ellipse scan, simply replace Scan1 with a timing_C scan over 1 magnetron period in at least 10 steps. Unless the trap depth is changed from endcap = 23.41 V F_- should stay relatively constant, so a good range is 540 us ± 255 us in steps of 15 us.

B.3 F_- Phase Accumulation

The Magnetron final phase, spot 2 in Figure 2.6 and pulse scheme from 2.9, is measured as follows:

1. Set Scan1 to 00dummy

2. Save appropriately named Timing and Specials files, e.g. "230309_k39_F-_100ms.xml"

3. Set mag-wait in the Timing panel to the desired t_{acc-}. For a rare isotope measurement, this could be approximately its half-life. For a stable isotope any value from 1 ms to 400 ms is acceptable, precision scales linearly with this time. At times greater than 400 ms, spot smearing begins to cause losses in precision, though advances are likely to be made on this front, allowing for longer phase accumulation times.

4. Set PhaseAccum in the Timing panel to the same time that was used for the start phase.

5. Set AFG8-SetTriggerDelay in the Specials section of the Load config panel to the sum of the excitation time (2000 us) and PhaseAccum. If you've already measured a start phase for this species, the next two steps have already been performed and need not be repeated.

6. Set AFGmag-SetBurstCounts in the Specials section of the Load config panel to the product of F_+ (can be acquired by clicking the "+" button on the right side of the "Exciting Stuff" section) and excitation time (.002 s)

7. Set AFG8-SetBurstCounts in the Specials section of the Load config panel to the product of F_c (can be acquired by clicking the "c" button on the right side of the "Exciting Stuff" section) and conversion time (.002 s)

8. Hit accept, and begin the MM8 scan, observe the data with the GUI described in Section C.4

9. Adjust Magwait in order to adjust the phase of the final spot so that it is within $\pm \sim 10^\circ$ of the start phase. This minimizes phase dependent systematics, such as the elliptical nature of the projection.

10. When satisfied with how the spot looks save the settings by clicking Save As, navigating to "I:/projects/lebit/Data Exchange/MM8/PISavedMainXML" and saving an XML file with a descriptive name, e.g. k39_100ms_F-_20230208.xml. Make sure to hit "Accept" after saving this file, or the XML file will *not* be saved.

B.4 F_+ Phase Accumulation

The reduced cyclotron final phase, spot 2 in Figure 2.6 and pulse scheme from 2.10, is measured as follows:

1. Set Scan1 to 00dummy
2. Save appropriately named Timing and Specials files, e.g. "230309_k39_100ms.xml"
3. Set PhaseAccum in the Timing panel to the desired t_{acc+}. For a rare isotope measurement, this could be approximately its half-life. For a stable isotope any value from 1 ms to 400 ms is acceptable, precision scales linearly with this time. At times greater than 400 ms, spot smearing begins to cause losses in precision, though advances are likely to be made on this front, allowing for longer phase accumulation times.
4. Set mag-wait in the Timing panel to the same time that was used for the start phase.
5. Set AFG8-SetTriggerDelay in the Specials section of the Load config panel to the sum of the excitation time (2000 us) and PhaseAccum. Note this will be a much larger number than in the previous meausurements! If you've already measured a start phase for this species, the next two steps have already been performed and need not be repeated.
6. Set AFGmag-SetBurstCounts in the Specials section of the Load config panel to the product of F_+ (can be acquired by clicking the "+" button on the right side of the "Exciting Stuff" section) and excitation time (.002 s)
7. Set AFG8-SetBurstCounts in the Specials section of the Load config panel to the product of F_c (can be acquired by clicking the "c" button on the right side of the "Exciting Stuff" section) and conversion time (.002 s)

8. Hit accept, and begin the MM8 scan, observe the data with the GUI described in Section C.4

9. Adjust both PhaseAccum and AFG8-SetTriggerDelay in order to adjust the phase of the final spot so that it is within $\pm \sim 10^{\circ}$ of the start phase. MM8 has a resolution of 25ns, so these values must always end in ".X00, .X25, .X50, or .X75" where X is the hundreds place number of ns. This minimizes phase dependent systematics, such as the elliptical nature of the projection.

10. When satisfied with how the spot looks save the settings by clicking Save As, navigating to "I:/projects/lebit/Data Exchange/MM8/PISavedMainXML" and saving an XML file with a descriptive name, e.g. k39_100ms_20230208.xml. Make sure to hit "Accept" after saving this file, or the XML file will *not* be saved.

All of these scans will need to be performed for both a calibrant ion and an ion of interest in order to perform a mass measurement, therefore 8 XML files are necessary.

APPENDIX C

Software

The software used to perform and analyse PI-ICR is broken up into three categories. The first is the CS++ application, CSPPapp, created by Dr. Dennis Neidherr at GSI Helmholtz Centre for Heavy Ion Research. This program interfaces with the TDC and interprets raw binary data into useful positions. The second category is Python scripts developed to generate, analyse, and visualize PI-ICR data. These were developed by the author, and improved upon with the assistance of Scott Campbell, a LEBIT graduate student who is an extremely talented programmer. The latest version of the Python scripts can be found at `https://gitlab.msu.edu/yandowis/pi-icr-measurement-and-analysis`, and will likely have evolved from the time of this thesis's writing.

However, this document should still be useful as a guide for the general techniques used in these codes.

The third category is MM8 (Mass Measurement 8), a program currently maintained by Ryan Ringle which is used to control timings across the entire LEBIT lab in order to measure masses; instructions for using MM8 for PI-ICR is described in Appendix B.

C.1 CSPPapp

CSPPapp is software, written by Dr. Dennis Neidherr in CS++ to interface with the TDC8HP hardware to gather data and interpret it into positions and times of flight. It was chosen over Roentdek's Cobold software, as the Cobold cannot interpret the "read start" and "read stop" inputs to TDC8, which meant the output was always swamped with noise. CSPPapp's primary purpose is to provide real-time position data in an easy to parse format. It's real time plotting capabilities are not ideal for LEBIT purposes, as they do not include many data filtering options required to visualize clear beam spots. The acquisition

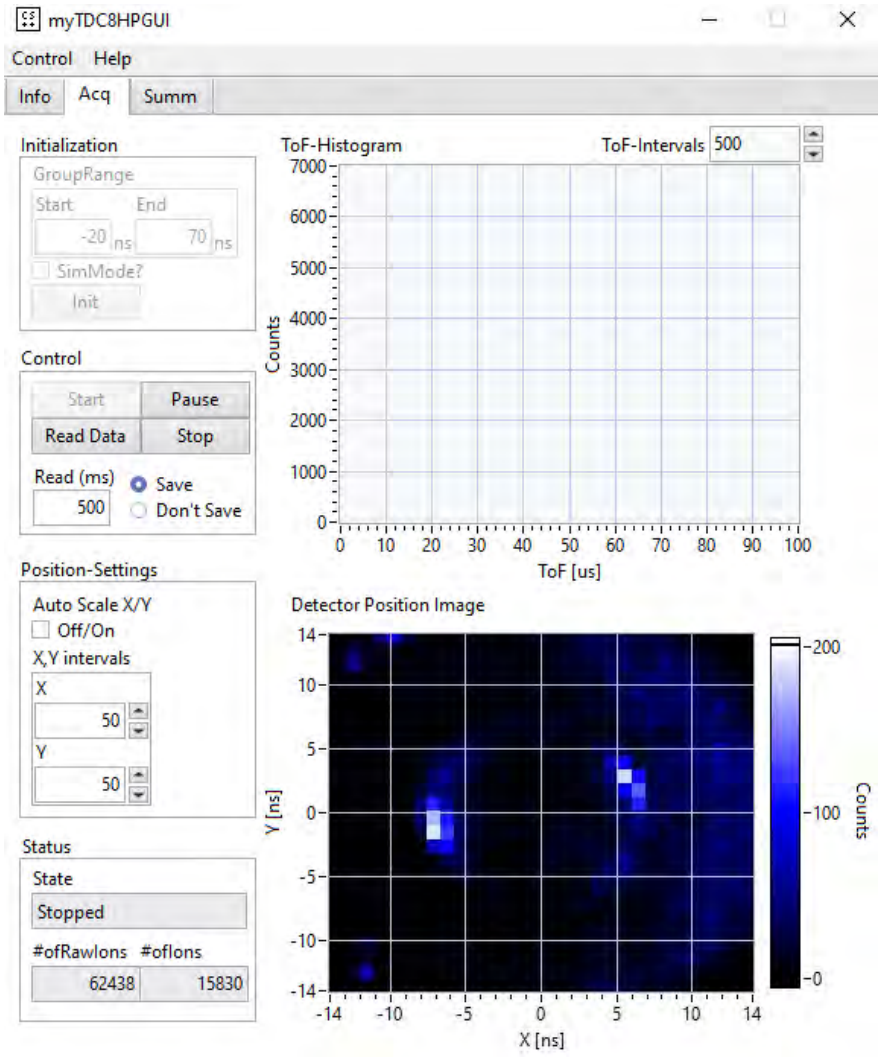

Figure C.1: The acquisition panel of CSPPapp, the only panel used at LEBIT. The two spots at $\sim (-7, -1)$ and $\sim (6, 2)$ are real ions, but the dark blue signals, especially along the right edge, is noise that perpetually accumulates along the edge of the PS-MCP.

panel of CSPPapp can be seen in Figure C.1. The two other panels Info and Summ, show version information and the values of *sumx* and *sumy* (see Equation A.2), respectively, and are not used at LEBIT.

When using CSPPapp at LEBIT, the process is almost always as simple as following these steps:

1. Set up and begin the appropriate MM8 scan (see Appendix B)

2. Select the save toggle

3. Press the Init button, this will cause the browser to open

4. Save the full file path as "I:/projects/lebit/DATA/currentPI-ICRData/CSPP_out"

5. Press Start, followed by Read Data, this begins data collection, and clears any junk data in the TDC

6. Change the value under Read (ms) to 500 ms. This is the update rate, and less than 500 ms is not recommended. By default it is -1, which tells the program to only add data when the Read Data button is pressed.

7. In order to clear the data, the easiest method is to hit Stop, Init, save over CSPP_out, Start.

Other options include:

- Edit GroupRange: a "group" defines the amount of time before and after the MCP signal which a delay line signal is allowed to arrive and be associated with that MCP signal. The default value of -20 to 70 ns is generous, and fine for resonable count rates.

- Pause: Pause the updating of data without stopping it from accumulating. Resume data updating by pressing Start.

- #ofRawIons and #ofIons: These show the number of ions accumulated. #ofRawIons includes all MCP hits, even those without four associated delay-line position signals. #ofIons is only ions with full position info. In a properly functioning system, #ofRawIons $< 4\times$#ofIons. If #ofRawIOns is much greater than this, it could indicate that the constant fraction discriminator needs to be re-calibrated (see Section A.3)

- Position Settings: Used to update position plotting options. See Section C.4 for position data display info.

The output produced by CSPPapp is a tab separated text file with data format:

triggerID time x y tof sumx sumy

Where "triggerID" is an integer which correlates to the number of times a "read start" signal has been received by the TDC; it is used to correlate number of ions, "z", released in each ejection from the Penning trap for count-class analysis. "time" is the Unix time stamp at which the MCP signal arrived. "x" and "y" are the position in units of nanoseconds; if any of the four delay line signals is missing, these are both set to "-99999999999999966000..." which makes them very easy to filter. "tof" is the time of flight in nanoseconds, as defined by the time between the "read start" signal and the arrival of the "MCP" signal. Finally, "sumx" and "sumy" are the total delay line delay on the x and y lines, respectively, as defined in Equation A.2.

C.2 AutoRunPIICR.py

The AutoRunPIICR.py script's function is to allow the user to set up every scan necessary to perform a mass measurement using PI-ICR, and then the system will automatically do it. While it could certainly be used for an on-line rare isotope measurement, it is often important to keep constant watch over the incoming data with valuable on-line beams. Therefore, this script shines when setting up a stable isotope measurement to run overnight. This section will outline how to use the script, the purpose of various functions.

The following steps are the only actions a regular user will need to take in order to run the code

1. Set up the MM8 XML files as described Appendix B. There are 8 XML files in total

required, one for the ion of interest and one for the reference for each of: ellipse, no phase accumulation, with F_+ phase accumulation, and with F_- phase accumulation.

2. Set the ion and reference source. An updated list of options is included in the code to the right of the variables "Ion1Source" and "Ref1Source", but common options are "TIS", for the thermal ion source without gas, "TISgas", for the same with gas injected into the chamber, "LAS", for the laser ablation source, and "D-line", for beam coming from the gas stopping facility. These sources are described in greater detail in Section 3.2.1.

3. Set desired TIS current. This option only needs to be used if "TISgas" is selected as one of the sources. Ionizing gasses in the TIS chamber rapidly degrades the tungsten filament, increasing resistance and therefore the power output per current applied. The TIS anode current can be regulated in order to avoid a runaway where the ion generation rate exponentially increases over time, and the filament is quickly broken.

4. Set number of scans for each file type. This is just the number of scans performed in MM8 before moving on to the next type. More scans means more statistics, but longer run times. Generally a value between 30 and 100 is appropriate for each of these, depending on the count rate of the reference or ion of interest.

5. Set number of loops to be performed, and the number of loops between each "calibration". In this case, the calibration is defined as measurement of each spot except for those with F_+ phase accumulation time. As this script is often run overnight, it is usually stopped manually in the morning so number of loops is set to an arbitrarily large number. The number of loops between calibration is usually from 10-20, but any value that allows for at least 2 calibrations to be made is acceptable.

With these steps performed, the script can be run and it will gather all data necessary to measure a mass using PI-ICR by performing the following steps:

1. Open all XML files to ensure they exist. This prevents the code from getting too far before the script errors out with the most common user error of misspelling a file name.

2. Switch the LEBIT system to the source set for the reference ion, making all necessary changes for ions to make it from the source to the trap

3. Run each calibration scan (i.e. ellipse, start phase, F_- phase accumulation) for the reference ion

4. Save the output data with a systematically generated name and a header in increase ease of analysis containing

    - Ion species and charge
    - F_+ and F_- phase accumulation time
    - the frequencies of the three eigenmotions in the trap as calculated based on the MM8 calibration file, F_c, F_+, and F_-,
    - The start time, middle time, and end time over which the data was collected, stored are the UNIX time stamp
    - whether or not the reference ion and ion of interest are isobars

5. Perform steps 2-4, but for the ion of interest.

6. Alternate between measurements of the reference ion and ion of interest with F_+ phase accumulation time. Measure each a number of times equal to the variable "LoopsBetweenCalibration", saving data with the same header as described in step 4.

7. Repeat all above steps a number of times equal to "NumLoops", then perform one final set of calibrations.

After the above code has run, the analysis script is ready to be run; all data has been gathered for a high precision mass measurement using PI-ICR.

C.3 RunAnalysis.py

The RunAnalysis script takes raw ion position data and analyses it, outputting data files in the exact same format as produced in analysis of ToF data, allowing them to be processed using the same tools. Running the analysis script is extremely straightforward. Simply input all the file numbers to be analysed, including all calibration files. In the script, this is the variable "all_files" which takes in a list of integers. Then run the script, that's it! There are several filters that can be adjusted:

- ToF bounds, "tofmin" and "tofmax": The minimum and maximum time of flight of valid data. The broadest bounds are ~ 5 us to ~ 100 us, but these can be narrowed to attempt to filter noise. Generally in PI-ICR, noise data is faster than good data, as its reduced cyclotron motion was not properly converted to magnetron motion, causing acceleration as these ions left the magnetic field. Therefore, it is good to increase tofmin so that the lowest values are cut out.

- Count rate maximum "zmax": the maximum number of ions allowed to arrive in one ejection from the trap. This is to minimize frequency shifts due to space charge interactions in the penning trap. Traditionally in TOF-ICR, this is set to zmax=5. However, it is known that the Daly configuration used in TOF-ICR increases counting efficiency, so the same number of ions in the trap correlates to a value closer to zmax=3 for PI-ICR. This is only relevant for very high precision mass measurements.

- Cluster thresholds and smoothing: these parameters adjust the thresholds for what is included in the cluster determined by the clustering neural network used to algorithmically filter out detected ions with positions far from the beam spot. There are separate parameters for clustering spots and ellipses. Broadly, decreasing cluster thresholds includes more data further from the densest ion clusters, increasing smoothing includes more data in a more symmetric manner by assuming that the valid spot or ellipse data is close to perfect in shape, but is thicker.

RunAnalysis.py performs the following operations when run:

1. Get all PI-ICR data files specified by the user.

2. Beginning with ellipse data, followed by all beam-spot data, filter out data which fall outside of the user defined position, time of flight, or count rate bounds.

3. Cluster the remaining data using Scott Campbell's custom neural network clustering tool. The details of this clustering algorithm will not delved into, but briefly, it can be stated that the neural network was trained on simulated data very similar to real noisy PI-ICR data as measured at LEBIT, including:

    - random noise
    - on-center noise from ions that were not excited outward
    - noise along the path of the ellipse from ions whose motion wasn't properly converted from reduced cyclotron to magnetron
    - tails on the real beam spot from ions with large axial oscillations leading to small frequency shifts.

It is custom made for PI-ICR, and does a superb job finding reasonable beam spots. It will likely be the topic of a paper in the near future, or part of a thesis in approximately four years.

4. Optional: Each set of clustered data is plotted, allowing the user to look for obvious errors, such as sudden drastic jumps in phase, severs smearing issues, or erroneous clustering.

5. The position of trap center is determined, which is why ellipse data must be processed first. Trap center found using ellipse measurements of the same species as the spot. Assuming that at least 2 ellipse measurements were performed the center value for any given beam spot is linearly interpolated over time. Normally, ellipse center is extremely stable.

6. Determine the phase and uncertainty in phase of each spot measured.

7. The start phase for each F_+ and F_- phase accumulation spot is determined by beam spots with no phase accumulation of the same ion species, again, linearly interpolated if at least 2 calibrations took place.

8. The magnetron frequency F_- is measured using equation 2.18, using the phase difference measured here, and number of full turns "n_-" calculated based on the MM8 value calculated from the calibration file. The value of F_- is calculated again using $n_- \pm 2$, and the value of n_- which yields a final result closest to the MM8 guess is chosen. This accounts for possible errors that have been found to arise if the ions make nearly an exact integer number of full turns.

9. The reduced cyclotron frequency F_+ is measured using equation 2.19, using the phase

difference measured here, and number of full turns "n_+" calculated based on the MM8 value calculated from the calibration file. The value of F_+ is calculated again using $n_+ \pm 2$, and the value of n_+ which yields a final result closest to the MM8 guess is chosen. This accounts for possible errors that have been found to arise if the ions make nearly an exact integer number of full turns. As discussed in Section 2.6.2, it is important that an appropriate value of t_{acc+} is chosen based on how well the reduced cyclotron frequency measured, such that a difference of one full turn is extraordinarily unlikely ($> 5\sigma$) to yield the true value of F_+.

10. For each measurement of F_+, a cyclotron frequency is calculated by summing F_+, and a linearly interpolated value of F_- (again, assuming at least who measurements of F_- were made). The uncertainty in F_c is calculated using the deviation in phase of the clustered beam spot with no phase accumulation, F_- phase accumulation, and F_+ phase accumulation.

11. The results are packaged and saved in a ".ft2" file, using the same format as TOF-ICR results, allowing them to be analysed and plotting using the same SOMA (Simple Online Mass Analysis) software LEBIT has used for over a decade.

C.4 AnalysisGUI.py

When an online experiment is being run, there are constantly people around to monitor it, as every moment is valuable. As such, it is unwise to use the AutoRunPIICR.py script, where the data cannot be monitored in real time. For this purpose, AnalysisGUI.py was developed. When run, the program generates the GUI displayed in Figure C.2

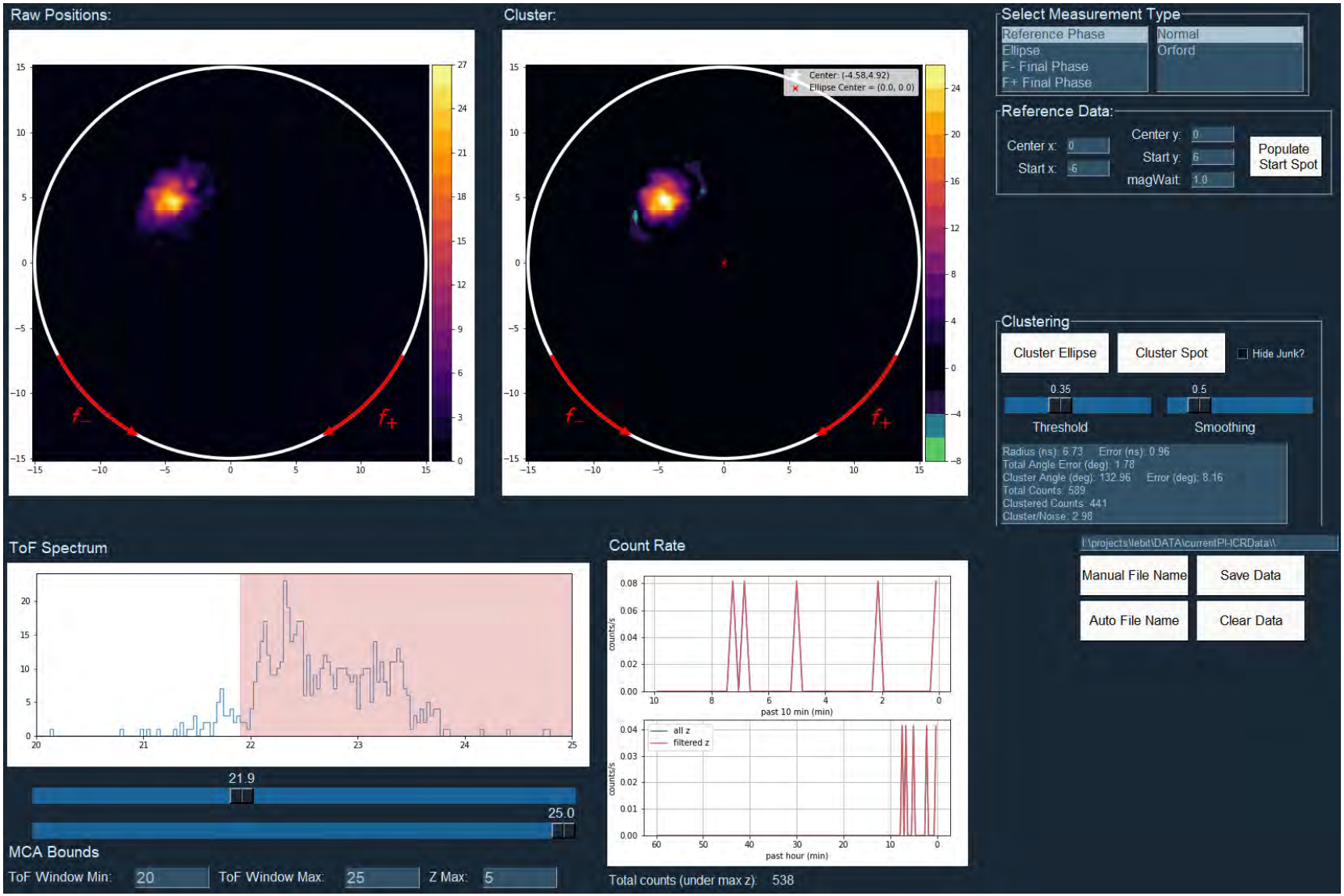

Figure C.2: The PI-ICR real time analysis GUI, AnalysisGUI.py

The “Raw Positions” panel on the top left shows a real-time heatmap of detected ion positions. These positions are filtered by the time of flight selected by the “MCA Bounds” slider, and the counts/shot maximum, “Z Max”, both bottom left. The ToF spectrum shows a histogram of number of ions recoreded over a given time of flight. The red highlighting over it is the MCA-range, data outside of this range will be excluded from from plotting and saved data. For PI-ICR it’s often good to cut out the fastest ions, as is the case in Figure C.2. The “Count Rate” plot shows the count rate before and after filtering plotted over the last ten minutes, and the last hour to watch for short and long term changes in the ion count rate. The “Cluster” plot shows data as positive and noise as negative on another heatmap. Clustering only occurs when “Cluster Ellipse” or “Cluster Spot” are pressed in the “Clustering” panel on the right. Optionally, the noise can be excluded from the plot by checking the “Hide Junk?” box. The “Clustering” panel also has sliders to adjust the clustering parameters, and displays several parameters such as the beam spot size/ellipse dimensions, the signal to noise ratio, and the number of ions contained in the cluster. Beneath this, the data can be saved or cleared; f the appropriate measurement type from the “Measurement Type” box is selected, “Auto File Name” can be pressed in order to set the file name using the same convention as is used in AutoRunPIICR.py. The GUI generates and saves the data with the same header as the AutoRunPIICR.py script.